Eindhoven University of Technology

MASTER

Acoustically enhanced heat transfer in pool boiling measurements

van de Sande, Bram

Award date:
2012

Acoustically enhanced heat transfer in pool boiling measurements

B. van de Sande

WPT 2012.04

Supervisors
dr. C.W.M. van der Geld (TU/e)
dr. ir. P.L.M.J. van Neer (TNO Delft)
dr. ir. A.S. Lexmond (TNO Delft)

TNO Delft
Process and Instrumentation Development

Eindhoven University of Technology
Department of Mechanical Engineering
Thermo Fluids Engineering
Section Process Technology

Eindhoven, June, 2012

Table of Contents

Summary

The heat transfer rates in pool boiling are among one of the highest in nature. Boiling is therefore widely used for cooling and its application can be found in a lot of different engineering fields. A drawback of boiling is the maximum in the heat transfer rate. It is investigated if we can enhance the heat transfer in pool boiling by acoustic excitation. It is assumed that excitation in the resonance mode of growing vapor bubbles promotes detachment of the bubbles from the heater surface, thereby increasing the micro-convection. A variety of experiments are performed, where the frequency dependence of the waves is investigated. Bubbles are excited in their volumetric resonance mode as well as in their first order anisotropic mode.

During acoustic excitation in the volumetric resonance mode of the bubble, volume decrease was observed. Moreover, the bubble growth times decreased and the detachment of the boiling bubbles was promoted. The effect of temperature on the volume decrease is excluded. The largest decrease in bubble volume was observed for applied frequencies close to the theoretical predicted resonance frequencies.

Volume decrease in the first order anisotropic mode was observed as well, however due to limitations in the experimental setup we were not able to measure a resonance response. The observed decrease in volume and growth time is of interest for future research.

The effect of volume decrease on heat transfer is investigated. A decrease of approximately 14 % in the heat transferred by the bubbles to the liquid is obtained, which should result in a higher convective heat transfer. Since the order of heat transported by vapor bubbles is a factor ten smaller than the convective heat transfer, the enhancement is in the order of 1 %.

Nomenclature

Latin

a	Radius of ellipsoid	m
A	Amplitude (chapter 2)	m
A	Surface	m^2
b	Height of ellipsoid	m
b	Constant for bubble growing at wall	
c	Speed of sound	m/s
C	Conversion factor	m/px
c_D	Drag force coefficient	-
c_p	Specific heat at constant pressure	J/(kg K)
C_s	Shape factor	
D	Diameter	m
D_c	Diameter of contact surface	m
f	Departure frequency	1/s
F	Force	N
g	Gravity acceleration	m/s^2
h	Height of bubble center	m
h_{ev}	Latent heat of evaporation	J/kg
I	Intensity	W/m^2
k	Stiffness	N/m
k	Wavenumber	
m	Mass	kg
m	integer	
n	integer	
N_a	Number of active nucleation sites	#
p	pressure	N/m^2
P_0	Static pressure	N/m^2
P_n^m	Legendre polynomial	
q"	Heat flux	W/m^2
r	Radius	m
R	Radius	m
t	Time	s
T	Temperature	K
u	Velocity	m/s

V	Volume	m^3
x	Distance	m
Y	Spherical harmonic	
z	Two times height of bubble center	m
Z_a	Impedance	Ω

Greek symbols

α	Thermal diffusivity	m^2/s
α	Added mass coefficient	-
β	Amplitude	m
γ	Polytropic constant	C_p/C_v
δ	Damping constant	
Δ	Difference	
ϵ	Displacement	m
θ	Contact angle	$^\circ$
θ_{st}	Static contact angle	$^\circ$
λ	Thermal conductivity	W/m K
λ	Wavelength	m
μ	Dynamic viscosity	kg/(s m)
ν	frequency	1/s
xi	Displacement	m
Π	Power	W
ρ	Mass density	kg/m^3
σ	Surface tension coefficient	N/m
ϕ	Phase angle	$^\circ$
Φ	Velocity potential	
Ψ	Complex amplitudes	m
ω	Natural radian frequency	radians/s

Superscripts

$''$	Value per unit area	$1/m^2$

Subscripts

∞	Infinity
bubble	Bubble
bulk	Bulk
c	Critical
cav	Cavity
CHF	Critical Heat Flux
F	Forcing
l	Liquid
L	Lamb
max	Maximum
M	Minnaert

ONB	Onset of Nucleate Boiling
PT-100	PT-100 sensor
ref	Reference
RP	Rayleigh-Plesset
sat	Saturation
v	Vapor
wall	Wall

Coordinates

(x,y,z)	Carthesian
(r, θ, ϕ)	Spherical

Dimensionless numbers

g_0	Constant to account for the wall	$g_0 = \frac{R}{z}$
Ja	Jacob number	$\mathrm{Ja} = \frac{\rho_l c_{p_l}(T_{\mathrm{wall}} - T_{\mathrm{sat}})}{h_{ev}\rho_v}$

Abbreviations

SSBG	Stainless Steel Bubble Generator

Chapter 1

Introduction

In recent years there has been an increasing demand for smaller and faster electronic devices such as portable computers, cameras and mobile phones. The sizes of the micro-electronic parts, *i.e.* think of chips or processors, are nowadays reduced to the order of several millimeters, whereas the heat generation of these parts has not diminished that significant. As a consequence, the generated heat per unit surface is increasing and heat fluxes of 1 $\mathrm{kW/cm^2}$ can be expected in the next few years [16]. Advanced cooling techniques realizing higher heat transfer rates will therefore become even more important. One of such techniques is studied in this report and utilized boiling.

1.1 Boiling

The phase change of a liquid into a vapor during boiling results in one of the highest heat transfer rates in nature. Especially the heat transfer during so-called *nucleate pool boiling* is large. Boiling processes are nowadays widely used for cooling and application can be found in a variety of engineering and industrial applications (see figure 1.1). Heat transfer in nucleate pool boiling is subject of the present study and we start to elucidate the characteristics in the following subsections.

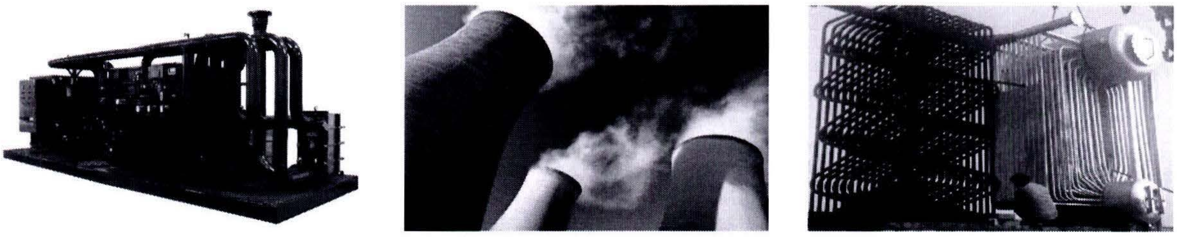
(a) Heat exchanger (b) Cooling tower (c) Water-tube steam boiler

Figure 1.1: Boiling processes used for cooling in a variety of industrial applications

1.1.1 Pool boiling

Boiling can be classified into different categories. The process in which a heating surface is submerged in a large volume of stagnant fluid is called pool boiling. During pool boiling, the generated vapor bubbles and the surrounding fluid near the heating surface have a relative motion, primarily induced by the buoyancy forces acting on the bubbles. The bulk however is at rest and heat transfer takes place by natural convection and by liquid refreshment induced by bubble motion. On the other hand, forced convection occurs when a flow is forced over the heating surface, thereby influencing the bubble dynamics in nucleate boiling [80]. In the remaining of this study we focus on pool boiling.

1.1.2 Pool boiling curve

The pool boiling process consists of different boiling modes. Each mode has its own characterizing behavior and corresponding heat transfer rates. The modes can be identified using a pool boiling curve, where the heat transfer rate is given as a function of superheated temperature. The superheat of temperature, ΔT, is in general defined as:

$$\Delta T = T_{\text{wall}} - T_{\text{sat}} \tag{1.1}$$

Note that since the saturation temperature of the fluid T_{sat} depends on pressure, the boiling process is determined by the wall superheat and not solely by the temperature of the wall T_{wall} [62].

Nukiyama (1966) [53] was one of the first who presented the boiling curve for pool boiling and was followed by among others Rohsenow (1971) [62] and later Dhir (1998) [26]. Figure 1.2 shows a typical pool boiling curve indicating the different boiling modes. For low superheated wall temperatures natural convection is the only mode of heat transfer and almost no vapor bubbles are present in the fluid. By increasing ΔT, vapor bubbles start to grow and rise from the heating surface. This specific wall superheat is referred to as the onset of nucleate boiling (ONB) and is denoted in figure 1.2 by point A. The value of the minimum needed heat flux for the onset of boiling bubbles q''_{ONB} is derived in section 2.1.1.

Beyond the ONB the slope of the boiling curve increases and vapor bubbles are generated at random active nucleation sites. For higher superheated temperatures, more nucleation sites become active and the frequency of bubble departure is increased. In this mode the bubbles form columns and slugs to the free surface and the associated fluid entrainment normal to the heated surface results in higher heat transfer from wall to liquid [12]. The mode is referred to as the nucleate boiling mode, where the highest heat transfer rates are obtained.

1.1.3 Critical heat flux

The nucleate boiling mode is limited by a maximum in the heat flux q''_{CHF} at a certain critical superheated wall temperature ΔT_c. This critical heat flux (CHF) corresponds to point B in figure 1.2. For non-subcooled water at atmospheric pressure, the critical heat flux can be as high as 10^6 W/m^2 with 20 Kelvin temperature difference and almost no flow [63].

Near the critical superheated wall temperature ΔT_c, a large number of vapor bubbles is present in the flow. At this point the bubbles coalesce and it is extremely difficult for the fluid to reach the heater surface. For superheated temperatures exceeding ΔT_c, the fluid is not able to reach the heater surface anymore and the vapor starts to form an insulated film, reducing the heat transfer. In this region (between B - C in figure 1.2) the slope of the boiling curve is negative and a transition mode will lead to the film boiling mode. The transition mode is highly unstable since a small increase in ΔT leads to a lower heat transfer from heater wall to fluid, which increases ΔT even more. The characterizing insulating vapor film can lead to destructive failure of the device! The device should therefore always be operated at temperatures below ΔT_c.

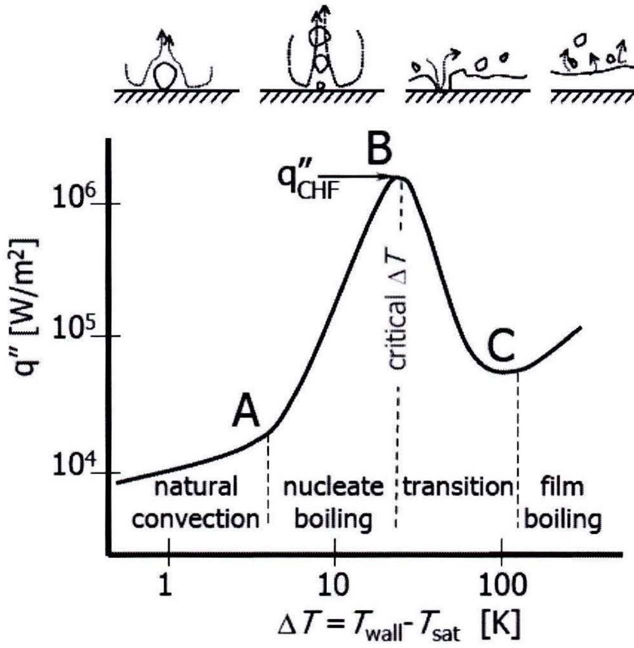

Figure 1.2: Typical pool boiling curve characterizing the different boiling modes as function of wall superheat $\Delta T = T_{\text{wall}} - T_{\text{sat}}$ based on Nukiyama's [53] boiling curve. The vertical axis shows the heat flux q'' from heater wall to fluid [W/m^2]. Values are indicative for water. (*From "Two phase flow and phase change heat transfer in small structures"*, 2009. C. M. Rops, p. 45 [12])

Point C in figure 1.2 is commonly referred to as the 'Leidenfrost point' [5], which signifies the onset of stable film boiling. It represents the point on the boiling curve where the heat flux is at the minimum and the surface is completely covered by a vapor film. Above this value, radiation is the main heat transfer mechanism.

1.2 Heat transfer enhancement

The increasing heat flux problem as was sketched in the beginning of this introduction, requires a higher heat transfer rate than the typical q''_{CHF} in pool boiling (see figure 1.2). Conventional pool boiling as cooling can therefore lead to destructive failure of future devices. Since failure needs to be prevented at all time, it is very desirable to enhance the boiling heat transfer rate and the maximum of the critical heat flux. The enhancement of heat transfer, using different techniques, has been investigated in the last decades by several researchers.

The different enhancement techniques can be classified into passive -and active techniques as was done by Bergles and Webb (1983) [69]. The passive techniques do not require the application of external power and one can think of differently treated surfaces, displaced enhancement devices, swirl flow devices or additives for fluids [19]. More recent, Rops *et.al.* (2009) [63] obtained a significant heat transfer enhancement by confining the geometries of the boiling pool and the heater surface. However, the active techniques for heat transfer enhancement are of more interest and experiments with mechanical aids, surface vibration, ultrasonic fluid excitation or jet impingement are among the present studies on heat transfer enhancement.

1.3 Present work

From the active enhancing techniques, ultrasonic fluid excitation seems to be the most applicable technique. Ultrasound is expected to be able to increase the critical heat flux as it is known to cause micro-mixing, initiate bubble formation and transport micro-bubbles. The three different effects are depicted in figure 1.3. It is therefore that the present study focuses on heat transfer enhancement in pool boiling using ultrasonic fluid excitation.

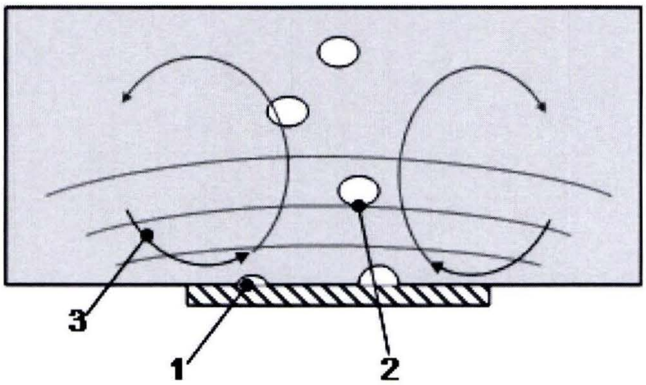

Figure 1.3: Possible effects of ultrasonic excitation: 1) the initiation of bubble formation, 2) transport of the micro-bubbles from the heater surface and 3) the increase in micro-mixing in the fluid.

To support our hypothesis we found several publications on the topic of heat transfer enhancement using ultrasound. The first studies were carried out by among others Fand (1965) [29], Li and Parker (1967) [43] and Wong and Chon (1969) [71] who reported a noticeable augmentation in the natural convection -and film boiling regime. They all concluded that the main mechanisms leading to heat transfer enhancement in natural convection and in subcooled boiling are acoustic streaming and cavitation. Jeong and Kwon (2006) [39] found an increase in the critical heat flux by suppressing the generation of large vapor bubbles.

More recent Douglas *et.al.* (2007) [27] investigated the boiling heat transfer of a single vapor bubble in the vicinity of a rigid-heated wall. It was found that ultrasound can lead to unstable waves on the interface of the bubble with the heater, which are violent enough to detach the bubble from its surface. By influencing the detachment of bubbles, Douglas *et.al.* succeeded to increase the critical heat flux.

An overview of the complete literature study is given in appendix A where the concepts of acoustic streaming and cavitation are discussed.

1.3.1 Goal

In the present work we try to enhance the heat transfer in pool boiling by ultrasonic fluid excitation. Our main focus lies on the promotion of the detachment of boiling bubbles from the heater surface, thereby increasing the bubble departure frequency and the bubble induced micro-convection near the heater surface.

1.3.2 Outline

It is assumed that the detachment of the boiling bubbles from the heater surface can be influenced by sonic fluid excitation with frequencies equal to the resonance frequencies of the boiling bubbles, where the attached vapor bubble starts to resonate and the detachment of the bubble is promoted. If successful, it is desired to know how much additional heat transfer can be enforced using ultrasonic waves. Heat transfer enhancement through ultrasonic excitation is expected to outweigh the additional heat generation of the transducer, but this need to be verified.

1.3.3 Approach

The present work combines two different fields of study into one: the boiling process and corresponding boiling bubble dynamics play of course a very important role, but on the other hand sound excitation and propagation needs to be well understood to do useful experiments and draw the right conclusions. The basics of both mechanisms are treated in the next two chapters, starting with theory of boiling bubbles. For the experiments we used a specially designed and manufactured single bubble generator, which is able to generate boiling bubbles of constant volume and constant growth times departing from an artificial cavity. The effect of sonic excitation on the growing boiling bubble is investigated with use of a high speed camera and a simple swimming pool loudspeaker. A more extensive description of the experimental setup and an error analysis can be found in chapter 4. The obtained results of the experiments done are presented in chapter 5 and will be extensively analyzed in chapter 6. The report ends with the most important conclusions and recommendations for future work.

Chapter 2

Bubble theory

The present study focusses on the effects of acoustic excitation on bubble detachment. By promoting the detachment of boiling bubbles from the heater surface we try to increase the heat transfer rate. For a thorough comprehension of the problem, it is important to gain insight in the dynamics of single vapor bubbles. Especially shape -and volumetric oscillations have major influences on bubble dynamics. We start with the theoretical background of boiling and treat the onset and growth of vapor bubbles. Subsequently, the resonance modes of a freely oscillating bubble are discussed and correlations to correct for the proximity of the heater wall are presented.

2.1 Boiling bubble

One of the main characteristics of a (nucleate) boiling process is the presence of a vapor phase throughout a complete liquid phase. The vapor phase consists in general of boiling bubbles, which originate from irregularities and cavities on the heated surface. At these nucleation sites vapor is trapped in and bubble nuclei are formed [12]. The onset of bubbles from the heated surface starts when sufficient heat flux is applied.

2.1.1 Onset of nucleate boiling

Hsu (1962) [35] was the first researcher who presented criteria for bubble incipience. The pressure inside an initial vapor bubble p_v is typically higher than the pressure of the surrounding liquid p_l. This capillary pressure difference Δp across the liquid - vapor bubble interface can sustain due to the presence of the surface tension σ of the fluid. The capillary pressure difference in thermo-dynamic equilibrium is described by the Young-Laplace relation [35]:

$$\Delta p = p_v - p_l = \frac{2\sigma}{R} \tag{2.1}$$

The corresponding saturation temperature inside the vapor bubble can be estimated by combining the Young-Laplace equation 2.1 with the Clausius-Clapeyron equation and is approximately given by Basu [18]:

$$T_v = T_{\text{sat}} + \frac{2\sigma T_{\text{sat}}}{R\rho_v h_{ev}} \tag{2.2}$$

with T_{sat} the saturation temperature of the bulk, σ the surface tension of the liquid, R the bubble radius, ρ_v the density of the vapor and h_{ev} the latent heat of evaporation. Hsu [35] postulated that the liquid temperature surrounding the bubble should at least be equal to the saturation temperature inside the bubble. This condition supports evaporation at the bubble interface and allows the bubble to grow.

A linear relation can be used to describe the temperature distribution in the thermal boundary layer, which is the thin layer of liquid between the bulk and the heater surface where the temperature changes from that of the wall to that of the free bulk. If we assume that the initial bubble size is in the same order of magnitude as the cavity it originates from - which is typically smaller than the thickness of the thermal boundary layer - the linear temperature drop in the thermal boundary layer is expressed as [12]:

$$T(y) = T_{\text{wall}} - \frac{q'' y}{\lambda_l} \tag{2.3}$$

where y is the normal position with respect to the heater wall and λ_l is the thermal conductivity of the liquid.

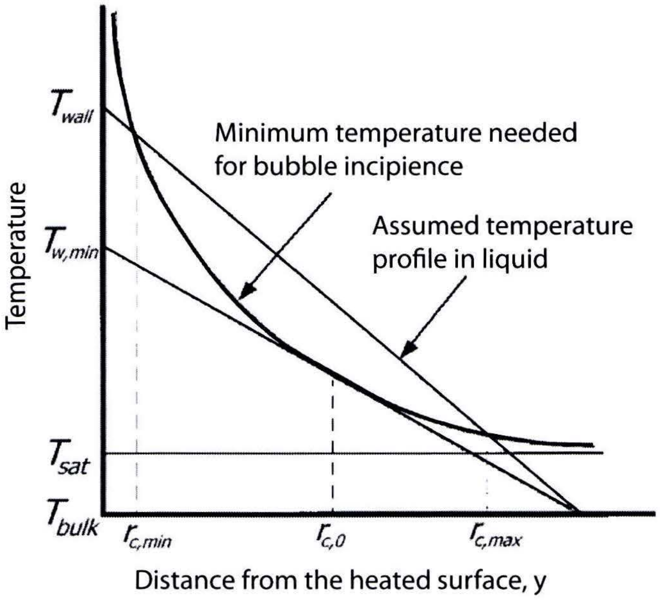

Figure 2.1: Criteria needed for the onset of boiling bubbles. $r_{c,min}$ is the minimum allowed cavity radius for nucleation, $r_{c,max}$ is the maximum allowed cavity radius for nucleation and $r_{c,0}$ corresponds to the cavity size allowing nucleation at the minimum wall temperature. Drawing is based on the work of Hsu [35]. (*From "Two phase flow and phase change heat transfer in small structures"*, 2009. C. M. Rops, p. 38 [12])

The minimum needed wall heat flux for the onset of vapor bubbles can be derived from the equations 2.2 and 2.3 and the corresponding figure 2.1. Sato and Matsumara [64] were the first who derived an analytical expression for this minimum needed heat flux as function of the wall superheat ΔT. Davis and Anderson [24] extended the expression with the contact angle as additional variable and the resulting analytical expression for the minimum needed wall heat flux for the onset of boiling bubbles is given by:

$$q''_{ONB} = \frac{\lambda_l h_{ev} \rho_v (\Delta T)^2}{8\sigma T_{\text{sat}}(1 + \cos\theta)} \tag{2.4}$$

2.1.2 Inertia controlled bubble growth

If the minimum needed heat flux for the onset of boiling bubbles q''_{ONB} is applied to the heater, the vapor trapped inside the cavities starts to grow. There are two main constraints to the rate of growth: the inertia of the surrounding liquid has to be pushed away by the vapor and heat has to diffuse from the surrounding liquid to the bubble interface to cause evaporation.

Inertia-controlled growth occurs in the early stages of the growth, particularly at low pressures when only a small amount of heat is needed to create a large volume of vapor [84]. The growth in this initial stage, when the bubble is infinitesimally small, is driven by the excess pressure equal to $2\sigma/R$ (equation 2.1), induced by the surface tension across the liquid-vapor interface.

The equation describing bubble growth solely controlled by inertial forces can be derived from the continuity equation as was done in the work of Mikic *et.al.* [46]. They arrive at the Rayleigh equation, where $b = 2/3$ for bubble growth in an infinite mass of liquid and $b = \pi/7$ for a spherical growing bubble attached to the wall [46]:

$$\boxed{R = At \qquad \text{with} \qquad A = \Big(b\frac{h_{ev}\rho_v \Delta T}{\rho_l T_{\text{sat}}}\Big)^{\frac{1}{2}}} \tag{2.5}$$

2.1.3 Heat diffusion controlled bubble growth

The mechanism that drives the growth of an initial vapor bubble in time is vaporization. The process is maintained by the energy transfer from the superheated liquid to the interface of the bubble. It is shown by among others Plesset and Zwick (1952) [58] that the evaporation flux - due to heat diffusion at the bubble interface - is dominating during the bubble growth [12]. Liquid properties like the surface tension coefficient σ, ratio of specific heats γ and dynamic viscosity μ, which are parameters characterizing the resonance frequencies of a bubble, are much less important in bubble growth.

The growth of a vapor bubble in time can be analyzed by the one-dimensional transient heat conduction problem of Zuber (1961) [74]. To do so, we need to assume a constant saturation temperature at the bubble interface and a uniformly superheated fluid. The energy balance of a growing bubble is given as:

$$h_{ev}\rho_v \frac{dR}{dt} = \lambda_l \frac{T_{\text{wall}} - T_{\text{sat}}}{\sqrt{\pi \alpha t}} \tag{2.6}$$

with h_{ev} the latent heat of evaporation, ρ_v the density of the vapor, R bubble radius, T_{wall} temperature of the heater wall, T_{sat} the saturation temperature, λ_l the thermal conductivity, $\alpha = \lambda_l/(\rho_l c_{p_l})$ the thermal diffusivity and t the growth time in seconds.

In the heat conduction problem of Zuber, the surface tension, fluid inertia, moving bubble boundary and sphericity of the bubbles are neglected. To account for the sphericity, a so-called constant shape factor C_s needs to be introduced. Different values for the shape factor can be found in literature, where the most have a value in the order of one. Zuber (1961) proposed a factor of $C_s = \pi/2$, whereas Plesset and Zwick (1954) [59] suggest a shape factor of $C_s = \sqrt{3}$.

The equation describing the bubble radius as function of time during the diffusion-controlled growth, can be obtained by integration of equation 2.6 and introduction of the shape factor:

$$\boxed{R = \frac{2}{\pi} \cdot C_s \cdot \mathrm{Ja}\sqrt{\pi \alpha t} \qquad \text{with} \qquad \mathrm{Ja} = \frac{\rho_l c_{p_l}(T_{\text{wall}} - T_{\text{sat}})}{h_{ev}\rho_v}} \tag{2.7}$$

Ja is the dimensionless Jacob number, which is a measure of the ratio of sensible heat to latent heat absorbed during the phase change. In the remaining of this chapter we take for the constant shape factor C_s the value as proposed by Plesset and Zwick: $C_s = \sqrt{3}$. However in chapter 5 we try to find the shape correction factor C_s corresponding to the bubbles of the present work.

2.1.4 Forces acting on growing bubbles

To be able to determine the bubble radius at detachment, we take a look at the forces acting on the bubble during its growth.

The bubble experiences forces which attach the bubble to the wall, *i.e.* the surface tension force and drag force related to bubble growth. On the other hand, detaching forces are working on the bubble in the direction away from the wall, *i.e.* the buoyancy force and the contact pressure force. Inertia forces are neglected. To account for the inertia forces, we introduce an added mass coefficient in section 2.4.1.

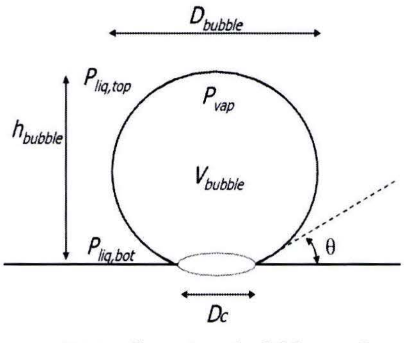

Figure 2.2: Growing bubble on heater surface *From "Two phase flow and phase change heat transfer in small structures"*, 2009. C. M. Rops, p. 40 [12])

The different forces acting on the growing bubble are presented in equation 2.8 and 2.9. The derivations are not treated here and for a thorough analysis of the different forces acting on the bubble, the reader is referred to Chen [22], Helden *et.al.* [34] and Van der Geld [30].

The attaching forces on the bubble are given by:

$$\begin{aligned} F_{\text{attach}} &= F_{\text{surf.tension}} + F_{\text{drag}} \\ &= \pi D_c \sigma \sin\theta + c_D \rho_l \frac{\pi}{4} D_{\text{bubble}}^2 \frac{(\frac{dh}{dt})^2}{2} \end{aligned} \tag{2.8}$$

Whereas the detaching forces are given by:

$$\begin{aligned} F_{\text{detach}} &= F_{\text{buoyancy}} + F_{\text{contact.press}} \\ &= (\rho_l - \rho_v) g V_{\text{bubble}} + \sigma\left(\frac{1}{R_1} + \frac{1}{R_2}\right)\frac{\pi D_c^2}{4} \end{aligned} \tag{2.9}$$

In general, the only force which is important enough to counteract the detachment forces is the surface tension force. The drag force only plays a role for high bubble growth rates. Bubble inertia force due to the acceleration of the bubble center of mass can be neglected in most cases [22].

At all times prior to bubble detachment, Newton's second law is satisfied ($F_{\text{detach}} = F_{\text{attach}}$). The force balance does not offer a criterion for bubble detachment, since detachment occurs only at one specific instant of time [77]. To determine the size and corresponding resonance frequency of the bubble at detachment, we need another (geometrical) criterion.

2.1.5 Bubble at detachment

The specific shape and size of a boiling bubble that grows from the heater surface is affected by a lot of factors, that a general description is very complex. The different factors are for example gravity, surface tension, contact angle between heater and bubble boundary, geometry of the heater surface, thermal properties or inertia and viscosity of both phases. It was proved by Chesters [23] that under certain conditions the size and shape at detachment are governed by the the first four factors mentioned above. Chesters investigated the case of a slow, isothermal growing vapor bubble on a sharp-edged orifice.

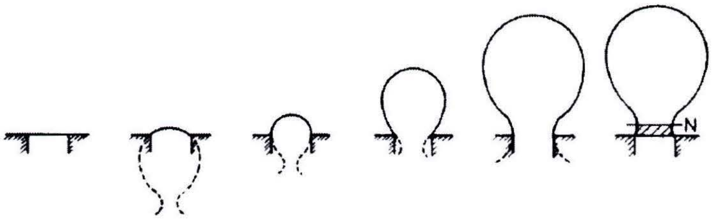

(a) Mode A bubble growth

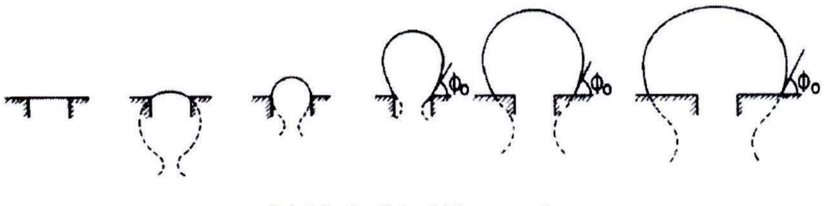

(b) Mode B bubble growth

Figure 2.3: Modes of bubble growth from artificial cavity (*From "Modes of bubble growth in the slow-formation regime of nucleate pool boiling"*, 1978. Chesters, A.K. [23])

There are two types of growth modes which are indicated in figure 2.3. In mode A the bubble boundary is equal to the cavity edge, whereas in mode B the bubble grows beyond the edge. It depends on the contact angle (material properties of liquid and heater) which growth mode occurs. During the experiments of Chesters [23] the growth mode B did not occur. It was concluded that this is attributed to the slowness with which a contact angle attains its equilibrium value. From previous measurements it is known that our generated bubbles will be of growth mode A as well.

Estimation of bubble radius at detachment

In mode A the scale of the profile (*i.e.* the value of R) reaches a maximum when the plane of attachment is equal to the plane cutting the profile in the neck region, where the point N corresponds to the neck point ($\theta = 90°$ see figure 2.4).

If the plane of attachment grows beyond the neck region, the volume enclosed by the profile above N is diminished. Unless this diminution is compensated by an increase in the volume of the shaded zone of figure 2.3(a), the maximum bubble volume has been reached and the bubble detaches [23]. The maximum bubble volume, enclosed by the bubble boundary and the horizontal plane through the neck region, can be calculated using equation 14 in Chesters [23]:

$$V = \frac{4}{3}\pi R^3(1+\beta) \tag{2.10}$$

where β is a dimensionless parameter defined as:

$$\beta = \frac{\rho g R^2}{\sigma} \tag{2.11}$$

The horizontal distance of the neck point N from the vertical axis of symmetry, x_N, can now be calculated as:

$$x_N = \frac{r_{cav}}{R} = \frac{2\beta}{3} \tag{2.12}$$

with r_{cav} the radius of the artificial cavity. Introduction of equation 2.11 into equation 2.12 results in the approximation of the maximum bubble radius at detachment:

$$\boxed{R^3_{\max} = \frac{3r_{cav}\sigma}{2\rho g}} \tag{2.13}$$

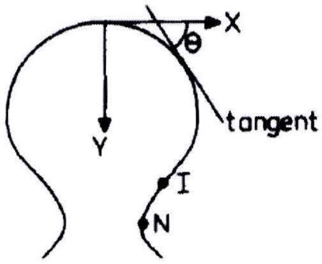

Figure 2.4: Coordinate system used by Chesters [23]

The order of the resonance frequency of a vapor bubble at detachment is predicted in section 2.5 based on the approximation of $R_{\max}$. In the chapter results it will be investigated if this approximation corresponds to our experiments.

2.2 Resonance response of free bubble

Consider a free bubble in an unbounded incompressible liquid in absence of a wall. To investigate how the bubble reacts on a forced sound wave, we take a look at the dynamical behavior of a forced (weakly damped) oscillator and use it to characterize the resonance response of a free bubble.

2.2.1 The forced free bubble

The small amplitude pulsation of a free vapor bubble in an unbounded liquid acts analogue to an unforced linear oscillator in terms of a bob on a spring. Theory of a forced linear oscillator can be used to describe the response of a forced free bubble in an unbounded liquid. The same analogy holds: the displacement of the bob corresponds to the oscillating motion of the bubble boundary, whereas the spring constant k acts as the restoring force (pressure changes in the vapor compressed or rarefied within the bubble) [8]. The driving force is the acoustic pressure wave, which acts on the bubble.

2.2.2 Undamped unforced harmonic oscillator

The equation of motion of an undamped simple harmonic oscillator is given by

$$\ddot{\epsilon} + \frac{k}{m}\epsilon = 0 \tag{2.14}$$

where ϵ is the displacement, k the stiffness and m the mass of the oscillator. From basic dynamics it follows for the natural frequency ω_0 of the oscillator:

$$\omega_0^2 = \frac{k}{m} \tag{2.15}$$

Mathematically there are two possible solutions: one oscillating as $\mathrm{e}^{\mathrm{i}\omega_0 t}$, the other as $\mathrm{e}^{-\mathrm{i}\omega_0 t}$ respectively. A general solution to equation 2.14 is therefore given by:

$$\epsilon = \Psi_1 \mathrm{e}^{\mathrm{i}\omega_0 t} + \Psi_2 \mathrm{e}^{-\mathrm{i}\omega_0 t} \tag{2.16}$$

where Ψ_1 and Ψ_2 are the complex conjugates $\Psi_2 = \Psi_1^*$.

2.2.3 Undamped forced harmonic oscillator

The equation of motion of a forced undamped harmonic oscillator can be written as:

$$\ddot{\epsilon} + \frac{k}{m}\epsilon = \frac{F_0}{m}\mathrm{e}^{\mathrm{i}\omega_F t} \tag{2.17}$$

where F_0 is the amplitude of the applied force and ω_F the frequency of the force. A general solution to equation 2.17 is given by

$$\epsilon = \Psi_1 \mathrm{e}^{\mathrm{i}\omega_0 t} + \Psi_2 \mathrm{e}^{-\mathrm{i}\omega_0 t} + A\mathrm{e}^{\mathrm{i}\omega_F t} \tag{2.18}$$

For zero damping, the constant A is real. The former part of the solution contains the frequency information at ω_0 in the transient response, the latter part describes the steady-state response at ω_0 [8].

In steady state, $t \to \infty$, the response of the oscillator is given by $\epsilon = A\mathrm{e}^{\mathrm{i}\omega_F t}$. Introduction of this expression into the equation of motion 2.17 results in the amplitude of oscillation:

$$\boxed{A = \frac{F_0}{m(\omega_0^2 - \omega_F^2)}} \tag{2.19}$$

2.2.4 Damped forced harmonic oscillator

The equation of motion of a damped forced oscillator is given by:

$$\ddot{\epsilon} + \delta\dot{\epsilon} + \omega_0^2\epsilon = \frac{F_0}{m}e^{i\omega_F t} \tag{2.20}$$

Substitution of $\epsilon = Ae^{i\omega_F t}$ for steady state results in:

$$((\omega_0^2 - \omega_F^2) + i\frac{\delta}{m}\omega_F)A = \frac{F_0}{m} \tag{2.21}$$

If the complex amplitude A is explicitly written as $A = |A|e^{-i\vartheta} = |A|\cos(\vartheta) - i|A|\sin(\vartheta)$ and the real -and imaginary parts of equation 2.21 are squared and added, we arrive at the expression for the amplitude of oscillation [8]:

$$\boxed{|A| = \frac{F_0/m}{\sqrt{(\omega_0^2 - \omega_F^2)^2 + (\frac{\delta\omega}{m})^2}}} \tag{2.22}$$

To obtain oscillatory solutions the damping δ must be light. Figure 2.5 shows the normalized displaced amplitude as function of ω_F/ω_0.

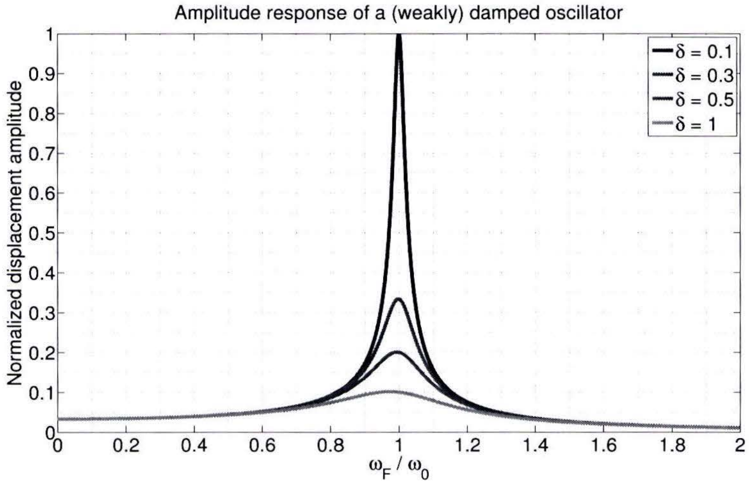

Figure 2.5: Amplitude response of a weakly damped forced harmonic oscillator. For decreasing damping constants δ the resonance peak sharpens and the amplitude at resonance increases.

The figure shows that for decreasing damping constants δ the resonance peak sharpens and the amplitude at resonance increases. If the frequency of the forced excitation ω_F approaches the resonance frequency of the weakly damped oscillator ω_0 - in our case the vapor bubble - the amplitude of the resonant oscillations becomes enormous [8].

2.3 Freely oscillating bubble

To be able to promote the bubble detachment by acoustic excitation in the bubble resonance frequencies, it is of importance to gain more insight in the bubble dynamics. The dynamical behavior of a bubble is characterized by spherical (isotropic) volume oscillations and much more complicated non-spherical (anisotropic) shape oscillations. Both types of oscillations can be derscribed using a superposition of spherical harmonics as will be shown in this section. We start with the natural volumetric response of the free bubble.

2.3.1 Isotropic volume oscillation

The first bubble dynamic studies concentrated on freely oscillating bubbles as a source of sound in running water, where the time dependent changes in bubble volume were of major interest. In 1933 Minnaert [47] proposed a 'pulsating theory' on this type of spherical volume oscillations. In his theory he considered the water-vapor system as a harmonic oscillator of the spring-bob type: the inertia of the fluid can be associated to the mass of the bob, whereas the (adiabatic) compressibility can be associated to the stiffness of the spring [25].

Let $R(t)$ be the instantaneous radius of an oscillating free bubble and R_0 the radius of the bubble in its equilibrium position:

$$R(t) = R_0 + \xi \tag{2.23}$$

Minnaert calculated the natural radian frequency (with $\omega = 2\pi\nu$) of this oscillating system by equating the (elastic) potential energy to the maximum kinetic energy. The potential energy can be calculated from the amount of work needed to change the radius from R_0 to $R_0+\xi$, whereas the kinetic energy E_k is a function of the velocity of the expanding free bubble $E_k = f(\dot{\xi})$ [25].

In the analysis of Minnaert, surface tension and viscous attenuation are neglected. Moreover, adiabatic conditions are assumed at the bubble boundary, with $\kappa = \gamma$. The resulting equation is Minnaert's equation describing the eigenfrequency of a free bubble (see [47], [25]):

$$\omega_M = \sqrt{\frac{3\gamma p_\infty}{\rho_l R_{t=0}^2}} \tag{2.24}$$

where $R_{t=0}$ is the initial bubble radius, p_∞ the pressure of the liquid at infinity, $\gamma = C_p/C_v$ the ratio of specific heats and ρ_l is the mass density of the liquid.

Rayleigh-Plesset

A more complex analysis of bubble dynamics, including nonlinearities, started with the work of Rayleigh in 1917 [61]. Rayleigh was the first who solved the problem of a collapsing empty cavity in an unbounded (incompressible) liquid. In 1949 the original equation of Rayleigh was extended by Plesset [56] with surface tension and viscous contributions. The resulting equation leads to the well known Rayleigh-Plesset equation and describes the bubble boundary $R(t)$ as function of time (see Plesset and Prosperetti [57] and Brennen, p. 101 [1]):

$$R\ddot{R} + \frac{3}{2}\dot{R}^2 = \frac{1}{\rho_l}\left\{p_i - p_\infty - \frac{2\sigma}{R} - \frac{4\mu}{R}\dot{R}\right\} \tag{2.25}$$

In this equation ρ_l is the density of the liquid, p_i is the internal pressure at the bubble wall, p_∞ is the pressure at infinity, μ is the dynamic viscosity of the liquid and σ is the surface tension coefficient of the liquid.

The Rayleigh-Plesset equation can be used to calculate the time evolution of the radius of a spherical bubble which is expanding and shrinking in absence of a wall. This isotropic oscillating mode is often referred to as the b_1 mode. For sufficient small changes in radius, the Rayleigh-Plesset equation is linearized with solution [32]:

$$R(t) = R_{t=0}(1 + \beta \sin(\omega_{RP} t)) \tag{2.26}$$

where $R_{t=0}$ is the initial bubble radius and ω_{RP} is the natural volumetric radian frequency corresponding to the isotropic deformation of a bubble. For a freely oscillating vapor bubble this radian frequency is given by (see among others Plesset and Prosperetti [57] and Van der Geld and Kuerten [32]):

$$\boxed{\omega_{RP} = \sqrt{\frac{3\gamma p_\infty}{\rho_l R_{t=0}^2} + \frac{2(3\gamma - 1)\sigma}{\rho_l R_{t=0}^3}}} \tag{2.27}$$

If surface tension effects are neglected (large bubbles), this volumetric radian frequency coincides with the results obtained by Minnaert [47] (equation 2.24).

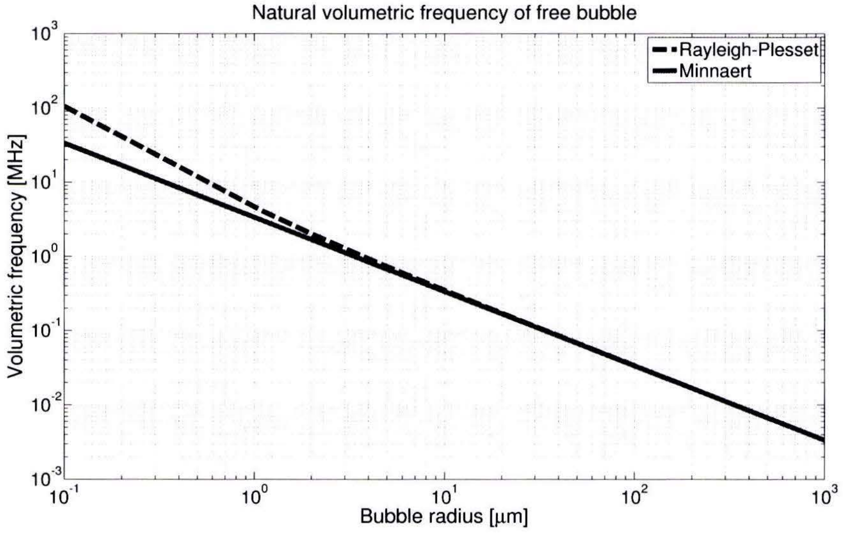

Figure 2.6: Volumetric frequency of a freely oscillating vapor bubble in water as function of bubble radius. Solid line corresponds to the Minnaert equation 2.24: $\nu_M = \frac{\omega_M}{2\pi}$, whereas the dotted line corresponds to the Rayleigh-Plesset equation 2.27: $\nu_{RP} = \frac{\omega_{RP}}{2\pi}$

A simple order analysis of the different terms reveals that the second term on the RHS of equation 2.27 only plays a role for very small bubble radii. To support this conclusion, the frequencies calculated by both the Minnaert equation 2.24 and the Rayleigh-Plesset equation 2.27

are compared in figure 2.6 for the case of a vapor bubble in saturated water. It is shown that the surface tension of a bubble with radius smaller than 5 μm becomes dominant enough to influence the volumetric frequency. For even smaller bubbles the second term on the RHS of equation 2.27 is the prevailing term. A neglect of the surface tension of these micro-bubbles leads to very large errors in the order of several Megahertz.

2.3.2 Non-spherical shape oscillations

Besides the isotropic b_1 resonance mode, higher order oscillation modes occur on the boundary of a disturbed free bubble. These higher order modes are typically non-spherical and can be described using spherical harmonics. The derivations in this subsection are based on the book *The acoustic bubble* by T.G. Leighton [8] and the interested reader is referred to it.

Spherical harmonics

The shape of a bubble oscillating in a higher order mode, can be constructed using a summation of spherical harmonics superimposed on a sphere. The spherical harmonics are a particular group of functions which form a solution to Laplace's equation in a spherical coordinate system. The spherical coordinate system, with coordinates r, θ and ϕ, is related to the Cartesian coordinate system as $x = r\sin\theta\cos\phi$, $y = r\sin\theta\sin\phi$ and $z = r\cos\theta$ (see figure 2.7).

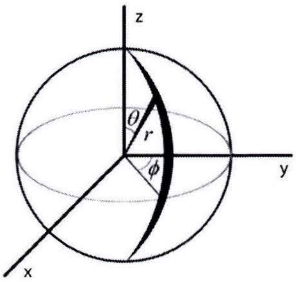

Figure 2.7: The spherical coordinate system with coordinates r, θ, ϕ with respect to the Cartesian coordinates x, y, z.

To derive an equation for the spherical harmonics, we start with introducing the velocity potential Φ (assuming incompressibility and irrotational flow) into the spherical Laplace equation [8]:

$$\nabla^2\Phi = \frac{1}{r^2}\frac{\partial}{\partial r}\left(r^2\frac{\partial\Phi}{\partial r}\right) + \frac{1}{r^2\sin\partial\theta}\frac{\partial}{\partial\theta}\left(\sin\theta\frac{\partial\Phi}{\partial\theta}\right) + \frac{1}{r^2\sin^2\theta}\frac{\partial^2\Phi}{\partial\phi^2} = 0 \tag{2.28}$$

Now consider the function $\Phi(r, \theta, \phi)$ as a solution to equation 2.28. If the three components in r, θ and ϕ of this solution are independent, the potential Φ can be expressed as the product of three independent component functions: $\Phi = \Phi_r\Phi_\theta\Phi_\phi$. Here $\Phi_r = \Phi(r)$, $\Phi_\theta = \Phi(\theta)$ and $\Phi_\phi = \Phi(\phi)$. Substitution of the component functions into equation 2.28 yields the following independent equations (T.G. Leighton, p.105 [8]):

$$\frac{1}{r^2}\frac{\partial}{\partial r}\left(r^2\frac{\partial\Phi_r}{\partial r}\right) - \frac{\mathrm{n}(\mathrm{n}+1)}{r^2}\Phi_r = 0 \tag{2.29a}$$

$$\frac{\partial^2\Phi_\phi}{\partial\phi^2} + \mathrm{m}^2\Phi_\phi = 0 \tag{2.29b}$$

$$\frac{1}{\sin\theta}\frac{\partial}{\partial\theta}\left(\sin\theta\frac{\partial\Phi_\theta}{\partial\theta}\right) + \left(\mathrm{n}(\mathrm{n}+1) - \frac{\mathrm{m}^2}{\sin^2\theta}\right)\Phi_\theta = 0 \tag{2.29c}$$

The solutions to equation 2.29a are of the form r^{n} or $r^{-(\mathrm{n}+1)}$. The solution r^{n} can not be physical, since it implies an increase in radial velocity or intensity for increasing distance from the pulsating bubble. Therefore only solutions of the form $r^{-(\mathrm{n}+1)}$ are relevant.

Equation 2.29b results in solutions of the form $\mathrm{e}^{\mathrm{i}m\phi}$ or $\mathrm{e}^{-\mathrm{i}m\phi}$. The potential Φ_ϕ can thus be obtained for any given angular coordinate ϕ. Moreover, circumventing the z-axis and returning to the same position at the bubble boundary should not change the value of the potential Φ_ϕ. This implies that $\mathrm{e}^{\mathrm{im}\phi} = \mathrm{e}^{\mathrm{im}(\phi+2\pi)} = \mathrm{e}^{\mathrm{im}(\phi+4\pi)}$...etc, which is only valid if m is zero or an integer.

Solutions to equation 2.29c are the so-called Associated Legendre polynomials, $\mathrm{P}_{\mathrm{n}}^{\mathrm{m}}$, where $\mathrm{P}_{\mathrm{n}}^{\mathrm{m}} = \sin^{\mathrm{m}}\theta \mathrm{P}_{\mathrm{n}}$. The value of n must be zero or integer. The first solutions corresponding to the Legendre polynomials P_{n} are given in among others Leighton [8] on page 106 and will not be presented here. If the θ and ϕ dependencies are combined, a function proportional to $\Phi_\theta\Phi_\phi$ is obtained. This function is called the *spherical harmonic*:

$$\mathrm{Y}_{\mathrm{n}}^{\mathrm{m}}(\theta,\phi) = (-1)^{\mathrm{m}}\sqrt{\frac{1}{4\pi}}\sqrt{\frac{(\mathrm{n}-\mathrm{m})!}{(\mathrm{n}+\mathrm{m})!}}\sqrt{2\mathrm{n}+1}\mathrm{P}_{\mathrm{n}}^{\mathrm{m}}(\cos\theta)\mathrm{e}^{\mathrm{im}\phi} \tag{2.30}$$

Zonal harmonics

In the remaining of this report we will only consider axisymmetric shape oscillations, *i.e.* the z-axis is the axis of symmetry. In that case, the spherical harmonics are independent of the angle ϕ (see figure 2.7) and the integer $\mathrm{m} = 0$. If, for example, the value of the spherical harmonic is zero at point (θ_0, ϕ_0) on the boundary, it will be zero for all values of ϕ on the circumventing nodal line $\theta = \theta_0$. These spherical harmonics, which are independent of ϕ and with $\mathrm{m} = 0$ are called *zonal harmonics*.

Bubble shapes

The (axisymmetric) shape of a freely oscillating bubble can now be constructed using a summation of zonal harmonics of amplitude A_{n} superimposed on a sphere. This is given by the following expression:

$$R = R_0 + \Sigma A_{\mathrm{n}}\mathrm{Y}_{\mathrm{n}}^0(\theta,\phi)(\theta,\phi) \tag{2.31}$$

Here R_0 is the radius of the undisturbed spherical bubble, A_{n} is a time dependent amplitude and $\mathrm{Y}_{\mathrm{n}}^0$ is the zonal harmonic of order n. The zero-order spherical harmonic $\mathrm{Y}_{\mathrm{n}}^{\mathrm{m}}$, with $\mathrm{m} = \mathrm{n} = 0$, is independent of the angles θ and ϕ and application of equation 2.30 results in:

$$\mathrm{Y}_0^0(\theta,\phi) = \sqrt{\frac{1}{4\pi}} \tag{2.32}$$

By assuming a sphere of radius $R_0 = 1$ and using equation 2.31, it is shown in figure 2.8(a) that the zero-order spherical harmonic describes the volumetric isotropic resonance mode of a bubble. Higher order shape oscillations ($\mathrm{n} \geq 2$) are constructed in a similar way and figure 2.8(b) and 2.8(c) represent the shapes of an oscillating bubble in the $\mathrm{n} = 2$ and $\mathrm{n} = 3$ mode.

Note that Y_1^0 is not presented here, since it differs from the other zonal harmonics. Unlike $\mathrm{Y}_0^0, \mathrm{Y}_2^0$ and higher order harmonics, Y_1^0 is not able to describe a shape oscillation about a fixed point. The Y_1^0 mode and corresponding Legendre polynomial P_1 are used to describe the translation of the bubble as a whole and is referred to as the b_2 mode.

2.3.3 Frequency of shape oscillations

The frequencies of the higher order shape oscillations were studied theoretically by Lamb [6] in 1932. Suppose a vapor bubble of radius $R_{t=0}$ and density ρ_v is perturbed in an oscillatory way in a fluid of density ρ_l. The perturbation $\epsilon(\theta, \phi, t)$ can be described by the zonal harmonic Y_n^0 of amplitude A_n multiplied with a temporal oscillation of frequency ω_n:

$$\hat{R}(t) = R_{t=0} + \epsilon(\theta, \phi, t) = R_{t=0} + A_\mathrm{n}\mathrm{Y}_\mathrm{n}^0 \cos(\omega_\mathrm{n} t + \vartheta) \tag{2.33}$$

From this, expressions for the velocity potential Φ and corresponding pressure inside p_in and pressure outside p_out the perturbed bubble can be derived. Without going into mathematical details, the pressures inside -and outside the bubble as presented by Lamb (where use is made of the expression $P = -\rho\dot{\Phi}$ for an inviscid incompressible potential flow) are given by (Leighton, p. 206 [8]):

$$p_\mathrm{in} = \frac{\rho_v \omega_\mathrm{n}^2 R_0}{\mathrm{n}} A_\mathrm{n} Y_\mathrm{n}^0 \cos(\omega_\mathrm{n} t + \vartheta) \qquad \text{for} \qquad r = R_{t=0} \tag{2.34a}$$

$$p_\mathrm{out} = -\frac{\rho_l \omega_\mathrm{n}^2 R_0}{\mathrm{n}+1} A_\mathrm{n} Y_\mathrm{n}^0 \cos(\omega_\mathrm{n} t + \vartheta) \qquad \text{for} \qquad r = R_{t=0} \tag{2.34b}$$

Since the shape of the perturbed bubble deviates from the spherical, it has two principal radii $\hat{\mathrm{R}}_1$ and $\hat{\mathrm{R}}_2$. The pressure difference across the interface of a perturbed bubble follows from the Young-Laplace equation 2.1 [7] and reads:

$$\Delta \mathrm{p} = \sigma\Big(\frac{1}{\hat{R}_1} + \frac{1}{\hat{R}_2}\Big) \tag{2.35}$$

If we introduce the definition of the sum of the reciprocals of the principal radii $(\frac{1}{\hat{R}_1} + \frac{1}{\hat{R}_2})$ as proposed by Lamb in [6], together with the pressure difference $\Delta \mathrm{p} = \mathrm{p_{in}} - \mathrm{p_{out}}$ into equation 2.35 we obtain the equation of Lamb for the frequencies of higher order oscillations. The equation of Lamb is given by:

$$\boxed{\omega_\mathrm{n}^2 = \mathrm{n}(\mathrm{n}-1)(\mathrm{n}+1)(\mathrm{n}+2)\frac{\sigma}{\Big\{(\mathrm{n}+1)\rho_v + \mathrm{n}\rho_l\Big\}R_{t=0}^3} \qquad \text{with} \quad \mathrm{n} \geq 2} \tag{2.36}$$

Again, ρ_l is the mass density of the liquid, ρ_v is the mass density of the vapor bubble, σ is the surface tension coefficient and $R_{t=0}$ is the initial bubble radius. Note that the zero-order mode of the oscillating bubble has a frequency ω_0 which is given by the Rayleigh-Plesset equation 2.27.

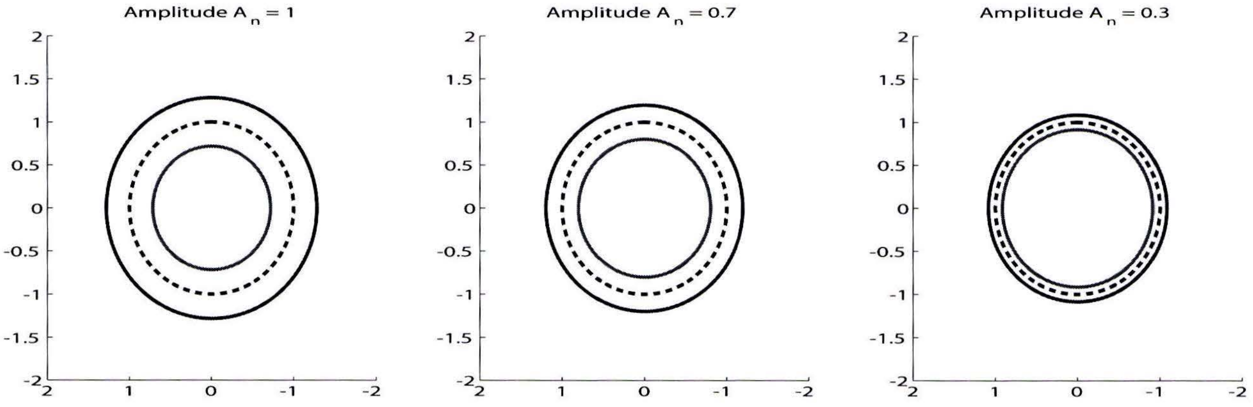

(a) The zero-order axisymmetric spherical harmonic Y_0^0 $(n = m = 0)$ for different amplitudes A_n in 2D. This mode corresponds to the isotropic resonance mode. The blue curve corresponds to $1 + A_n Y_0^0$, the red curve to $1 - A_n Y_0^0$.

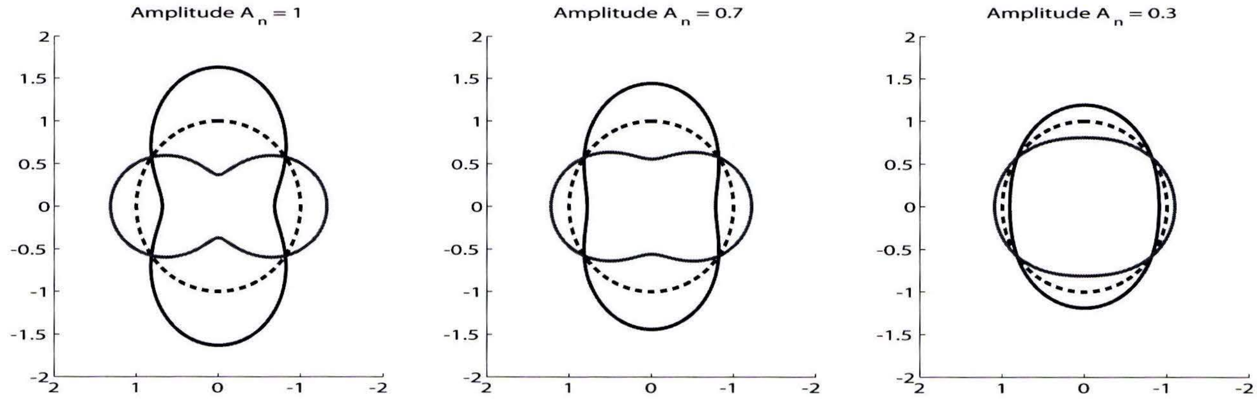

(b) The second-order axisymmetric spherical harmonic Y_2^0 $(n = 2, m = 0)$ for different amplitudes A_n in 2D. The blue curve corresponds to $1 + A_n Y_2^0$, the red curve to $1 - A_n Y_2^0$.

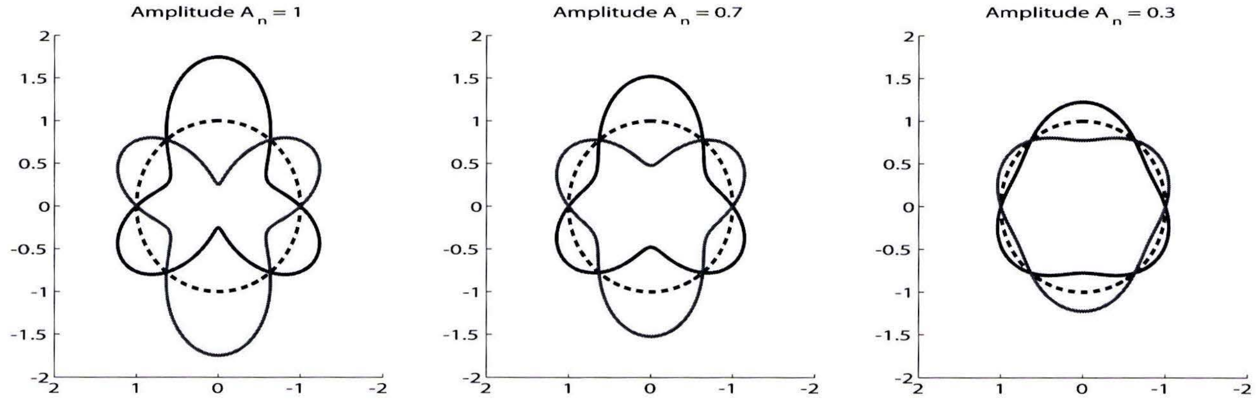

(c) The third-order axisymmetric spherical harmonic Y_3^0 $(n = 3, m = 0)$ for different amplitudes A_n in 2D. The blue curve corresponds to $1 + A_n Y_3^0$, the red curve to $1 - A_n Y_3^0$.

Figure 2.8: Boundary shapes resulting from the linear superimposition upon the unit sphere (dotted black curve) of a zonal spherical harmonic $Y_n^0 (m = 0)$ for increasing amplitudes A_n in 2D. The red and blue curves show the two extreme values. Since the spherical harmonics are zonal, the z-axis is the axis of symmetry.

2.4 Bubble attached to the wall

The previously presented equations for a freely oscillating bubble were derived with the assumption of spherical vapor bubbles. In the case of a bubble attached to the wall, the bubble is not spherical but has a truncated shape and the equations of section 2.3 need to be corrected. Moreover, the proximity of a wall influences the resonance frequencies in such a way that the Rayleigh-Plesset equation needs to be extended (see Van der Geld and Kuerten [32] equation 3.13). Even today it is still an ongoing challenge to find equations describing the oscillations of a bubble during its growth at the wall. Nevertheless, there are some very accurate approximations for the frequencies of a detached bubble very close to a wall which can be used.

2.4.1 Isotropic frequency in the proximity of a wall

It is proved by Van der Geld and Kuerten [32] that the period time T of a freely oscillating bubble increases with decreasing distance to a wall. A first-order approximation of the isotropic frequency of a bubble located in the proximity of a wall is given by Van der Geld and Kuerten as:

$$(1+g_0)^{-1/2}\omega_{RP} \qquad \text{with} \qquad g_0 \overset{\text{def}}{=} \frac{R_{t=0}}{z_{t=0}} \tag{2.37}$$

where $R_{t=0}$ is the initial bubble radius and $z_{t=0} = 2h$ with h the center height of the bubble above the plane wall.

A bubble located very close to the wall experiences a frequency change as a consequence of the induced motion U of the center of the bubble. Equation 2.37 is therefore not valid for bubbles located very close to the wall ($g_0 \geq 0.45$) and the reduced frequency for the isotropic oscillating mode follows from the extended Rayleigh-Plesset equation as presented in Van der Geld and Kuerten [32] in equation 3.13:

$$\omega^2_{RP_{\text{wall}}} = \omega^2_{RP} \Big/ \left\{1 + g_0 - \frac{3}{2} g_0^4 \Big/ (2\alpha)\right\} \tag{2.38}$$

Very close to the wall, the value of the added mass coefficient α is approximated as 0.7 resulting in the following expression:

$$\boxed{\omega_{RP_{\text{wall}}} = \frac{\omega_{RP}}{\sqrt{1 + g_0 - \frac{3}{2.8} g_0^4}}} \tag{2.39}$$

Bubble touching the wall

The reduced isotropic frequency of a spherical bubble touching the wall can now be calculated. In that case we take $h = R$, which leads to $g_0 = \frac{R}{2R} = 0.5$. It follows for the reduced angular frequency:

$$\omega_{RP_{\text{wall}}} = \frac{\omega_{RP}}{1.1971} \tag{2.40}$$

Isotropic deformation of a bubble attached to the wall is only possible with a simultaneous rectilinear motion of the center of mass [33]. The predicted decrease of the isotropic frequency has been observed by Van der Geld *et.al.* (2009) [31] and it will be investigated experimentally in the present work.

2.4.2 Anisotropic frequency of bubble attached to the wall

The anisotropic shape oscillations of a growing vapor bubble at the wall are investigated by Van der Geld [33]. It was found that the frequency of the lowest Lamb mode ω_L (with n = 2) of a vapor bubble is nearly halved when the bubble is attached to the wall (truncated sphere) in comparison with the frequency of a free (spherical) vapor bubble.

The reduced frequency of the shape oscillations is frequently observed in experiments and can be approximated by the following expression [33]:

$$\boxed{\omega_{L_{\text{wall}}} = (1.22193 + 0.15867/\lambda_0^3)^{-1}\omega_L} \tag{2.41}$$

The constant λ_0 is a function of the static contact angle θ_{st} in radians and is defined as

$$0.5\lambda_0^{-1} = \cos(\theta_{st}) \tag{2.42}$$

A typical static contact angle θ_{st} corresponding with our measurements (stainless steel and water) is obtained from the work of Boulangé-Petermann *et.al.* [21] and is found to be $\theta_{st} = 37°$. With this value of the static angle θ_{st}, the frequency of the lowest Lamb mode of a bubble attached to the wall is approximated by:

$$\omega_{L_{\text{wall}}} = \frac{\omega_L}{1.9} \tag{2.43}$$

which corresponds very well with the experimental findings of Van der Geld *et.al.* [31].

2.5 Resonance frequencies during bubble growth

A vapor bubble grows from the minimum bubble radius, in general equal to the radius of the cavity r_{cav}, until it reaches the maximum bubble radius $R_{\max}$ at detachment. The bubble radius increases continuously during the growth, which causes a decrease in the corresponding resonance frequencies.

2.5.1 Frequency change as function of bubble radius

Figure 2.9(a) shows the decreasing isotropic Rayleigh-Plesset and lowest anisotropic Lamb frequency as function of growing bubble radius ($r_{cav} \leq R \leq R_{\max}$). The black dotted vertical line at the left of the figure corresponds to the bubble radius of the diffusion controlled growth $R = r_{cav}$, whereas the black dotted vertical line on the right corresponds to the maximum bubble radius at detachment. The maximum bubble radius at detachment from a cavity of size $r_{cav} = 30\mu$m is calculated with use of equation 2.13 to be $R_{\max} \approx 0.66$ millimeter. The solid curves in the figure show the resonance frequencies of freely oscillating bubbles (equation 2.27 and 2.36 respectively), whereas the dotted curves refer to the corrected resonance frequencies of bubbles growing at the wall (equation 2.40 and equation 2.43 respectively).

The figure shows nicely how the changing bubble radius influences the resonance frequencies. During its growth at the wall, the bubble volumetric frequency (Rayleigh-Plesset) changes from a value above 100 kHz to approximately 4 kHz at detachment, whereas the frequency of the first Lamb mode reduces from approximately 20 Khz to the order of several hundred Hertz before detachment.

2.5.2 Frequency change as function of bubble growth time

Instead of visualizing the decreasing resonance frequencies as function of bubble radius, it is of more interest to show the change of frequency as function of time. To do this, we can make use of equation 2.7 for the diffusion controlled bubble growth as function of time. The inertia controlled growth is neglected, since the growing vapor bubbles are only excited during the diffusion controlled growth. The bubble growth time as function of bubble radius is therefore given by:

$$t = \frac{R^2\pi}{12\mathrm{Ja}^2\alpha} \tag{2.44}$$

where the shape factor $C_s = \sqrt{3}$. With use of this expression we are able to transform figure 2.9(a) into figure 2.9(b), showing the decrease in frequencies as function of the bubble growth time.

A superheating temperature of $\Delta T = 2°$ Celsius results in a bubble growth time of approximately 19 milliseconds. It is shown that due to the rapidly increase in bubble radius during the initial stage of bubble growth, the frequency decreases very fast in the first quarter of the growth and decreases much slower in the last stage of the growth.

σ	$58.91 \cdot 10^{-3}$	[N/m]
ρ_l	958.4	[kg/m^3]
ρ_v	0.598	[kg/m^3]
h_{ev}	$2.2570 \cdot 10^6$	[J/kg]
c_p	$4.216 \cdot 10^3$	[J/(kg·K)]
λ_l	0.680	[W/m K]
α	$1.680 \cdot 10^{-7}$	[m^2/s]
γ	1.4	[-]
c	1450	[m/s]

Table 2.1: Typical values of saturated water (100° Celsius) at standard pressure (1 atm.) [68], [2],[4]

Acoustic excitation

The goal of the present study is to promote the detachment of boiling bubbles from the heater surface, by exciting the growing vapor bubble in its resonance frequency. From figure 2.9(b) it can be concluded that the value of the resonance frequency is more constant near the final stage of the bubble growth, than it is in the initial stage. Therefore, we are exciting the growing vapor bubbles in the resonance frequency corresponding to the final stage just before

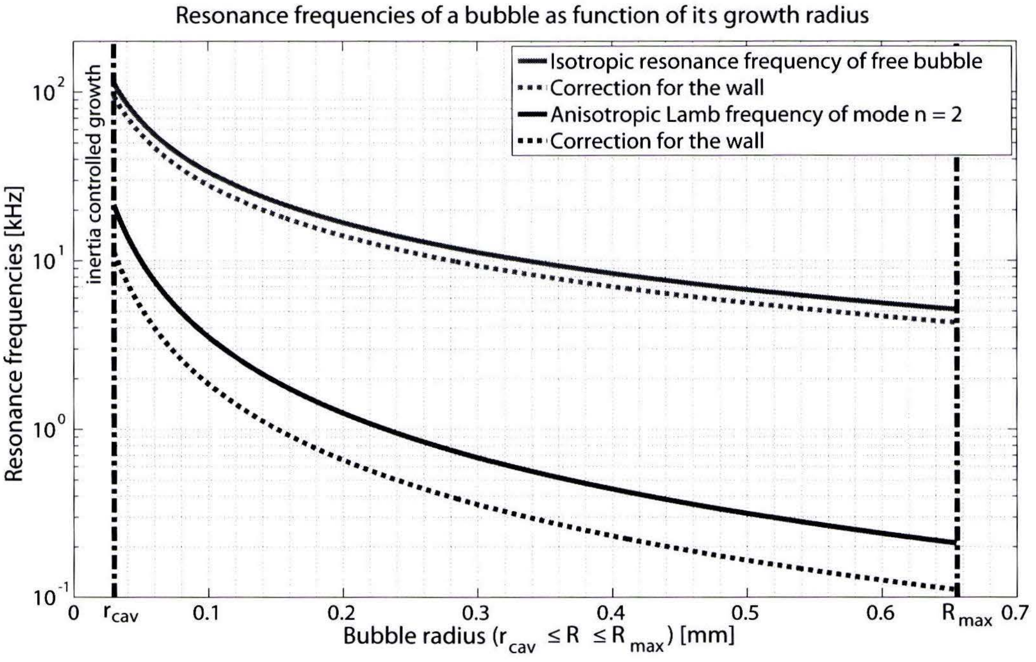

(a) The continuously decreasing resonance frequencies of bubble during its growth as function of the bubble radius. The left dotted vertical line corresponds to the minimum bubble radius $r_{cav} = 30\mu$m, the right vertical dotted line corresponds to the maximum possible bubble radius at detachment $R_{\max}$. Inertia controlled growth occurs for R $< r_{cav}$.

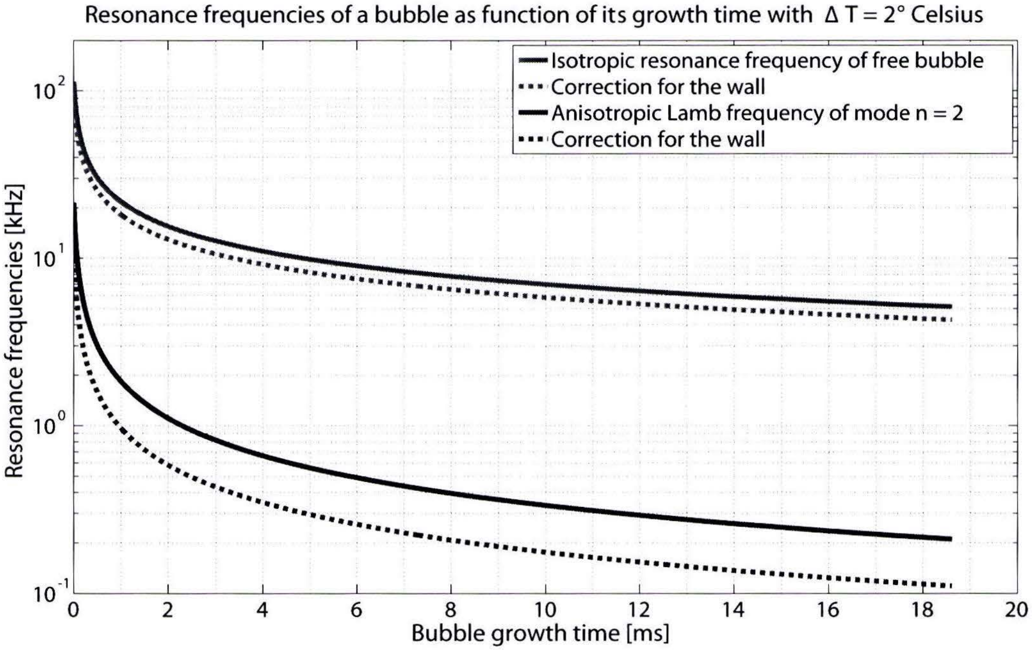

(b) The decreasing resonance frequencies of bubble during its growth as function of bubble growth time. The superheat ΔT equals 2° Celsius.

Figure 2.9: Resonance frequencies (with $\nu = \frac{\omega}{2\pi}$) of bubble during its growth with and without corrections for the wall.

detachment, which corresponds to a frequency in the order of 4kHz for the isotropic mode and a frequency in the order of 100 Hz for the first order Lamb mode.

Note that the resonance frequencies of boiling bubbles with maximum bubble radius as predicted by expression 2.13 of Chesters [23] are located inside the audible range. Instead of ultrasonic excitation, we actually can use sonic excitation. In the remaining of the report we will therefore use the term acoustic excitation.

Chapter 3

Sound propagation

The basic principles of sound and sound propagation will be discussed in this chapter. As a start the theory regarding simple longitudinal sound waves will be treated, which will gradually be extended with phenomena like wave diffraction to construct an ultrasonic sound field. At the end of the chapter some theory about transducers and the application of ultrasound is given.

3.1 Sound

Sound, whether it is a voice, background music or very annoying noise, is characterized by a waveform with density variations in an elastic medium, propagating away of a source [8]. One of the most characterizing properties of sound is the frequency at which it is propagating, measured in cycles per second or Hertz (Hz). The frequency ν is used to categorize sound. To generate a sound, mechanical work has to be done on the medium , *i.e.* the vibrations of a source have to set air into motion. On the other hand, to detect a sound the medium has to do mechanical work on the detecting device.

Whether a sound is detected or not is determined by the frequency and magnitude of the propagating sound wave and the limitations in the frequency range of the detector. The human ear operates in the frequency range of 20Hz-20kHz, though we lose sensitivity for the higher frequencies at a later age. Based on the range of the human ear, the three different terms *infrasonic, sonic* and *ultrasonic* are defined [8]. The term sonic refers to sounds with frequencies in the human ear range, infrasonic refers to sounds with frequencies below 20 Hertz and ultrasonic refers to sounds with frequencies above 20 kHz. No matter at what intensity ultrasonic sound is propagating, we will never hear the sound.

3.2 Simple longitudinal waves

A wave is in general defined as a disturbance that travels through time, accompanied by a transfer of energy [83]. The motion of a wave consists of displacements or oscillations of particles in a medium: the wave itself is traveling from source to detector, whereas the particles merely move. A well known type of wave is the so called transverse wave, which occurs when a droplet hits a water surface (see figure 3.1).

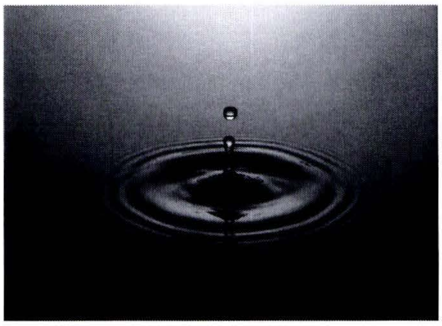

Figure 3.1: Transverse wave in ripples on water surface

The particles in the medium are displaced perpendicular to the direction of wave motion in these types of waves. Sound waves are typically not transverse but longitudinal, where the particles are displaced parallel to the direction of wave motion. In a longitudinal wave, the variations in density occur in the direction of motion, and regions of high pressure (compression) and regions of low pressure (rarefactions) are characterizing.

Figure 3.2 shows an example of a longitudinal wave. The drawing is taken from the book *The acoustic bubble* by T.G. Leighton [8]. The wave is visualized by bobs of equal mass connected to massless springs, which correspond to the inertia and elasticity of the medium a wave is traveling through. Consider the bobs as the particles of the medium.

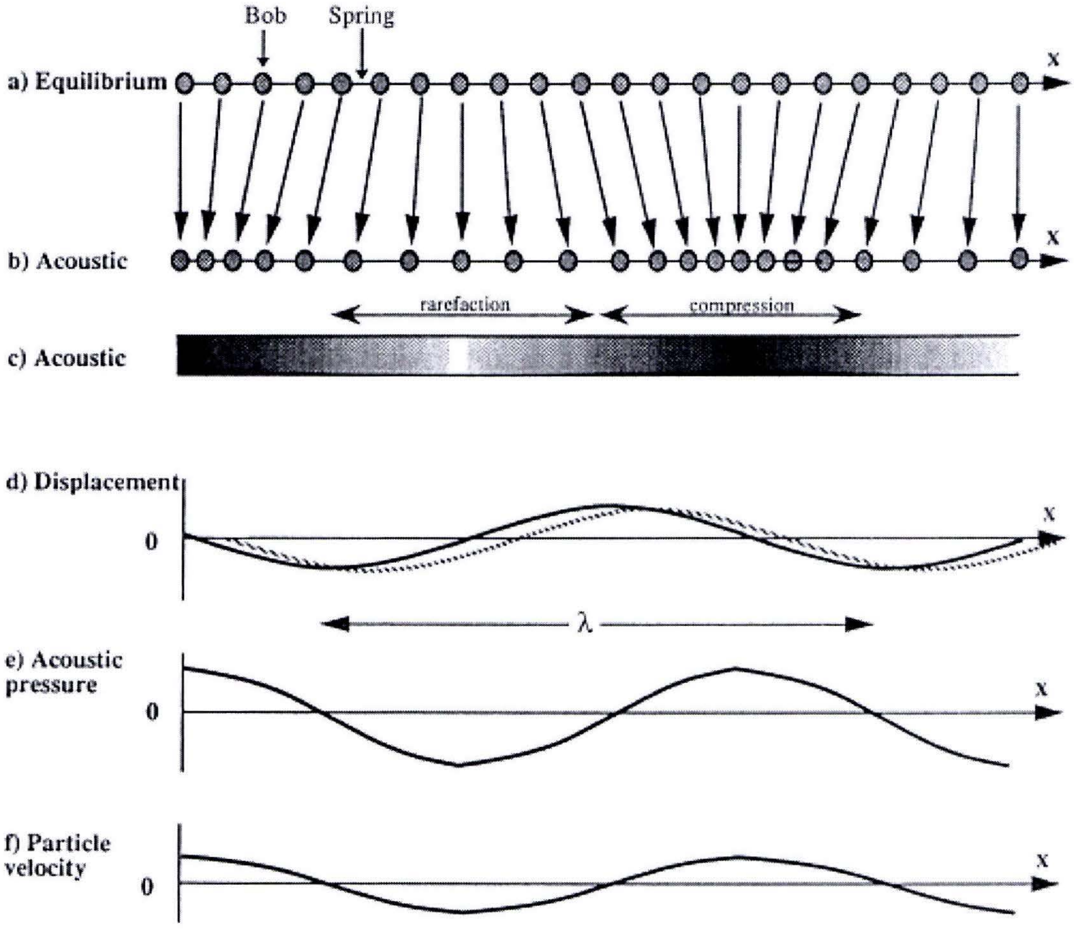

Figure 3.2: Model of longitudinal wave using bobs of equal mass connected by massless springs. (*From "The acoustic bubble"*, 1994. T. G. Leighton, p. 4 [8])

Figure 3.2(a) shows a medium at rest, where the particles are in equilibrium. In figure 3.2(b) a longitudinal wave is propagating through the medium, resulting in the displacement of the particles. The arrows indicate the direction of the particle movement. The displacement of the particles in the direction parallel to the motion of wave propagation results in a variation in the concentration of particles. The particle concentration is given in figure 3.2(c), where the compression and rarefaction regions are indicated. Figure 3.2(d) shows the displacement of the particles with respect to the equilibrium position (solid line). A small time step later, this displacement is given by the dotted line. The wave has propagated in the positive x direction (to the right). The acoustic pressure in figure 3.2(e) corresponds to the regions of compression and rarefaction and has a maximum where the displacement is zero.

3.2.1 Dynamics of longitudinal waves

The longitudinal one-dimensional wave described above is called a simple wave, since in general sound waves travel in three dimensions. For these simple waves the following important relation holds:

$$c = \nu\lambda = \omega/k \tag{3.1}$$

Here, the c is the phase speed of the wave, ν is the frequency of the wave, λ is the wavelength, $\omega = 2\pi\nu$ is the angular frequency and $k = 2\pi/\lambda$ is the wavenumber. Since c is the velocity at which the stress moves from particle to particle, it is equal to the speed of sound in the medium.

Wave equation

The displacement of any wave in one dimension as function of time is given by the second-order linear partial differential wave equation [8]

$$\boxed{\frac{\partial^2\xi}{\partial t^2} = \ddot{\xi} = c^2\frac{\partial^2\xi}{\partial x^2}} \tag{3.2}$$

The parameter $\xi(x,t)$ that satisfies the one-dimensional wave equation, describes a wave which is propagating in the $+x$ or $-x$ direction with phase speed c. The general solution of $\xi(x,t)$ to equation 3.2 is given by

$$\xi = \mathbf{f}_1(ct - x) + \mathbf{f}_2(ct + x) \tag{3.3}$$

The values of $\mathbf{f}_1$ and $\mathbf{f}_2$ are determined by the boundary conditions of the problem. The argument of both solutions can be rewritten in the non-dimensional form using the definitions of equation 3.1 as $(\omega t - kx) = 2\pi(ct - x)/\lambda$. The displacement of a sinusoidal wave in time is therefore in general of the form of

$$\xi_+ = \mathbf{f}_1 e^{i(\omega t - kx)} \qquad \text{and} \qquad \xi_- = \mathbf{f}_2 e^{i(\omega t + kx)} \tag{3.4}$$

where the former solution corresponds to a wave traveling in the positive x direction and the latter in negative x direction.

Impedance

The pressure of the propagating sound wave consists of a steady part and a fluctuating part, where the pressure fluctuations $p(\vec{x},t)$ in the medium are the main concern in acoustics:

$$P(\vec{x},t) = P_0(\vec{x}) + \vec{p}(\vec{x},t) \tag{3.5}$$

For small amplitude sound waves the conservation of momentum holds and the linear inviscid force equation is derived as [10]:

$$\rho_0 \frac{\partial \vec{u}}{\partial t} + \vec{\nabla}\vec{p} = 0 \qquad \text{or} \qquad \vec{u} = -\int \frac{1}{\rho_0}\vec{\nabla}\vec{p}\mathrm{d}t \tag{3.6}$$

If we take the pressure fluctuation $p = \vec{p}(\vec{x},t)$ as the parameter which satisfies the wave equation 3.2, thus $\xi = p$, we arrive at:

$$p_+ = \mathbf{f}_1 \mathrm{e}^{i(\omega t - kx)} \qquad \text{and} \qquad p_- = \mathbf{f}_2 \mathrm{e}^{i(\omega t + kx)} \tag{3.7}$$

It follows with application of equation 3.6 for the particle velocity $\vec{u}(\vec{x},t)$:

$$\vec{u}(\vec{x},t) = \left\{\frac{p_+}{\rho_0 c} - \frac{p_-}{\rho_0 c}\right\}\vec{i} \tag{3.8}$$

with $\vec{i}$ the unit vector. This expression states that for a harmonic wave traveling in positive or negative x direction, the pressure fluctuations are always in phase with the velocities of the particles. This is also shown in figure 3.2.

Now we introduce the term *impedance*, which is the ratio of driving force to velocity response. In acoustics the driving force is the acoustic pressure fluctuation $\vec{p}(\vec{x},t)$, whereas the velocity response is equal to the velocity of the particles $\vec{u}(\vec{x},t)$ in the medium. The acoustic impedance (Z_a) is thus defined as

$$\boxed{Z_a = \frac{\vec{p}(\vec{x},t)}{\vec{u}(\vec{x},t)} = \pm\rho_0 c} \tag{3.9}$$

3.3 Sound intensity

A very important parameter in acoustics is the sound intensity, which is a measure of the loudness or strength of a sonic wave. As discussed before (figure 3.2), sound waves are characterized by regions of high pressure (compression) and regions of low pressure (rarefaction). The pressure is therefore the most important parameter to define the sound intensity.

The intensity of a wave is the rate of flow of energy through a unit area normal to the direction of propagation. It is known from basic dynamics that the instantaneous power equals force time velocity ($\Pi = \vec{F} \cdot \vec{u}$), where the force $\vec{F}$ is a vector acting on a particle with particle velocity $\vec{u}$. The power per unit normal area is given by the instantaneous sound intensity vector $\vec{I'}$ as [10]

$$\vec{I'} = p\vec{u} \tag{3.10}$$

The mean intensity vector $\vec{I}$ can be obtained by averaging over time of equation 3.10:

$$\vec{I} = \frac{1}{T}\int_0^T p\vec{u}\mathrm{d}t = \frac{1}{2}\mathrm{Re}[p\vec{u}] \tag{3.11}$$

Consider the longitudinal plane wave given in equation 3.7 traveling in positive direction. For the fluctuating pressure we have:

$$p_+ = p(\vec{x},t) = \mathrm{Re}[\mathbf{f}_1 \mathrm{e}^{i(\omega t - kx)}] = \hat{p}\cos(\omega t - kx) \tag{3.12}$$

and for the associated particle velocity:

$$u(\vec{x},t) = \mathrm{Re}\Big[\frac{\mathbf{f}_1}{\rho_0 c}\mathrm{e}^{i(\omega t - kx)}\Big] = \frac{\hat{p}}{\rho_0 c}\cos(\omega t - kx) \tag{3.13}$$

Introduction of equation 3.12 and equation 3.13 into equation 3.11 results in the mean sound intensity I:

$$\boxed{I = \frac{\hat{p}^2}{2\rho_0 c} = \frac{p_{\mathrm{rms}}^2}{\rho_0 c}} \tag{3.14}$$

with $\hat{p}$ the acoustic pressure amplitude of the wave.

3.3.1 Intensity -and sound pressure level

To compare the ratio of powers of different sound waves with each other, one can use the bel scale. If two sound signals with power Π_1 and Π_2 are compared, their relative level in bels is given by

$$L_\Pi = \log_{10}\frac{\Pi_1}{\Pi_2} \tag{3.15}$$

The bel scale is a very large unit scale. If the power of one signal is 10^1 times greater than the power of the other signal, there is only one bel difference. More often, the decibel scale is used. In this scale two signals differ one bel if the powers have ratio $10^{1/10}(\approx 1.26)$ [10]. A doubling of the relative powers results in a value of 3 dB. The sound power level L_Π or sound intensity level L_I is given in decibel scale as:

$$L_\Pi = 10\log_{10}\frac{\Pi}{\Pi_0} \qquad \text{or} \qquad L_I = 10\log_{10}\frac{I}{I_0} \tag{3.16}$$

Here Π_0 and I_0 are reference values. The internationally accepted reference values for the sound power and sound intensity are $\Pi_0 = 10^{-12}\mathrm{W}$ and $I_0 = 10^{-12}\mathrm{W/m^2}$ [10] respectively.

From equation 3.14 it is known that $I \propto p^2$. The sound intensity level L_I can be converted into the sound pressure level L_p as:

$$L_p = 10\log_{10}\frac{p^2}{p_{\mathrm{ref}}^2} = 20\log_{10}\frac{p}{p_{\mathrm{ref}}} \tag{3.17}$$

The commonly used reference for sound pressure in air is $p_{\mathrm{ref\ (rms)}} = 2\cdot 10^{-5}\mathrm{N/m^2}$, since it is the threshold of human hearing.

3.4 Acoustic fields

In the preceding we treated the theory of a simple one-dimensional wave traveling in positive or negative x direction. In real acoustic fields a lot more complicated wave phenomena occur and the presented theory has to be adapted. We start with wave diffraction and the consequences for the near-and far field in an ultrasonic field.

3.4.1 Diffraction

All acoustic pressure fields produced by a transducer are affected by three important phenomena: diffraction, attenuation and nonlinearity. Diffraction affects all types of wave propagation in a bounded space and is defined by Sommerfeld for light as [3]: Any deviation of light rays from rectilinear paths which cannot be interpreted as reflection or refraction is called diffraction. The phenomenon diffraction will be discussed in the remaining of this section in more detail based on the principle of Huygens.

Propagating sound waves lose their energy through absorption and by scattering [3]. Absorption is the process where the ultrasound is converted into other forms of energy such as heat. Scattering is the redirection of ultrasound energy by changes in compressibility and density on scales much smaller than the ultrasound wavelength. Attenuation of an ultrasonic wave consists of both absorption and scattering. In the present work we use relative low frequencies (kilo Hertz range) and the medium is water. Under these conditions attenuation is negligible and the energy of the sound wave remains.

Besides attenuation, nonlinearity is an important phenomenon in acoustic pressure field. The propagation of sound waves through a medium is nonlinear. This is caused by the fact that the medium is compressed during positive pressure peaks - with respect to the ambient pressure - and rarefacted during negative pressure peaks. Since the propagation speed of a wave through a medium is related to the density of the medium, the propagation speed of the positive pressure peaks is higher than that of the negative peaks [9]. This results in a distortion of the pressure wave. For low frequencies and low pressure amplitudes, this effect is not sufficiently large and can be neglected.

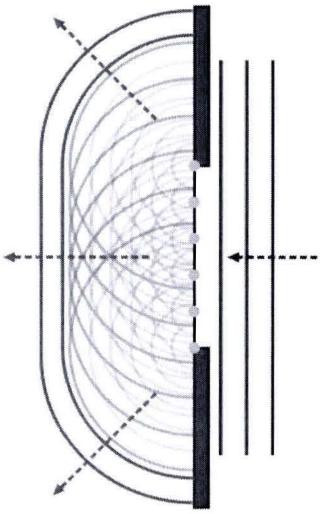

Figure 3.3: Illustration of the Huygens principle [82].

3.4.2 Huygens principle

In practice it is impossible to have just one single wave radiated from a sound source. Namely, every vibrating surface of a sound source can be subdivided into a collection of small point sources, which are radiating spherical wavelets independently. The envelope of all these spherical wavelets corresponds to the wavefront at that instant in time. It was Huygens [36] in 1678 who presented this theory and it is commonly known as the Huygens principle.

The Huygens principle is nicely illustrated in figure 3.3: assume a vibrating piston mounted in a rigid baffle. The vibrating surface of the sound source can be subdivided into six individual point sources (indicated by the dots in the figure). Each point source generates spherical acoustic waves, which are radiating outwards. At this specific moment in time, the envelope of all wavelets shows the propagating wavefront.

3.4.3 Near -and far field

The vibrating surface of a radiating sound source is subdivided into multiple point sources. For the ease of drawing we take S_1 and S_2 as two radiating point sources on the vibrating surface, where the distance between these point sources ($S_1 \rightarrow S_2$) is called the pitch (see figure 3.4). The difference in the traveled distance by two acoustic wavelets from the sound source to an observer O_1 very far away from the source (indicated by the red arrow in the figure) can in general be considered as negligible small as compared to the wavelength. The phase difference between both signals becomes vanishingly small as the observer moves to infinity, since the angle tends to zero [8]. The observer O_1 is located in the so called *far field* of the sound source since the path difference $S_2 \rightarrow P_1 \ll \lambda$.

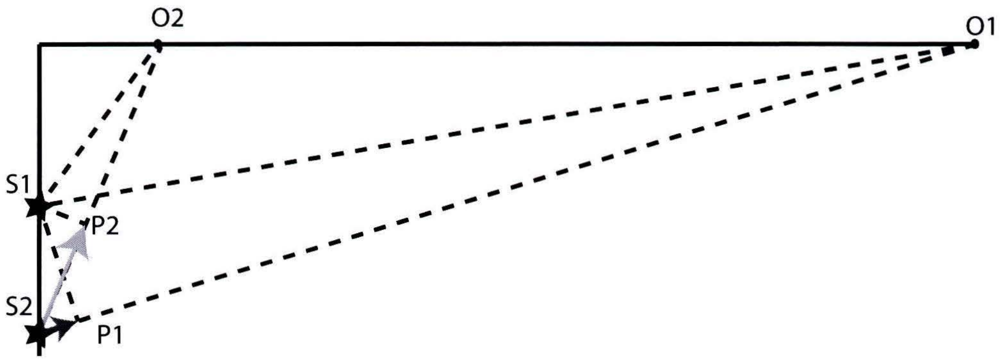

Figure 3.4: Phase shift between two signals as a result of the path difference between point of observation and sound sources.

On the contrary, an observer O_2 close to the radiating sound source experiences a phase shift due to the differences in distance ($S_2 \rightarrow P_2$) traveled by the waves. This path difference (blue arrow in the figure) is in the order of the wavelength λ. Therefore, if all the wavelets from the point sources are summed, the differences in phase have to be included in the calculations as well. The exact value of the path difference depends on the location of the observer O_2. The corresponding sound field close to the radiating sources is much more complicated than further away. The region with complicated wave diffractions and phase shifts is referred to as the *near field* of the ultrasonic sound field. Note that the closer the observer is located to the radiating sound source, the more important the path difference and the more complex the wave diffraction.

3.4.4 Construction of sound field

From the theory presented above, it is not a very big step to the construction of the acoustic field resulting from individual radiating point sources. The pressure at a given point in the sound field can be obtained by a summation of the radiated pressures of each of the infinitesimal point sources together with the induced phase changes at that point [8]. The induced phase difference is given by [8] as:

$$\Delta\phi = 2\pi\frac{\Delta x}{\lambda} \tag{3.18}$$

From this expression it follows that the smaller the wavelength, the greater the distance of the near field region extends. If the pressures in all points of the sound field space are calculated, the pressure field can be mapped.

Rayleigh integral

The Rayleigh integral is commonly used to construct the radiated pressure field. The velocity normal to the vibrating surface (x-y plane) is denoted with v_n and the location of a radiating point source is denoted with the coordinates x_s and y_s respectively (see figure 3.5). $\vec{R}$ is the relative position vector of the observer with respect to the radiating point source and can be written as $\vec{R} = \sqrt{z^2 + (x - x_s)^2 + (y - y_s)^2}$.

The integral is based on the principle of Huygens and without going into further mathematical details (the interested reader is referred to [8] and [11]) the Rayleigh integral is given by:

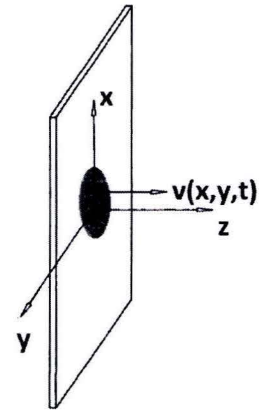

Figure 3.5: Coordinate system as given in [11]

$$\boxed{\vec{p}(\vec{x},t) = \frac{\rho}{2\pi}\int\int\frac{\dot{v}_n(x_s, y_s, t - \vec{R}/c)}{\vec{R}}\mathrm{d}x_s\mathrm{d}y_s} \tag{3.19}$$

3.4.5 Lateral beam profiles

An acoustic field is often analyzed with use of lateral beam profiles, which show the normalized pressure profile in decibel in lateral direction at a certain axial position. In this way the pressure field can be characterized and possible - unwanted - secondary lobes can be visualized. Secondary lobes are caused by sound energy that spreads out from the transducer at angles other than the primary beam. There are two types of secondary lobes: the side lobes and the grating lobes.

Side lobes

Side lobes are the local maxima of the far field radiation pattern that are not the main lobe [9]. Side lobes arise as a consequence of diffraction by the path difference of the traveled waves and gain in importance for wavelengths close to the size of the transducer pitch (see figure 3.4). The pressure intensity of the side lobes is in general low in comparison with the main lobe.

Grating lobes

A special type side lobe is the grating lobe. Namely, grating lobes have much higher amplitudes than side lobes and the amplitude is in general equal - or close - to the amplitude of the main lobe. Grating lobes will occur whenever the size of the pitch is greater than the wavelength. When the distance between the pitch is smaller than half a wavelength, no grating lobes will occur.

Grating lobes arise as a consequence of the Nyquist sampling theorem, which states that perfect reconstruction of a signal is only possible when the sampling frequency is greater than twice the maximum frequency of the signal being sampled [66]. If the sampling frequency is lower than twice the frequency of the signal, the signal can not completely be constructed and information is lost. This results in so called aliasing of the signal.

Since the frequency (time domain) can easily be transferred into wavelength (space domain), the same theory holds for the pitch size of transducers. This is the reason why the pitch size needs to be smaller than half a wavelength. For example: the wavelength of a signal of 2kHz in water is almost 73 centimeters. A normal transducer is always smaller than this wavelength, so no grating lobes are expected to occur. However, the wavelength of a 2 MHz signal in water is 0.73 millimeter. For these signals the pitch is of big importance and grating lobes can occur.

3.4.6 Axial beam profiles

The profile of the pressure distribution at a specific lateral position, for example at the center line, can be visualized with use of an axial beam profile. These profiles can be useful, especially for frequencies in the MegaHertz range, where the axial beam profiles show the location of the near field, the focus point and the far field. In the following section we present the axial beam profile for the present work.

3.5 Numerical simulations

Different parameters such as the frequency, number of radiating point sources, surface of the aperture and the medium determine the ultrasonic pressure field. To illustrate how a change in one of the parameters changes the complete field, some numerical simulations are performed. The numerical code is written in MATLAB and is based on the Rayleigh integral 3.19.

The performed simulations correspond to the pressure fields of the present work with frequencies equal to 70 Hz and 4 kHz. The pressure fields are calculated in a large domain without taking the geometry of the experimental setup into account. It is expected that standing waves occur inside the experimental setup with the used geometry. Nevertheless, the simulations prove that no wave diffraction occurs as a consequence of transducer size and that the total setup is located in the far field of the sound source.

To show the complex pressure field with wave diffraction in the Megahertz range, we performed simulations with an applied frequency of 2 MHz as well. These simulations and some practical issues can be found in appendix B.

A more thorough simulation, where the geometry of the experimental setup is taken into account, is performed using COMSOL. The simulations prove that standing waves occur inside the experimental setup. Moreover, the pressure fluctuations at the position of the heater are calculated and will be presented in the chapter discussion.

3.5.1 Lateral beam profiles of present work

Two different lateral beam profiles corresponding to the pressure field of the present work are given in figure 3.6. The simulations are performed with a rectangular aperture of 100 cm^2 oscillating at 4000 Hz. The first beam profile is calculated at an axial position very close to the aperture. The second lateral profile shows the pressure distribution at a distance of 15 cm in front of the aperture, which corresponds approximately to the location of the bubble generator with respect to the speaker.

The pressure distribution at axial position $y = 0.001$ [m] located very close to the radiating aperture shows one main lobe with a maximum magnitude of 0 dB. The different 'peaks' on the main lobe correspond to the radiated pressure of the individual elements of the transducer and the width of the main beam is equal to the width of the aperture. No diffraction and side lobes occur. This was expected since the wavelengths are equal to

$$\lambda = \frac{c}{\nu} = \frac{1450}{4000} = 0.36 \quad [\text{m}]$$

where the aperture size is almost 4 times smaller. For the case of 2 MHz, the wavelength is 500 times smaller and diffraction of waves occurs. The lateral beam profiles in the Megahertz range can be found in figure B.5 in appendix B.

At the axial position $y = 0.15$ [m] the peak has smoothened and the pressure is more or less distributed equally in lateral direction. The maximum pressure is located at the centerline. The lateral beam profile shows once more that no diffraction occurs at the position of the heater surface.

3.5.2 Axial beam profile of present work

The beam profile in axial direction for the present work is presented in figure 3.6(c). It is shown that the maximum pressure occurs at the vibrating surface and decays rapidly for increasing distance. No near -and far field of the sound source can be observed and there is no focus point. This can of course be expected for large wavelengths with respect to transducer element size.

3.5.3 Acoustic sound field of present work

Figure 3.7 shows the acoustic pressure field corresponding to the present work. For the simulation we used a rectangular aperture of 100 cm^2 oscillating at a frequency of 4 kHz. The aperture has an array of 30 x 30 elements. The acoustic pressure field is calculated in a

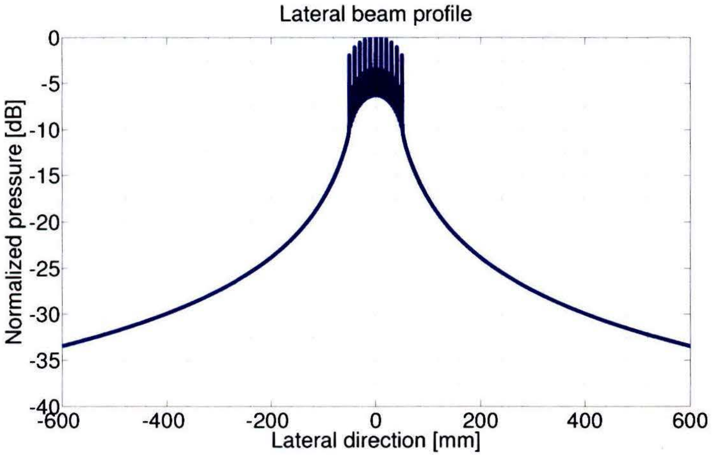

(a) Lateral beam profile at axial direction $y = 0.001$ m.

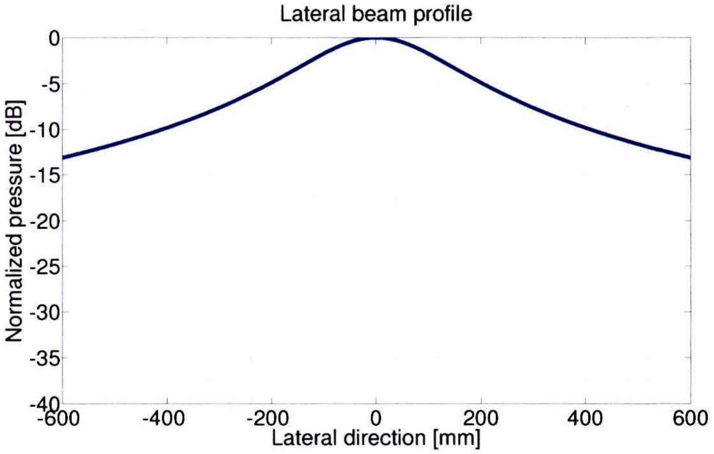

(b) Lateral beam profile at axial direction $y = 0.15$ m.

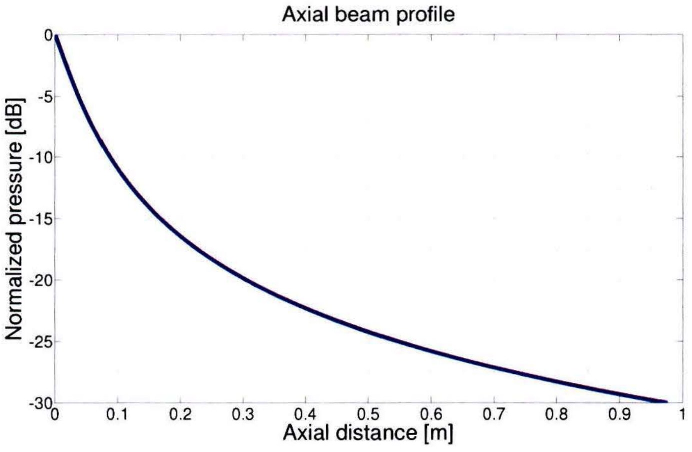

(c) Axial beam profile calculated at the centerline.

Figure 3.6: Lateral -and axial beam profiles corresponding to the present work are calculated at different positions. The pressure is normalized in dB with the maximum magnitude at the corresponding position.

domain of 100 centimeter in axial direction and 60 centimeters in lateral direction. The heated surface in the present setup is located at an axial distance of approximately 15 centimeters in front of the sound source. The bubbles are thus generated in the far field of the sound source, where the pressure amplitude is still sufficient high.

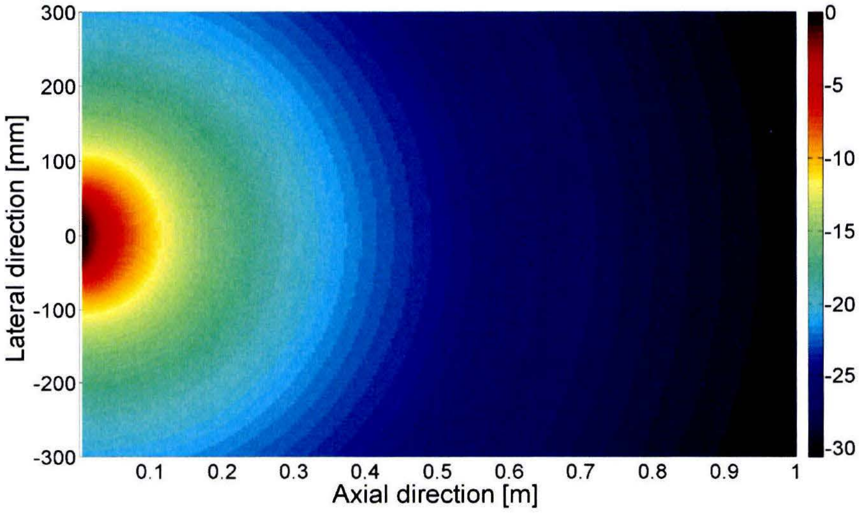

Figure 3.7: Topview of the pressure field radiated from a 100 cm^2 rectangular aperture oscillating at a frequency of $\nu = 4$ kHz.

There is a big similarity between the radiated pressure fields of the simulations with 70 Hz and the simulations with 4 kHz. Therefore the results of the simulation with 70 Hz are not presented here and can be found in appendix B.

Chapter 4

Experiments

Pool boiling experiments are performed with a variety of boiling and applied sound conditions. We start with a discussion of the experimental pool boiling setup. Subsequently, calibration measurements are presented and an error analysis is pointed out. At the end of this chapter we discuss the different heat transfer mechanisms of the setup and derive the corresponding energy equation.

4.1 Experimental setup

The main part of the experimental setup consists of a pool boiling pot extended with a so-called bubble generator, which is used to locally heat up the the bulk and generate boiling bubbles. The bubble generator acts as a single active nucleation site, since an artificial cavity with air pocket is created inside the middle of the heating surface of the generator. Consequently, all generated bubbles depart from the same location and have constant volume and growth times, which makes the analysis much more simple.

The bubble generator is mounted inside the center of the pool boiling pot, where the bulk is at rest. Two different types of bubble generators are available: one providing a constant heat flux, the other a constant surface temperature. Both types will be discussed in the remaining of this section. The generated boiling bubbles in each experiment are recorded for analysis with a high-speed camera with frame rates up to 5000 frames per second. The instantaneous temperature of the bulk is measured with two PT-100 sensors. Figure 4.1 shows an overview of the experimental setup.

4.1.1 Pool boiling pot

The pool boiling setup is constructed from a stainless steel block (141mm x 141mm x 141mm) where holes of Ø 80 mm are drilled through the centers of each side. Two sides and the bottom of the boiling pot are covered by silicon heating elements (the red plates in figure 4.1) which are connected to a temperature control unit. The heating elements heat up both the fluid and the stainless steel pot, to minimize heat losses from the fluid to the surroundings. The temperature control unit makes it possible to control the temperature of the bulk, allowing experiments at different subcooled temperatures.

The remaining three sides of the pool boiling pot are covered by perspex plates which are connected to the boiling pot by bolts. Each cover plate can therefore easily be unmounted and the pool boiling setup can be adapted to the customers needs. In the present setup, two thin PT-100 sensors are inserted through the top cover plate to measure the instantaneous changes in local bulk temperature. Another PT-100 sensor controls the temperature of the bulk via a closed temperature feedback-system. The perspex cover plate at the right side of the pool boiling pot enables a view at the test section for the high speed camera. The pot can be filled with any fluid by removing the top cover plate. A hose is connected to the bottom of the boiling pot to drain it.

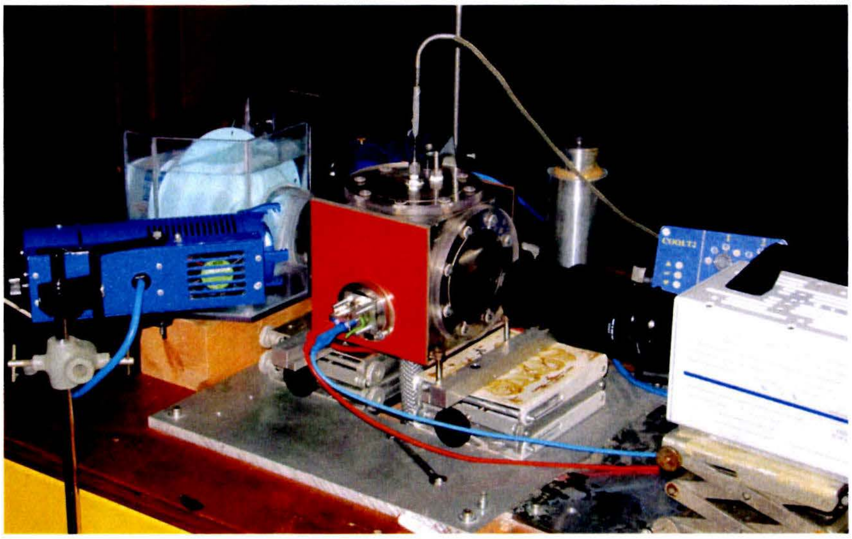

Figure 4.1: The experimental pool boiling setup with the light blue transducer (speaker) located in the extended reservoir (left) and the high speed camera positioned in line with the test section (right). Two high intensity lamps (left) are needed for the recordings with the high speed camera. A PT-100 sensor is inserted through the top cover plate to control the bulk temperature. The red plate shows one of the three silicon heating elements.

4.1.2 Extended reservoir

Since we concentrate ourselves on frequencies in the audible range, we are able to use an ordinary swimming pool loudspeaker as transducer. To integrate the speaker into the setup, we had to extend the boiling pot with an extra reservoir. The reservoir is filled with the same liquid as the boiling pot, to make sure that there is no difference in impedance between the reservoir and the pot.

A drawback of the relative low frequencies in the audible range (order of several thousands Hertz) is the large wavelength of the waves. Consider the case of saturated water which is excited by sound waves with a frequency of 4500 Hz. The resulting length of the waves in the water corresponds to:

$$\lambda = \frac{c}{\nu} = \frac{1450}{4500} \approx 0.32 \quad [\mathrm{m}] \tag{4.1}$$

It is clear that these large waves do not fit inside the pot and standing waves are expected to occur in the experimental setup. During the design of the reservoir we tried to minimize the standing waves in our setup, however there were limitations in the geometry.

Reservoir design

The dimensions of the reservoir are adapted to the diameter of the speaker (Ø 180mm), to make sure that the speaker fits precisely inside the setup with its center placed in line with the bubble generator and the high speed camera. The speaker is clamped inside the reservoir with isolation foam, which acts as a damper to minimize vibrations of the speaker.

For recordings with high frame rates (more than 3000 frames per second) an enormous amount of light is needed. In the experimental setup without the reservoir - as was used in previous works - a single high intensity lamp was placed in line with the camera. A smooth white background needed for the numerical analysis of the bubble recordings was created by a white milk glass-sheet. Unfortunately, with the extended reservoir it was no longer possible to place the high intensity lamp in line with the white milk glass-sheet and the high-speed camera. The challenge to create a smooth white background with sufficient light for high frame-rate recordings resulted in the design of the reservoir as sketched in figure 4.2.

Between the connection of the reservoir with the pool boiling pot, a white balloon is clamped as a membrane. The white balloon distributes all incident light over its surface to obtain a smooth white background. Furthermore, the balloon separates the fluid in the pool boiling pot with the fluid in the reservoir, thereby preventing a fluid flow between both parts of the setup. Since the thickness of the balloon is much smaller than the wavelengths of the waves, the sound field is not disturb by the membrane.

To optimize the positioning of the high intensity lamps with respect to the membrane, the reservoir of figure 4.2(b) has two oblique sides under an angle of 30 degrees providing enough space to adjust the positioning. Later, the geometry of the reservoir was adapted and the oblique angles were removed as is shown in figure 4.2(c). In the rectangular reservoir the speaker is directly connected to the horizontal cylinder, which diminish standing waves inside the reservoir.

The reservoir is made of polycarbonate and the glue can resist more than hundred degrees Celsius. To prevent heat losses to the surroundings, the reservoir is completely covered by thick isolation material. The reservoir is connected to the boiling pot by one of the perspex cover plates as illustrated in figure 4.2(a).

4.1.3 Single bubble generator

All boiling experiments are performed with use of single bubble generators, which are designed and produced at the Eindhoven University of Technology. The bubble generators create equally sized single bubbles, departing from an artificial nucleation site. In this way the effects of acoustic excitation on single vapor bubbles can be examined. There are two different types of bubble generators: the stainless steel bubble generator and the thin film bubble generator.

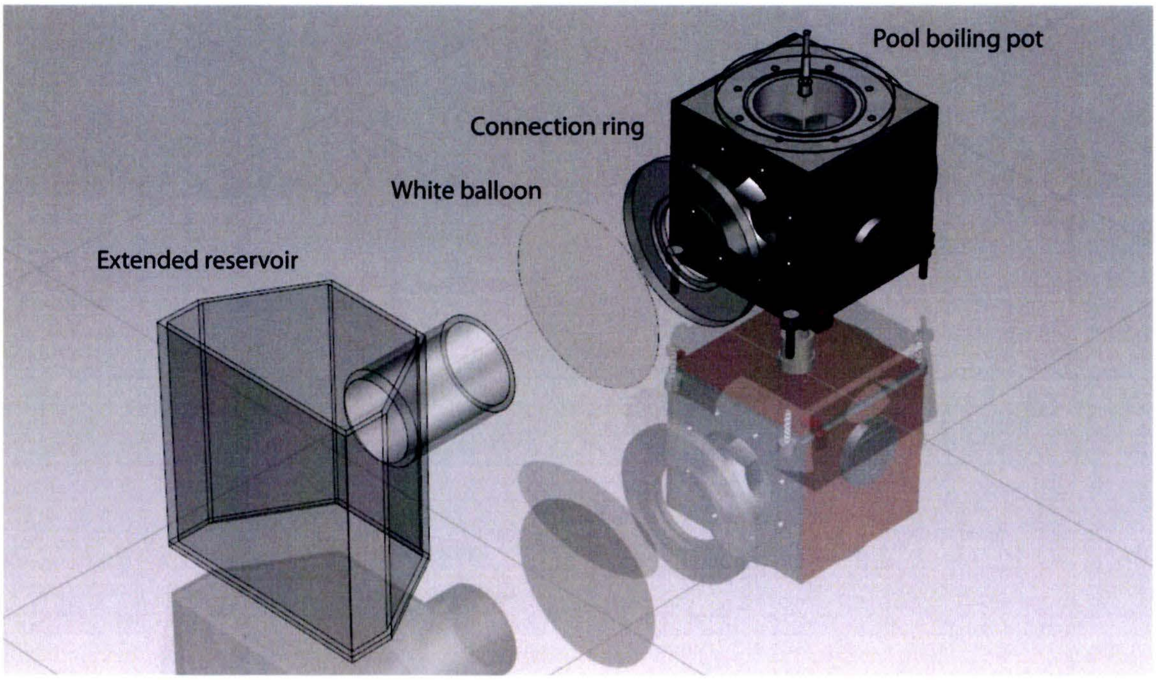

(a) Exploded view of the connection between reservoir and the pool boiling pot with a white balloon as membrane. The perspex connection ring is bolted to the boiling pot, whereas the balloon is clamped between the reservoir and the ring with silicon glue.

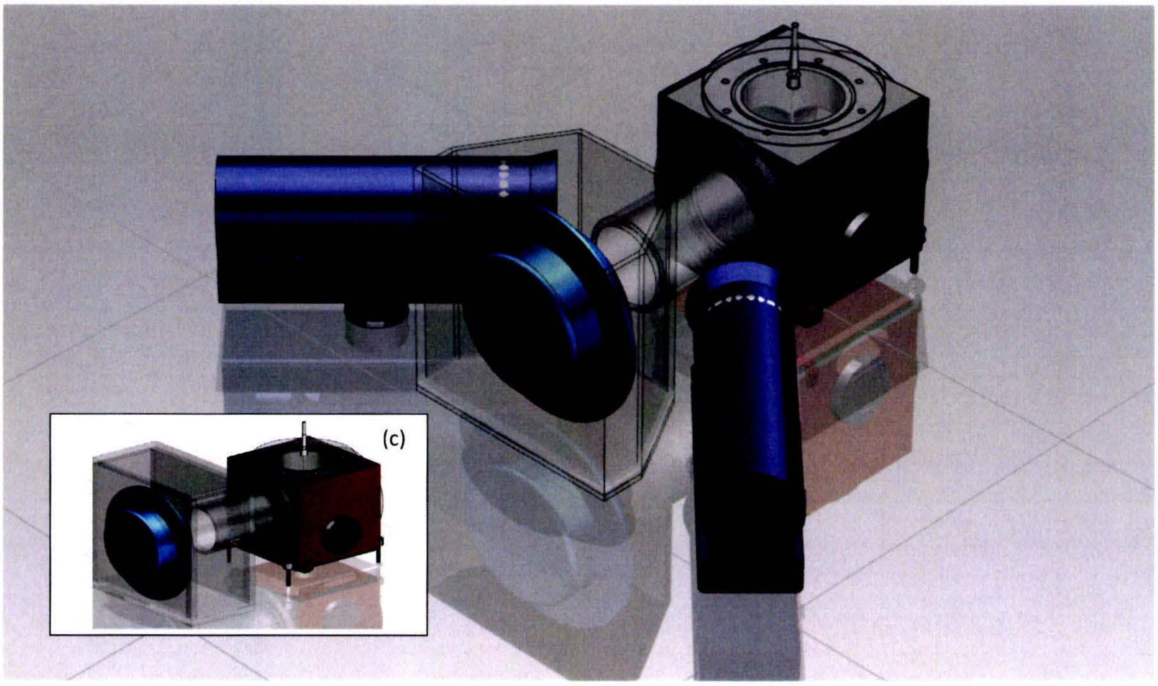

(b) Assembled experimental setup with the reservoir connected to the boiling pot. Figure 4.2(c) shows the rectangular reservoir, which is the follow up of the reservoir with the oblique sides.

Figure 4.2: Experimental setup with extended reservoir, speaker and high-intensity lamps. Designed in the CAD/CAM program Unigraphics.

Both types of bubble generators are based on the same working principle: a thin sheet of conductive material is mounted on top of a piece of non-conductive and isolating material. Inside this non-conductive material a pocket of air is made. A (conical) hole with diameter in the order of several micrometers is sparked through the thin sheet of conductive material until it reaches the air pocket. This hole is the artificial cavity.

The non-conductive and isolating material ensures that the heat is located mainly in the conductive sheet. If the conductive sheet is connected to a power source, the pocket of air is heated up and the artificial cavity acts like a boiling nucleation site. Two types of boiling bubble generators are available. The thin film bubble generator has a constant wall temperature, whereas the stainless steel bubble generator generates a constant heat flux. The experiments in the present work are performed with use of the more robust stainless steel bubble generator.

4.1.4 Stainless steel bubble generator

The stainless steel bubble generator (in the remaining we will use the abbreviation SSBG) is a robust bubble generator made of stainless steel. The bubble generator is constructed on a stainless steel holder which positions the SSBG in the exact middle of the pool boiling pot. A close-up photograph of the heating surface of the stainless steel bubble generator is shown in figure 4.3. The technical drawings of the SSBG are given in figure F.4 in appendix F.

The SSBG has a thin sheet of stainless steel on top of its surface. The thin sheet is surrounded by non-conductive and isolating glue. In the middle of the stainless steel sheet a contraction is made which has a higher resistance. A hole (Ø 40 μm) is sparked through the contraction of the thin sheet to connect it to the underlying artificial air pocket. If a constant current is applied to the bubble generator, the contraction (surface = 1 mm^2) in the thin sheet heats up to a superheated temperature due to the higher resistance. Since an artificial cavity with air pocket is created in the middle of the contraction, bubbles start to grow in the exact middle of the bubble generator and the pool boiling pot.

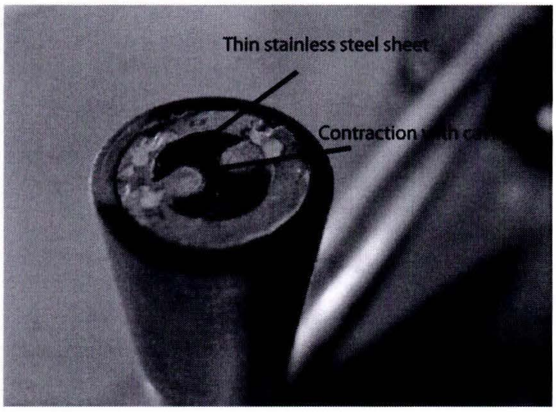

Figure 4.3: Stainless steel bubble generator with close up of thin sheet and cavity located in the exact middle of the bubble generator

Wall temperature

The stainless steel bubble generator has an internal thermocouple approximately 200 μm below the heated steel sheet to measure the wall temperature. The internal thermocouple is not as accurate as one wishes: since the heat is conducted from the steel sheet to the thermocouple, an instantaneously registration of changes in the temperature of the steel sheet is prevented. Furthermore, it can not completely be excluded that the measured temperature is not influenced by the temperature of the surrounding steel holder. Since we compare different measurements with each other, it can be assumed that the error of the internal thermocouple is the same for all experiments. The internal thermocouple has a delay of several seconds when the temperature is changing rapidly [78].

Another drawback of the SSBG is the glue used. The glue bulges under influence of high temperatures and from time to time it has to be grind off to ensure a flat surface of the bubble generator. After some time leakage can occur as well. Figure 4.3 shows a nice example of the influence of heat on the glue after a while.

4.1.5 High speed camera

For the analysis of the bubble growth with -and without sonic excitation, the bubbles are recorded with a high speed camera. The camera used is a Photron Fastcam SA3 [81], which is able to record with frame rates up to 20000 frames per second depending on the amount of incident light and resolution. The amount of light is the main concern in our setup and a frame rate of 5000 frames per second is the maximum possible recording speed for a sufficient resolution. However, the higher the frame rate, the shorter the maximum recording time. A good comprise can be found in recordings with a frame rate of 3000 frames per second with a camera resolution of 512 x 256. Depending on the amount of incident light, a record time of approximately 7 seconds is achieved.

The camera is able to do an endless record, which means that the camera stores all recorded data of the last 7 seconds in its internal memory and overwrites the data for the subsequent 7 seconds. This process continues until the camera is triggered. For our measurements we recorded boiling bubbles without acoustic excitation with an endless record until the acoustic waves were applied and the camera was triggered.

The resulting recordings show the undisturbed boiling bubbles for the last 3.5 seconds before the triggering and the disturbed boiling bubbles for the subsequent 3.5 seconds after the triggering. In this way it can easily be observed if acoustic excitation influences the boiling bubble behavior.

4.1.6 Sound setup

The sound setup consists of three main components: a waveform generator (Agilent 33120a), a power amplifier (Peavey GPS 3400) and a speaker (Lubell UW30). The arbitrary wave form generator is used to generate the signal (a continuous sinusoidal wave with corresponding frequency) and can be controlled manually or with a computer. The wave form generator triggers the high speed camera. The power amplifier is a guitar amplifier and can easily be connected to the used loudspeaker. The amplifier is able to amplify the signal from the wave generator with +32 dB which corresponds to a factor 40. The loudspeaker is designed to operate in water with a frequency range of 100Hz - 10kHz and can resist temperatures up to hundred degrees Celsius. A maximum of 30 Watt continuous power can be applied to the present speaker (this corresponds to an applied voltage of approximately 22 Volts).

4.2 Experimental approach

The bubble radius is by far the most important parameter in bubble growth and in the bubble dynamics. Since the bubble growth is proportional to the square root of time ($R \propto \sqrt{\alpha \pi t}$) and the resonance frequencies of the bubbles are proportional to the radius squared or cubed, we discussed that we should excite the bubbles in the last stage of the growth. Furthermore, the surface tension force is much weaker for bubbles at the end of the growth than at the beginning of the growth, which should make it more easy to detach the bubbles.

4.2.1 Experiments

Before the start of each experiment, the fluid was degassed and kept at the desired bulk temperature via the closed temperature feedback system. The experiments are performed using the stainless steel bubble generators, since these bubble generators have a constant heat flux, which makes the analysis easier.

During the experiments we generated constant 'bubble-trains' - consisting of bubbles of constant volume, growth times and waiting times - by applying a constant power on the bubble generator. The constant bubble-trains are recorded with the high speed camera in the endless recording mode. An estimation of the bubble radius at detachment results in an estimation for the corresponding resonance frequency of the bubbles growing at the wall.

The growing bubbles are excited by acoustic waves within a range of frequencies corresponding to this estimation, until some effect is observed. The range varies from frequencies close to the predicted values, to frequencies further away from the predicted values, to investigate the frequency dependence of the sound on bubble detachment.

4.3 Data processing

During all measurements with the stainless steel bubble generators, the data of the internal thermocouple and the two PT-100 sensors was logged in *Labview* with a frequency of 5 Hz. The resulting output is loaded into MATLAB where the data is processed. The recordings are analyzed by hand in the high-speed camera software program.

4.3.1 High speed recordings

The bubble recordings are analyzed frame by frame for each experiment. The growth time of each bubble is determined by counting the number of frames where the bubble was attached to the wall. The number of frames in between two adjacent bubbles is a measure for the waiting time. If the frame rate is known, the number of frames can easily be converted into time.

The pixel width and height of each bubble are determined by hand as indicated in figure 4.4. With use of the high-speed camera software, a box was drawn around the first bubble (see the dotted box in the figure). This box was constrained during the remaining of the recording. The constrained box makes it easier to observe changes in bubble sizes during the experiment. Moreover, the boundary of the wall (horizontal solid line in figure 4.4) is constrained during the recordings as well. Note the reflections at the bubble boundary, as a result of the reflections of the high intensity lamps on the polycarbonate cylinder. With tape we tried to minimize these reflections.

The volume of the bubbles is estimated by assuming axisymmetry and an ellipsoid bubble shape. The volume of an ellipsoid can be calculated with the expression

$$\boxed{V = \frac{4}{3}\pi abc} \tag{4.2}$$

where a and b are the width halved and height halved respectively (see figure 4.4). Note that $a = c$ since axisymmetry is assumed.

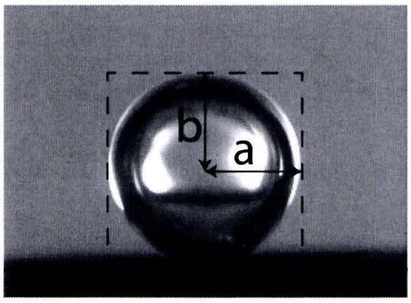

Figure 4.4: Determination of pixel width and height.

4.4 Calibration

The different performed calibration measurements and the thereby obtained relations are presented in this section.

4.4.1 Stainless steel bubble generator

The wall temperature of the stainless steel bubble generator with internal thermocouple is logged in *Labview*. For a correct value the thermocouple has to be calibrated first. This is done with use of a thin PT-100 sensor mounted on top of the thin sheet of the SSBG.

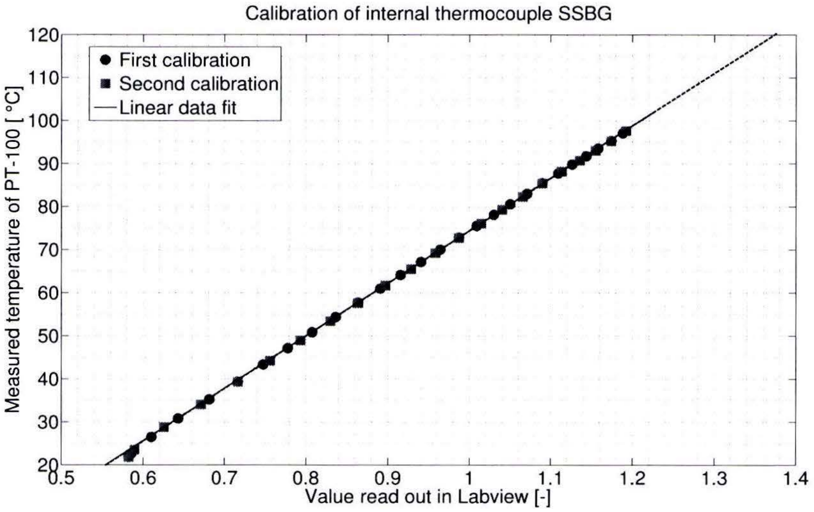

Figure 4.5: Calibration of internal thermocouple of the stainless steel bubble generator. The horizontal axis shows the output of the thermocouple whereas the vertical axis shows the measured temperature of the PT-100 sensor mounted on top of the thin sheet.

During the heating up of the bulk to saturation temperature, the output of both the PT-100 sensor and internal thermocouple were read out simultaneously. Plotting both signals as function of each other results in a linear relation as shown in figure 4.5.

The calibration is done twice and a data fit is applied to obtain the following relation:

$$T_{\text{wall}} = 122x - 47.55 \tag{4.3}$$

4.4.2 Pixel to millimeter ratio

Most of the bubble experiments are recorded with pixel resolutions of 512 x 256. To make an estimation of the bubble volume, the ratio of pixels to millimeter has to be calculated. This can be achieved by placing a glass calibration sphere, with a very accurately known diameter, in the bulk near the place where the bubbles are generated. The glass sphere has a diameter in the order of the created bubbles. An image of the calibration setup is shown in figure 4.6.

Every time the camera was moved, the diaphragm was changed or a small correction in the focus of the camera was applied (for example after switching to another type of bubble generator), the pixel to millimeter ratio had to be recalculated.

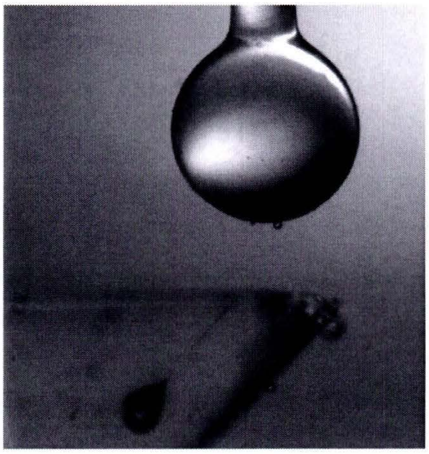

Figure 4.6: Calibration of pixel to millimeter ratio using glass ball with known diameter

For the measurements with the stainless steel bubble generator we obtained the values as presented in table 4.1, where r_x is the diameter of the glass ball, r_p is the number of pixels and Δ corresponds to the absolute uncertainty. The pixel to millimeter ratio is given per experiment in the remaining.

	$r_p \pm \Delta r_p$ pixels	$r_x \pm \Delta r_x$ mm
error estimates	222 ± 2	3.10 ± 0.01

Table 4.1: Calibration uncertainties

The conversion factor C is equal to

$$C = \frac{\text{millimeters}}{\text{pixels}} = \frac{3.10}{222} = 0.0140$$

The relative uncertainty of the conversion factor ΔC can be calculated using the expression of Squires [13]

$$\frac{\Delta C}{C} = \sqrt{\left(\frac{\Delta r_p}{r_p}\right)^2 + \left(\frac{\Delta r_x}{r_x}\right)^2} \tag{4.4}$$

The pixel to millimeter ration is thereby equal to 0.0140 ± 0.0010

4.4.3 PT-100 sensors

The PT-100 sensors used in the experiments are calibrated by the manufacturer. The sensors are connected to a data acquisition system and the output is logged in *Labview*. The linear relation which converts the output voltage of the PT-100 sensors into temperature is given by

$$T_{\text{PT-100}} = 62.10x - 4.507 \tag{4.5}$$

4.5 Error analysis

The different errors of the components of the setup are discussed here. The error made in the determination of pixel size and growth times is treated here as well.

4.5.1 Temperature

The Pt-100 (class C), which is coupled to the temperature feedback system and placed in the bulk, is calibrated by the manufacturer. The maximum possible error of the PT-100 sensor is equal to ± 0.1° Celsius. An extra error is introduced by the digital controller, which is at maximum 0.2 %. [78]

The two thin PT-100 sensors are calibrated by the manufacturer and the absolute error is equal to ± 0.05° Celsius. The time response is very quick and sudden changes in temperature are registrated in less than the sampling rate in *Labview* (5 Hz). There is no time delay in the temperature plots of the bulk.

The thermocouple of the SSBG1 is calibrated with one of the thin PT-100 sensors and has an error of ± 0.2 ° Celsius. The thermocouple is mounted inside the steel holder of the bubble generator at a distance of approximately 200 μm below the heated surface. As a consequence, the measured temperature is not necessarily the surface wall temperature and the internal thermocouple has a delay of several seconds when the temperature is changing rapidly. This is due to the well known inverse heat problem [78]. To account for this time delay, we plotted the temperature profiles for 2 more seconds than the time of the recorded images. In this way we should be able to see a change in the heater wall temperature after the trigger.

Since we compare the situation with sound to the situation without sound in one single experiment, it is of interest to see if acoustic excitation changes the bulk or superheat. The relative errors of the temperature sensors are the same in all experiments and not of importance when only the change in temperature due to the sonic waves is investigated. The errors in the temperature sensors do play a role however, when we want to make calculations on the heat transfer in chapter 6. The error in superheat is maximum ± 0.2 ° Celsius, corresponding to the internal thermocouple.

4.5.2 Applied power

We apply a constant power to the stainless steel bubble generator. This power can be adjusted with an accuracy of one digit. The relative error in applied power is therefore equal to ± 0.05 V and ± 0.05 A. Moreover, it is not sure that all applied power is consumed by the thin sheet. Heat losses in wiring and through the steel holder to the surroundings are not taken into account. Once more we can concluded that this error is the same in all experiments and the error is only of importance when calculating the heat transfer.

4.5.3 Sound

The sound setup has a lot of errors, which are very hard to quantify. The response of the speaker to frequencies (transition function) is unknown and errors in the amplitude of the radiated sound wave can occur. Moreover, the losses of the sound to the surroundings are not mapped. There are losses via the air, the table etc. since we need to wear ear plugs during the excitation. These losses are not taken into account in the simulation of the pressure field inside the pool boiling pot, resulting in large pressure amplitudes. The neglecting of the losses leads to huge errors in the calculated pressure field.

On the contrary, the frequency can be adjusted with a very high accuracy (more than 5 digits). The error of the wave generator is given by the manufacturer as 20 ppm in 1 year for the frequency generation and 1 % in the output amplitude.

4.5.4 Determination of pixels

The size of the bubbles is determined by the number of pixels. The numbers of pixels follow from the high speed camera recordings, where the pixel to millimeter ratio is calibrated with the glass sphere. The error in the determination of the pixels is equal to 2 pixels in bubble width - corresponding to an error of 1 pixel in bubble radius - and 1 pixel error in bubble height. For the determination of the growth times and waiting times, the number of frames is counted. Here, an error of maximum one frame occurs.

Experiments are performed with two types of stainless steel bubble generators: one has a cavity radius of 20μm, the other has a cavity radius of 30μm. The bubbles generated by the bubble generator with the largest cavity are in the order of 150 pixels in width and 170 pixels in height. The maximum possible error in the determination of the radius is one pixel, which is equal to 0.0140 millimeter (as is obtained by the calibration with the glass sphere). The relative error in the determination of bubble radius is equal to $2/150 = 1.3$ %. The error in bubble height is equal to $1/170 = 0.6$ %. The bubble growth times are typically in the order of 28 frames. The error of 1 frame is therefore equal to 3.6 %.

In the case of the smaller generated bubbles the errors are larger. The width of the smallest bubbles is equal to 91 frames, corresponding to an error in bubble radius of 2.2 %. The minimum height of the bubbles is equal to 100 pixels. The error in bubble height is therefore equal to $1/100 = 1$ %. The error in the determination of the growth times is equal to $1/18 =$ 5.6 %. Error bars corresponding to these values are introduced in the figures.

An error is introduced by assuming ellipsoid bubble volumes. The error is the same in all experiments (width/height ratio is approximately the same for all bubbles). Therefore this error is not of importance by comparing the different bubble volumes with each other. The error only plays a role in the analysis of the heat transfer. However, as will be presented in chapter 6, this error has no influence on the heat transfer.

4.6 Heat transfer mechanisms

During nucleate pool boiling various heat transfer mechanisms occur. The two most important mechanisms are (micro-)convective heat transfer and the energy transport by the vapor bubbles. Both mechanisms will be discussed in the following subsections and the total energy equation will be derived.

4.6.1 Heat transport by vapor bubbles

A growing vapor bubble extracts heat from its surroundings. This can either be the surrounding saturated liquid or the heated wall. Due to the large latent heat of the liquid (in the order of MJ/kg for water) a substantial part of the required heat flux will be extracted from the heated wall. The vapor bubbles that rise from the heated surface transport an amount of heat flux away from the heater into the liquid. The heat flux transported by the vapor bubbles q''_{bubbles} is given in [12] as:

$$\boxed{q''_{\text{bubbles}} = \rho_v \cdot V_{\text{bubbles}} \cdot h_{ev} \cdot f \cdot N''_a \quad [\text{W/m}^2]} \tag{4.6}$$

where ρ_v is the mass density of the vapor [kg/m^3], V_{bubbles} the volume of the departing vapor bubble [m^3], h_{ev} the latent heat of evaporation [MJ/kg], f the bubble departure frequency [Hz] and N''_a is the nucleation site density [$\#/cm^2$].

In general the primes $''$ refer to value per unit area. The total power in Watts transported by the vapor bubbles is therefore given by $Q = q'' \cdot A$. The same analogy holds for the number of active nucleation sites per unit area N''_a. In the following we will use $N_a = N''_a \cdot A$ to denote the total number of active nucleation sites.

4.6.2 (Micro)-convection

Bubble incipience -and departure from the heated wall disrupts the thermal boundary layer. A rising vapor bubble drags hot liquid from the thermal boundary layer into the colder bulk of the liquid, which has to be compensated by a colder liquid flow from the bulk to the heater. The colder liquid is pushed to the heated wall and acts as a cold liquid impinging jet, which increases the heat transfer from heater wall to the liquid [12]. The colder liquid reduces the effective thickness of the thermal boundary layer.

It is obvious that the more often a vapor bubble is formed and departs, the more often the thermal boundary layer is disrupted and cold liquid is transported from bulk to heater. Increasing the detachment of the bubbles and thereby the departure frequency of the bubbles results in a higher nucleate boiling heat transfer rate.

Convection

The total heat transfer from heated wall to fluid by convection - which is equal to all heat transfer minus the heat transported by the vapor bubbles - can be written as:

$$\boxed{q''_{\text{convection}} = h \cdot (T_{\text{wall}} - T_{\text{bulk}}) \quad [\text{W/m}^2]} \tag{4.7}$$

where h is the heat transfer coefficient [W/(m^{2}K)]. Increasing the heat transfer coefficient h for a constant ΔT results in a better convective heat transfer.

4.6.3 Heat flux induced by transducer

A transducer converts one form of energy into another. In the present setup we use a speaker which converts electrical energy into vibrational motion. This process is always accompanied by energy losses, in the form of heat generation. Furthermore, the sound waves can lose their energy to the surroundings in the form of heat. The additional heat generated by the speaker and the sonic waves has to be included into the total energy equation. In the remaining of this section we denote the additional generated heat as Q_{sound} [W].

The additional heat of the speaker is estimated by measuring the temperature increase of the bulk during sonic excitation. The temperature of the bulk is logged for several minutes without sound, followed by several minutes with sound. Two PT-100 sensors are used to measure the instantaneous temperature at different positions in the setup.

The bulk is measured at an almost saturated temperature of 99.2° Celsius. Due to the slow temperature feedback system, large temperature fluctuations occurred and no convincing conclusions could be drawn (see appendix C). To minimize the fluctuations, we performed the same measurement at room temperature with the heaters turned off.

Figure 4.7 shows the measured bulk temperature as function of time. The region between the thick vertical black lines indicates the period where the sound was turned on. The bulk temperature is measured at two positions: close to the bubble generator and at five millimeters in front of the speaker.
The blue curve shows the measured temperature of the bulk at a distance of five millimeters in front of the speaker. At this position a small increase in temperature is visible during the period the speaker was turned on. However, the PT-100 sensor located very close to the bubble generator did not registrated any change in temperature.

The temperature increases approximately 0.02° Celsius during sonic excitation. This increase is a consequence of the heat generation by the speaker (for example the heating up of

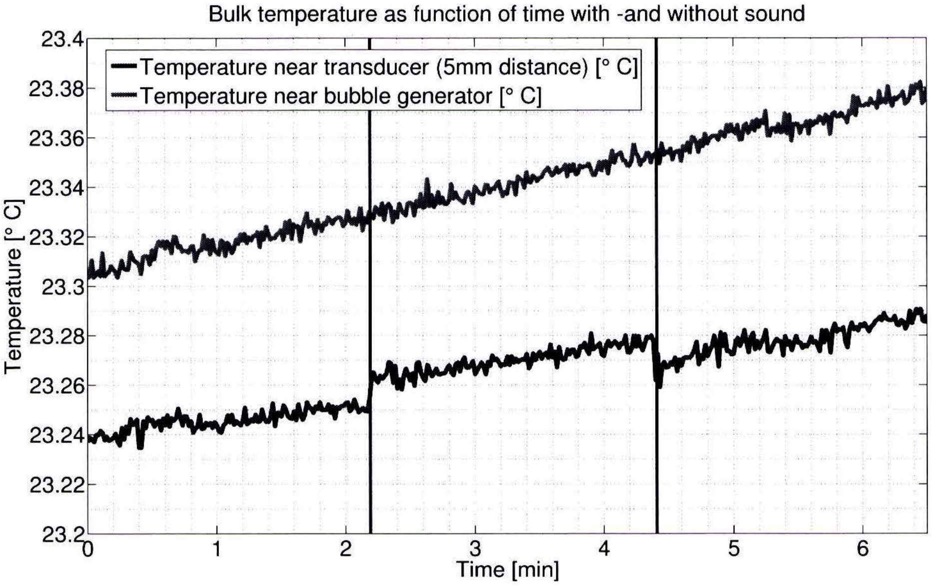

Figure 4.7: Bulk temperature at $T_{\text{bulk}} \approx 23.3°$Celsius. Between the black vertical lines the sound was turned on. It can be observed that a small increase in temperature occurs when the speaker is turned on at 5 millimeters in front of the speaker.

the coil inside the speaker) and not of the acoustic waves. An increase in temperature due to attenuation of the acoustic wave would result in a linear increase and therefore a steeper slope. The temperature measured near the bubble generator does not show any change in temperature. Since the slope of the curve stays the same during the excitation, it can be concluded that no heat is added by the sonic waves at the position of the bubble generator.

Additional generated heat

Based on the maximum temperature increase of 0.02° Celsius at a distance of five millimeters in front of the speaker, we can estimate the additional generated heat of the speaker using the following expression:

$$Q_{\text{sound}} = m_l \cdot c_{p_l} \cdot \Delta T \tag{4.8}$$

with m_l the mass of the liquid [kg], c_{p_l} the specific heat of the liquid [J/(kg · K)] and ΔT the measured temperature difference.

All additional heat is transferred into the horizontal cylinder of the setup (see figure 4.2), where the diameter of the cylinder is equal to the diameter of the speaker (Ø 80mm). The additional heat is thus able to heat up a volume of

$$V_l = 0.005 \cdot \frac{\pi}{4} 0.08^2 = 2.5 \cdot 10^{-5} \quad \text{m}^3$$

with an amount of 0.02° Celsius. Introduction of $m_l = \rho_l \cdot V_l$ into equation 4.8 results in:

$$Q_{\text{sound}} = 998.4 \cdot 2.5 \cdot 10^{-5} \cdot 4216 \cdot 0.02 = 2.1 \quad [\text{W}] \tag{4.9}$$

The bubbles are generated at a distance of approximately 15 centimeter away of the speaker. A liquid volume of $V_l = 7.5 \cdot 10^{-4}$ m^3 is therefore located between the speaker surface and the bubble generator. The maximum increase in temperature at the position of the bubble generator can now easily be obtained by application of

$$\Delta T = \frac{Q_{\text{sound}}}{(\rho_l \cdot V_l \cdot c_{p_l})} \tag{4.10}$$

and results in $\Delta T = 6.6 \cdot 10^{-4\circ}$ Celsius.

Based on figure 4.7 and the presented calculations, we conclude that Q_{sound} (the heat generation of the speaker and the attenuation of the sonic waves) has no influence near the location of the bubble generator and we neglect Q_{sound} in the (local) energy equation of our pool boiling setup. Therefore we can write:

$$\boxed{Q_{\text{sound}} \approx 0 \quad [\text{W}]} \tag{4.11}$$

4.6.4 Losses to the surroundings

The heat flux that is lost to the surroundings Q_{losses} has to be included in the energy equation. To minimize the losses to the surroundings we covered the extended reservoir by thick isolation material, whereas the pool boiling pot is kept at bulk temperature by the silicon heating pads. An estimation of the losses to the surroundings can be made based on figure C.1. If the heating pads are disabled, the bulk decreases approximately three tenths of a degree in three minutes.

Since the experiments are performed in less than ten seconds we presume that no heat transfer to the surroundings will occur. Furthermore, we compare the situation with -and without acoustic excitation and it is very likely that heat losses were the same during the experiment. We can write for the heat losses:

$$\boxed{Q_{\text{losses}} \approx 0 \quad [\text{W}]} \tag{4.12}$$

4.6.5 Total heat transfer

The total energy equation of our setup can now easily be constructed. During the measurements, the silicon heating elements were turned off. The bubble generator is therefore the only heating element which generates the power for boiling. The power input is referred to as Q_{power}. The power delivered by the bubble generator is either transported by the generated bubbles or transferred to the fluid by convection.

The energy equation of the experimental setup is given by:

$$\boxed{Q_{\text{power}} + Q_{\text{sound}} = Q_{\text{bubbles}} + Q_{\text{convection}} + Q_{\text{losses}} \quad [\text{W}]} \tag{4.13}$$

Here we used $Q = q'' \cdot A$.

The energy equation can be rewritten using equations 4.6 up to 4.12 into the following form:

$$\boxed{Q_{\text{power}} = \rho_v \cdot V_{\text{bubbles}} \cdot h_{ev} \cdot f \cdot N_a + h \cdot A \cdot (T_{\text{wall}} - T_{\text{bulk}}) \quad [\text{W}]} \qquad (4.14)$$

where A is the surface of the heated thin film [m^2] and $N_a = N_a'' \cdot A$ the number of active nucleation sites [#].

In the next chapter we present the results of acoustic excitation on bubble volume, bubble growth and waiting time. In chapter 6 we investigate the influence of the reported results on the heat transfer.

Chapter 5

Results

The results of the performed pool boiling measurements are presented in this chapter. We start with a discussion of the results obtained from the stainless steel bubble generators. The effects of sound on bubble volume, bubble growth times and waiting times are presented for excitation in the Rayleigh-Plesset volumetric mode as well as for the first order 'Lamb'-mode. Furthermore, we show the effects of frequency on bubble detachment.

5.1 Resonance modes

For the experiments with acoustic excitation in the volumetric Rayleigh-Plesset mode, we used two types of stainless steel bubble generators. The first type, in the following denoted with SSBG1, is equipped with an internal thermocouple and has a cavity radius of 30μm. The second type, denoted with SSBG2, has no internal thermocouple and the cavity radius equals 20μm. Experiments performed with both types are treated separately in the following sections. The experiments with acoustic excitation in the first order Lamb mode are performed with the SSBG1.

5.2 Volumetric resonance mode using SSBG1

This section presents the effects of acoustic excitation in the isotropic mode of the bubbles generated by the stainless steel bubble generator SSBG1.

5.2.1 Measurement configuration

During all performed measurements, the bubbles were recorded with a frame rate of 3000 frames per second, which was the maximum possible frame rate for a sufficient high resolution of 512 x 256 pixels and the available amount of light. The applied power was maintained at a value of $Q_{\text{power}} = 7.4$ [W], whereas the temperature of the bulk was slightly varied per measurement. The wall temperature of the bubble generator is calculated using relation 4.3 obtained by the calibration measurements. The pixel to millimeter ratio is calibrated as:

$$\frac{\text{pixels}}{\text{millimeter}} = \frac{222 \pm \Delta 2}{3.10 \pm \Delta 0.01}$$

resulting in the size of one pixel equal to 0.0140± 0.0001 millimeters (see section 4.5).

5.2.2 Effect of sound on bubble volume

The effect of acoustic excitation is investigated by comparing the volumes at detachment of the bubbles before the trigger (no excitation) and after the trigger (excitation in isotropic resonance frequency). Before the sound wave is applied, constant "bubble-trains" are generated: all bubbles have exactly the same volume, same growth time and the waiting times are constant. For the best comparison between the different experiments, we tried to generate bubbles of the same volume each experiment. However, we found out that it is extremely difficult to generate vapor bubbles with exactly the same volume in different experiments, especially when the experiments are performed on different days. A small increase in pressure, bulk temperature or water quality can influence the bubble size. Nonetheless we were able to generate bubbles of almost equal volume.

Figure 5.1(a) shows the volume in mm^3 of the recorded bubbles as function of time before and after the trigger with sound. Four different measurements are presented here, were the frequencies of the applied acoustic waves per measurement are given in the legend. The wave generator and the high speed camera are triggered at time $t = 0$, which is indicated by the thick vertical black line in the figure. The sound setup (wave generator → amplifier → speaker) has a time delay due to start-up effects of approximately 0.15 seconds, indicated by the dashed vertical black line. The error bars denote the maximum possible error of 3% as a result of the estimation of the bubble width and height by hand (see for a more thorough error analysis section 4.5). For clarity we presented only a few error bars, but of course all bubbles have the same error and corresponding bar.

The bubble volumes at detachment are estimated with use of expression 4.2 and the bubble radii of the different measurements are found to be in the order of 1.05 ± 0.05 millimeters. Recalling equation 2.13 of Chesters [23] for the approximation of the maximum bubble radius at detachment, results - with a cavity size of 30 μm - in:

$$R_{\max}^3 = \frac{3 r_{cav} \sigma}{2 \rho_l g} \approx 0.66 \quad [\mathrm{mm}] \tag{5.1}$$

The radii of the generated bubbles are almost 40% larger than the predicted theoretical radius $R_{\max}$. The resonance frequencies of the generated bubbles are therefore smaller than the predicted 4000 Hz, however the expression is a good first estimate of the order of the resonance frequencies.

It can be observed from figure 5.1(a) that in three of the four measurements, the bubble volume decreases immediately after the acoustic waves are applied. The bubbles which are excited by acoustic waves with a frequency of 2800 Hz show no effect on the sound. These bubbles are the largest in volume of all measurements and they have the lowest resonance frequency. Instead, we excited the largest bubbles with the highest frequency of all measurements. The frequency of the applied waves seems to be related to bubble size.

To investigate whether the decrease in bubble volume is correlated to the resonance frequencies of the bubble we recall equation 2.27 and 2.40:

$$\omega_{RP_{\text{wall}}} = \frac{\omega_{RP}}{1.1971} \qquad \text{where} \qquad \omega_{RP} = \sqrt{\frac{3\gamma p_\infty}{\rho_l R_{t=0}^2} + \frac{2(3\gamma - 1)\sigma}{\rho_l R_{t=0}^3}} \tag{5.2}$$

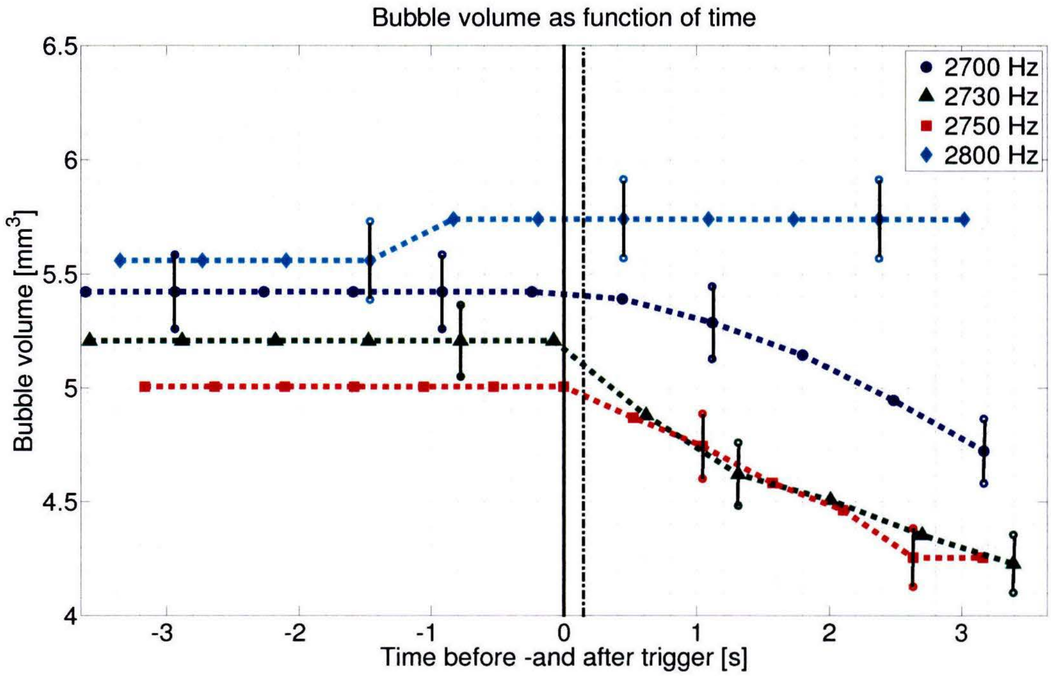

(a) Bubble volume as function of time before and after trigger. The vertical lines are the error bars, where the maximum error is 3%. The symbols indicate the volumes of the vapor bubbles at detachment.

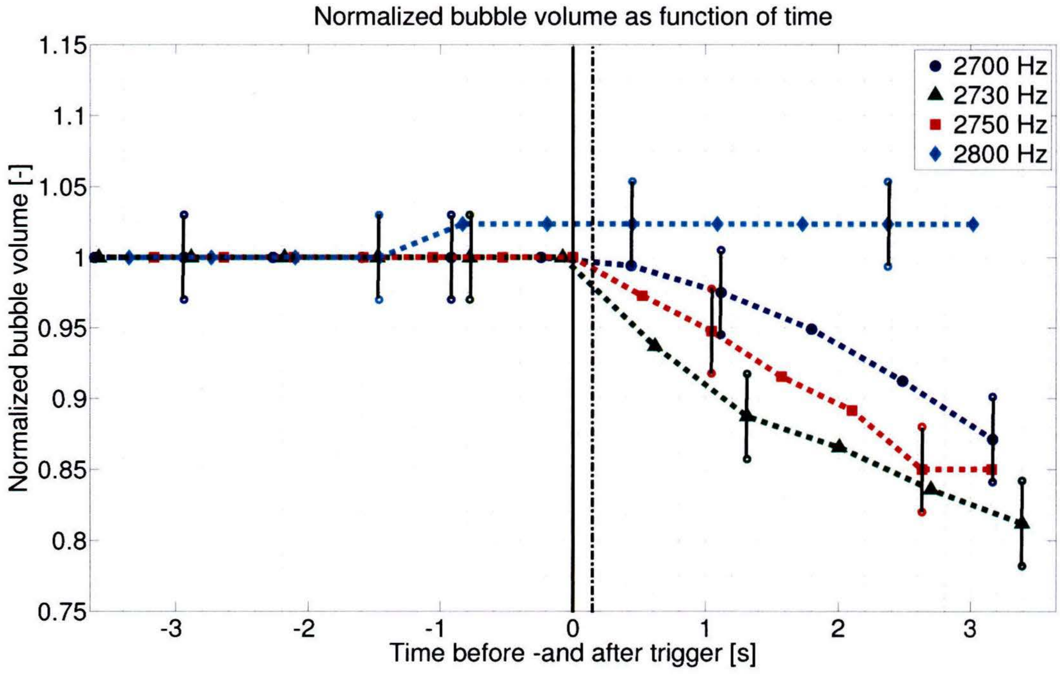

(b) Normalized bubble volume as function of time before and after trigger. The vertical lines are the error bars, where the maximum error is 3%. The symbols indicate the volumes of the vapor bubbles at detachment.

Figure 5.1: Bubble volume as function of time before and after trigger. The black solid vertical line at $t = 0$ corresponds to the trigger of the camera and the wave-generator, whereas the black dotted vertical line at $t \approx 0.15$ corresponds to the time delay of the sound setup.

The values for saturated water can be found in table 2.1. The radius at detachment of the bubble right before the trigger determines which frequency should be applied to excite the bubbles in their resonance frequencies. Therefore, these bubble radii are given in table 5.1 together with the corresponding theoretical predicted resonance frequency $\nu_{RP_{wall}}$. The frequency dependence is investigated by comparing the differences between applied frequency and theoretical predicted frequency. The difference, $\Delta\nu$, is presented in column five of table 5.1.

From the fifth column of table 5.1 we can conclude that the difference between applied frequency and theoretical predicted frequency in measurement number 4 (2800 Hz) is relatively large as compared to the other three measurements, where a decrease in bubble volume is observed. To make an estimate of the decrease in bubble volume as function of frequency difference, we normalized the bubble volumes in figure 5.1(b). The volumes are normalized with respect to the volume of the first bubble.

It follows that the smaller the difference $\Delta\nu$, the larger the decrease in bubble volume. The absolute frequency difference $|\Delta\nu|$ is almost equal for measurement number 1 and 3, which results in a comparable decrease in bubble volume as function of time.

In contrast, the bubble volume in measurement number 4 increases. The increase however, occurs before the sound was triggered and the increase in bubble volume is located between the error bars of 3%. The increase can therefore not be larger than one single pixel in height and one single pixel in width. The small increase in bubble volume is probably an effect of an error in the pixel determination, the restricted resolution of the recordings or a small increase in superheat (this will be investigated in section 5.2.5).

Figure 5.2 shows the maximum decrease in bubble volume as function of the difference in frequency $\Delta\nu$. The black lines are the error bars. The 'v-shaped' plot proves that the decrease in bubble volume is resonance dependent (recall the resonance response of the weakly-damped oscillator as discussed in section 2.2, where the maximum response occurred at ω_F/ω_0). The largest decrease in bubble volume can be obtained by acoustic waves with frequencies equal to - or close to - the resonance frequency of the growing vapor bubble.

#	ν_{applied}[Hz]	$R_{bubble}[mm]$	$\nu_{RP_{wall}}$[Hz]	$\Delta\nu = \nu_{\text{applied}} - \nu_{RP_{wall}}$ [-]	Volume decrease [%]
1	2700	1.047 ± 0.014	2677 ± 36	23 ± 36	12.9 ± 3
2	2730	1.026 ± 0.014	2732 ± 38	-2 ± 38	18.8 ± 3
3	2750	1.012 ± 0.014	2770 ± 39	-20 ± 39	15.0 ± 3
4	2800	1.068 ± 0.014	2624 ± 35	176 ± 55	0.0 ± 3

Table 5.1: Frequency dependence of bubbles in the four different measurements. The table shows the numbers corresponding to the different measurements in the first column, the applied frequency of sonic wave in the second column, bubble radius right before trigger in the third column, theoretical predicted value of volumetric resonance mode at wall in the fourth column and difference between applied frequency and theoretical resonance frequency in the fifth column. The last column shows the decrease in percentage bubble volume. The errors in the table are the maximum possible errors made in the determination of the bubble size (1 pixel error (1.4 %) in determination of bubble radius and 3% in bubble volume).

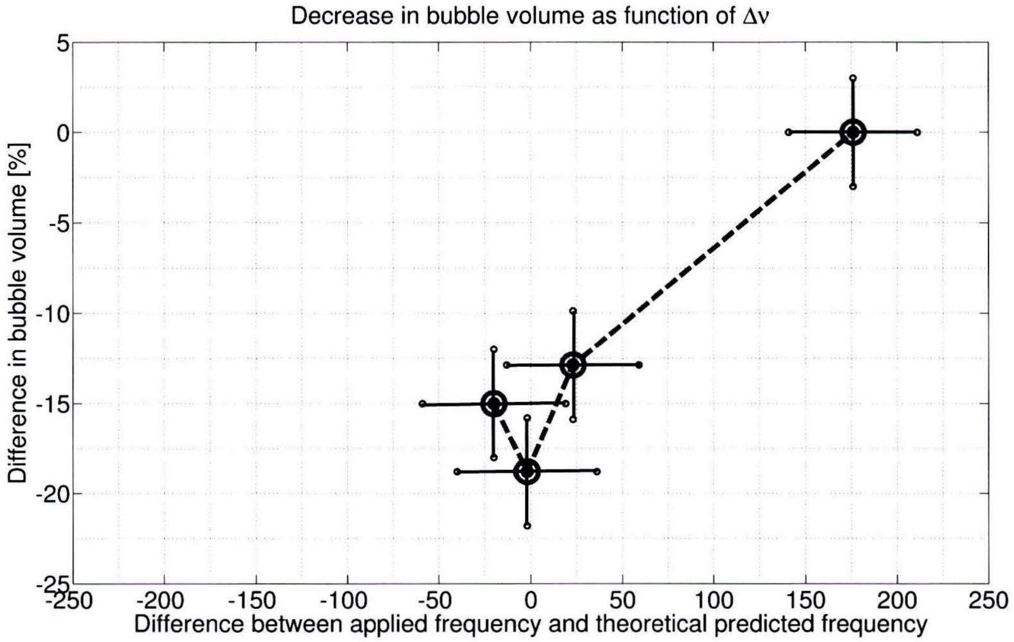

Figure 5.2: Decrease in bubble volume as function of the difference in frequency $\Delta\nu$. The black lines are the error bars, with a maximum error of ± 39 Hz in horizontal direction and ± 3% in vertical direction. The horizontal error is a result of the error of one pixel (1 %) in the determination of the radius.

5.2.3 Effect of sound on bubble growth times

The effect of acoustic excitation on the bubble growth time is shown in this subsection. From the previous subsection it was concluded that sound can decrease the volume of the growing vapor bubbles as long as the acoustic waves have frequencies close to the resonance frequencies of the bubbles (see figure 5.2). Smaller bubbles should result in smaller growth times, which means - if the waiting times are not increased - an increase in the bubble departure frequency, thereby promoting micro-convection.

The growth times of the recorded bubbles as function of time before and after the trigger are shown in figure 5.3. Again we normalized the growth times to compare the different measurements with each other. It can be observed that the growth times are very constant before the sound wave is applied. After the trigger, the growth times decrease slowly for measurement number 1 and 3, and immediately for the measurement where the frequency difference is the smallest. The growth times of the bubbles in measurement number 4 are not changed at all and again the conclusion can be drawn that the applied sound has no influence on these bubbles.

The error made in the determination of the bubble growth time is one frame. Since the bubbles grow in approximately 28 frames (corresponding to a growth time of $28/3 = 9\frac{1}{3}$ms), the error is relatively large and equal to $\frac{1}{28} = 3.6\%$. We are pretty sure that the decrease in bubble growth time is a consequence of the sound, especially since the frequency dependence can be observed. However, the decrease in growth time of the bubbles is equal to the maximum possible error. It can therefore not completely be excluded that the decrease in growth time might be a measurement error.

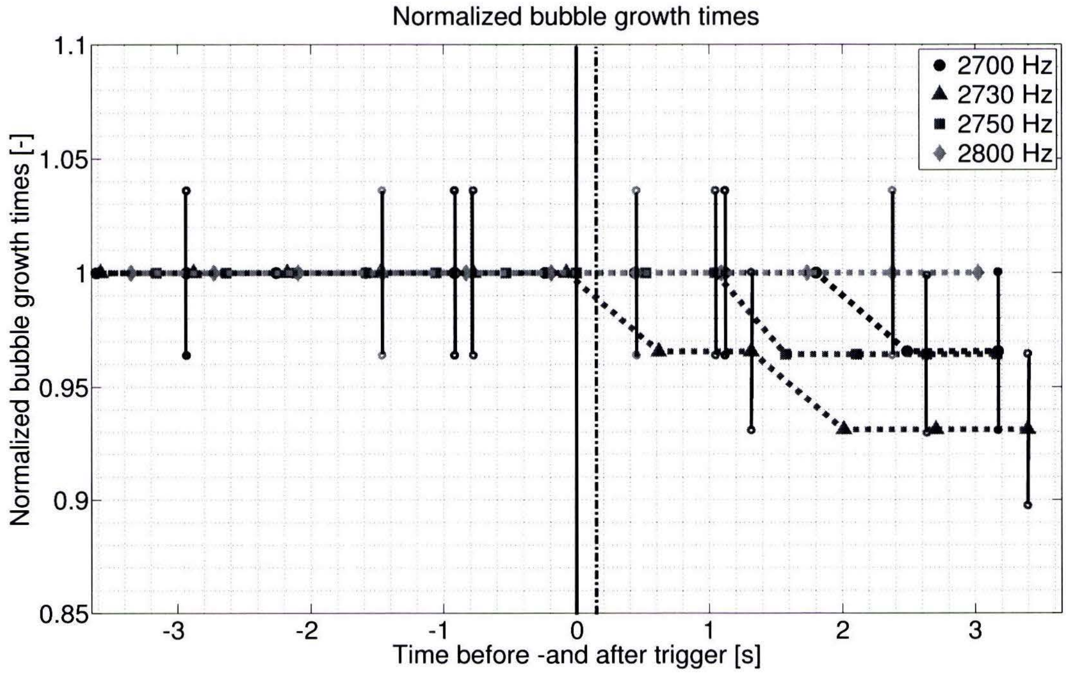

Figure 5.3: Bubble growth times as function of time before and after the trigger. The error bars correspond to the error of one frame equal to 3.6%.

5.2.4 Effect of sound on waiting time

The waiting time is the time between two adjacent bubbles. The waiting times are visualized in figure 5.4. It can be observed that the time between two adjacent vapor bubbles is much shorter for measurement number 3 than it is for the other measurements (the waiting time is in the order of 0.5 seconds versus 0.65 seconds), which means that the departure frequency of the bubbles was higher. The vertical black lines indicate the trigger of the sound and the camera.

The figure shows that there is almost no difference in the waiting time before -and after the triggering. For each measurements the waiting time has a constant value and no effect of acoustic excitation can be observed. Therefore we conclude that acoustic excitation has no effect on the waiting time between two adjacent bubbles.

5.2.5 Temperature registration

To make sure that the decrease in bubble volume during the measurements is not a result of a change in temperature, we logged the temperatures of both the bulk and the thin sheet film. The difference between these temperatures, ΔT, is the driving force of bubble growth. The temperature of the bulk, the temperature of the heater and the superheat before and after the trigger are presented in figure 5.5 for measurement number 2. Temperature registrations of the other experiments can be found in appendix D. During the experiments we switched off the heating elements, preventing heating up of the bulk.

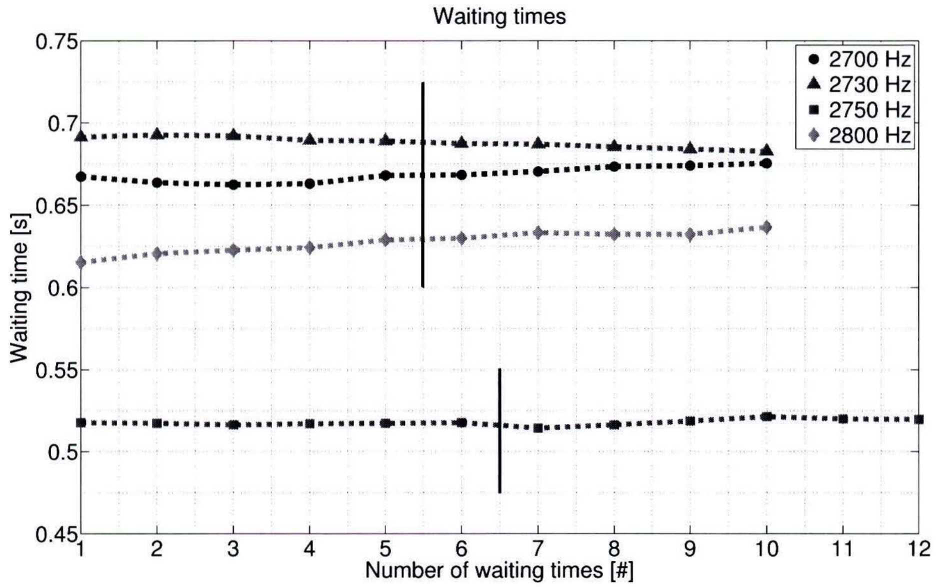

Figure 5.4: Waiting times as function of total number of waiting times during the recordings. The symbols correspond to the waiting time between two adjacent bubbles [s].

Since the internal thermocouple is mounted inside the steel holder at a distance of 200μm underneath the thin sheet film, the measured temperature has a delay of several seconds [78]. Therefore we present the temperature in figure 5.5 up to eight seconds after the trigger, which should be long enough to observe changes in the heater wall.

Figure 5.5 proves that during the recordings of the bubbles, almost no changes in ΔT occurred and that the decrease in bubble volume should be an effect of the pressure waves inside the pool boiling pot. The influence of temperature on the change in bubble volume during the measurement can be excluded. The same conclusion holds for the other experiments where a decrease in bubble volume was observed.

To investigate whether the increase in bubble volume of the bubbles of measurement number 4 is a consequence of a change in the superheat ΔT we plotted the registration of the superheat in figure D.1 in appendix D. It can be observed that a small increase in superheat occurs and this is probably the effect of the small increase in bubble volume during the measurement.

The effect of the decrease in bubble volume and the constant ΔT on the heat transfer will be discussed in the next chapter.

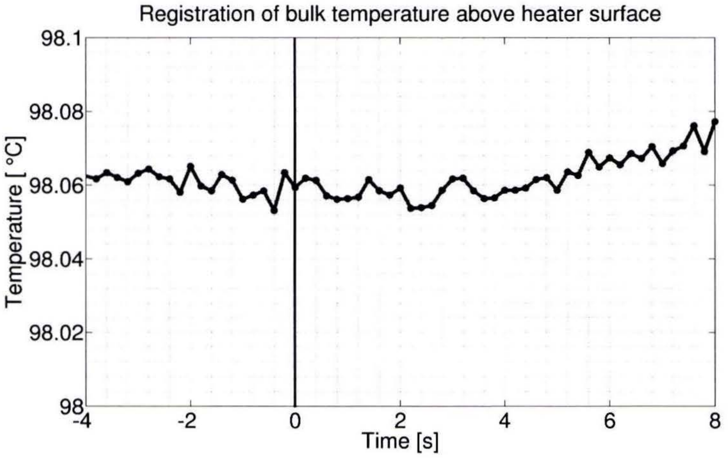

(a) Temperature registration of the bulk in the center of the pool boiling pot.

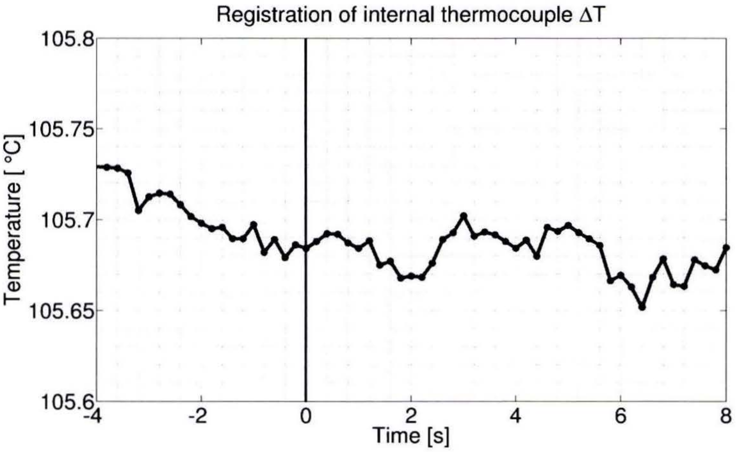

(b) Temperature registration of internal thermocouple. The thermocouple is located inside the steel holder and has therefore a delay of several seconds [78].

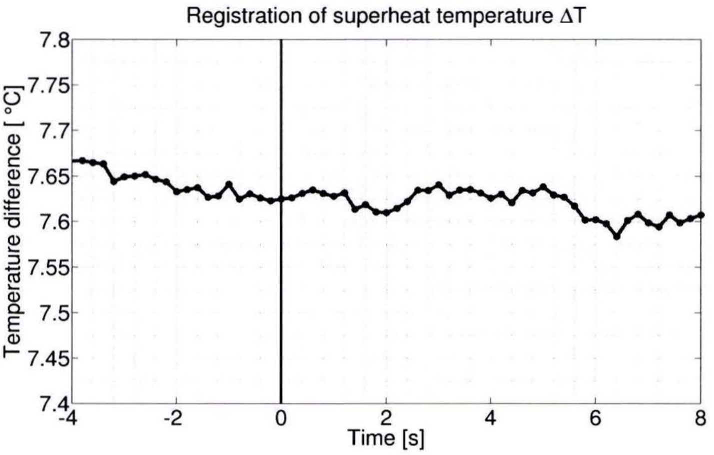

(c) Registration of superheat temperature Δ T.

Figure 5.5: Temperature registration before and after the trigger of sound corresponding to measurement number 2.

5.2.6 Bubble growth with -and without sound

We analyzed the bubble growth of the bubbles in experiment number 2 with each other. The bubble diameter and bubble height as function of growth time of the undisturbed bubbles is compared to the diameter and bubble height as function of growth time of the disturbed bubbles.

The bubble growth of the undisturbed bubbles as function of growth time is very reproducible. At each instant of time the bubbles have the same bubble radius and bubble height. The reproducibility of the bubble growth of the excited bubbles however is much worse, since the decrease in volume of the excited bubbles increases with time. We therefore only compare the bubble growth of the excited bubble with the largest volume decrease - corresponding to bubble number 11 in measurement #2 - with the undisturbed bubble growth in the figures 5.6 and 5.7.

The bubble diameter as function of growth time is compared in figure 5.6. The maximum possible error in the determination of the bubble diameter is 2 pixels, which corresponds to an error of approximately 1.4%. No error bars are shown in the figure, but it can clearly be observed that the bubble growth of the disturbed bubble (bubble number 11) is outside this error range of 1.4%. The figure shows that the growth of the diameter of bubble number 11 starts to deviate from the undisturbed bubbles at approximately 3 milliseconds. At detachment, the disturbed bubble detaches 0.7 milliseconds faster and the bubble diameter has decreased with 7 % as indicated in the figure.

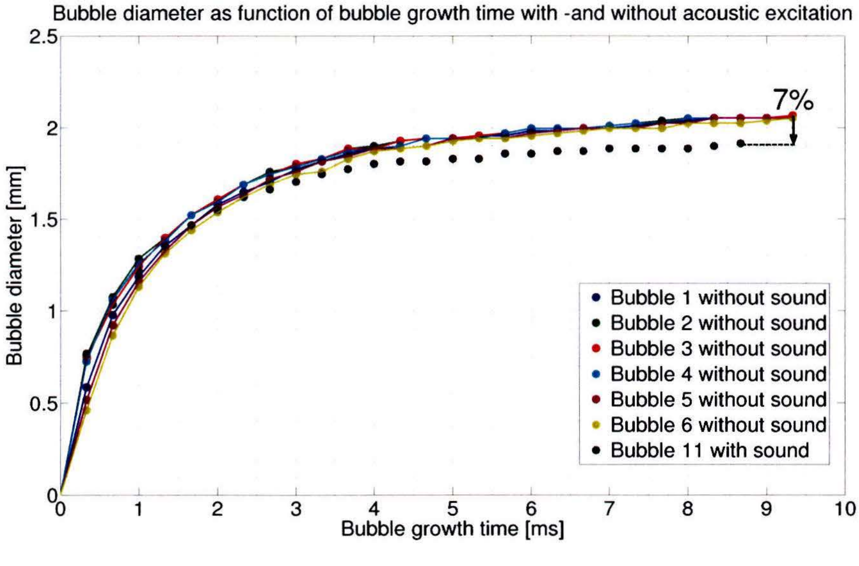

Figure 5.6: Bubble growth of the diameter of the undisturbed bubbles compared to the growth of the diameter of the disturbed bubble with the largest decrease in volume (bubble number 11 in experiment # 2). The bubble detaches 0.7 milliseconds faster and the bubble diameter has decreased with 7 %.

The bubble height as function of growth time with and without sound is compared in figure 5.7. The bubble height as function of time can perfectly be described by the theoretical predicted diffusion controlled bubble growth as given in equation 2.7. The theoretical prediction is shown in the figure by the black dashed line. To calculate the theoretical predicted growth we used the values for water as presented in table 2.1. The temperature of the heater wall and bulk are based on the values of figure 5.5, which leads to $T_{\text{bulk}} = 98.1°\text{C}$ and $T_{\text{wall}} = 106°\text{C}$. The corresponding Jacob number is equal to Ja = 23.6 and we fitted the shape function C_s to the value of 1.1

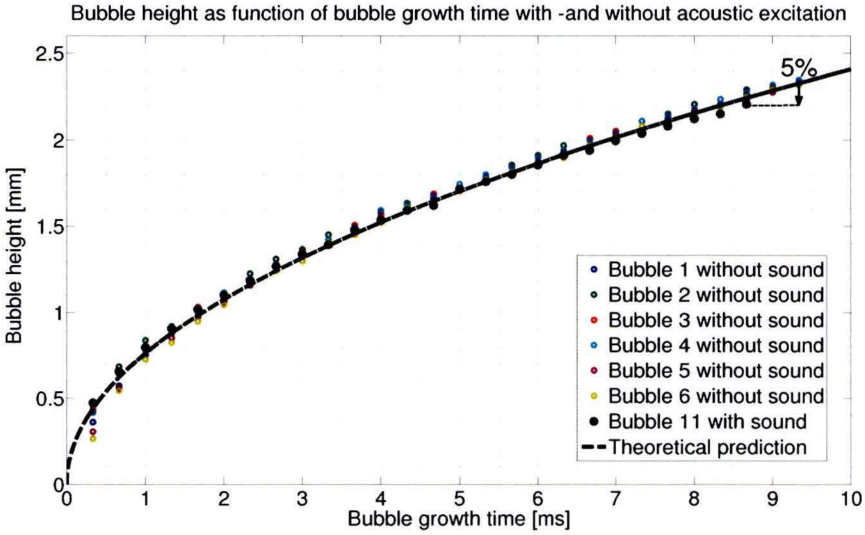

Figure 5.7: Growth of bubble height of the undisturbed bubbles compared to the bubble height of the disturbed bubble with the largest decrease in volume (bubble number 11 in experiment # 2). The black dotted line corresponds to the theoretical predicted diffusion controlled bubble growth (equation 2.7), where $\Delta T = 7.9$ [$°C$], Ja = 23.6 [-] and $\alpha = \lambda/(\rho_l c_{p_l}) = 1.68 \cdot 10^{-7}$ [m^2/s]. The shape correction factor C_s is fitted to the value of 1.1.

The bubble height as function of growth time for the disturbed bubble is almost comparable to the bubble height of the undisturbed bubbles in time. The height of the disturbed bubble is approximately 2 % smaller during the last stage of the growth. Since the bubble detaches 0.7 milliseconds faster, a total decrease of 5 % in bubble height is obtained in the end.

Bubble recordings

The figures 5.8 and 5.9 show recorded images of the bubble growth for the case of an undisturbed bubble at the left and a bubble disturbed by acoustic waves with frequency 2730 Hz at the right. The horizontal bar corresponds to the bubble diameter of the undisturbed bubbles at detachment and has a length of 150 pixels. With the corresponding conversion factor this yields to a length of 2.09 millimeter.

The data shown in figure 5.6 and 5.7 are based on the presented recordings. The decrease in bubble volume and the decrease in bubble growth time are nicely visualized in this way. Moreover, it can be observed that the bubbles grow via growth mode A as was discussed in section 2.1.5. The results will be analyzed more thoroughly in the next chapter, were the induced pressure field of the sound source is taken into account as well.

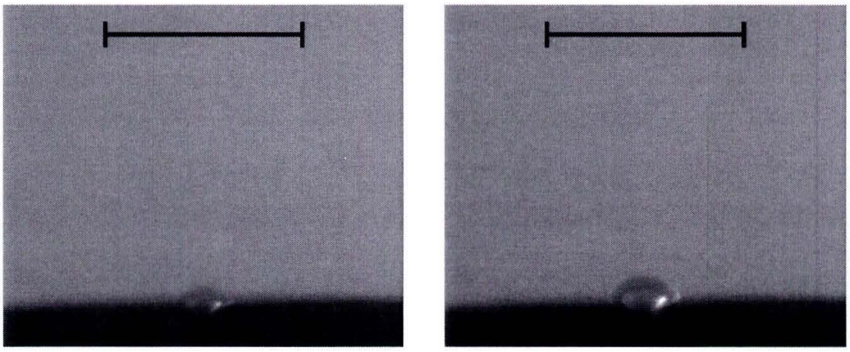

(a) t = 0.33 ms (b) t = 0.33 ms

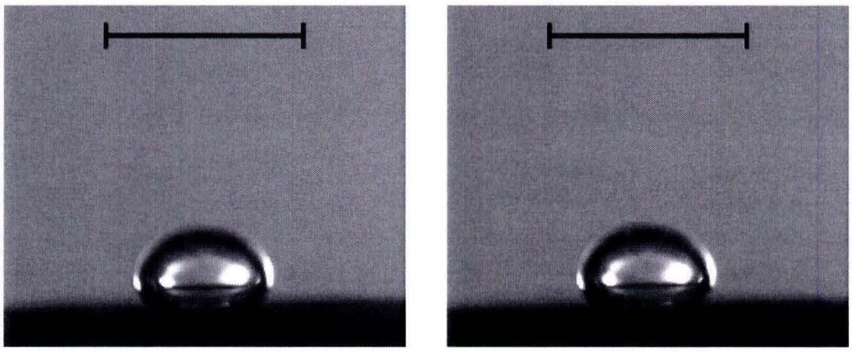

(c) t = 1.67 ms (d) t = 1.67 ms

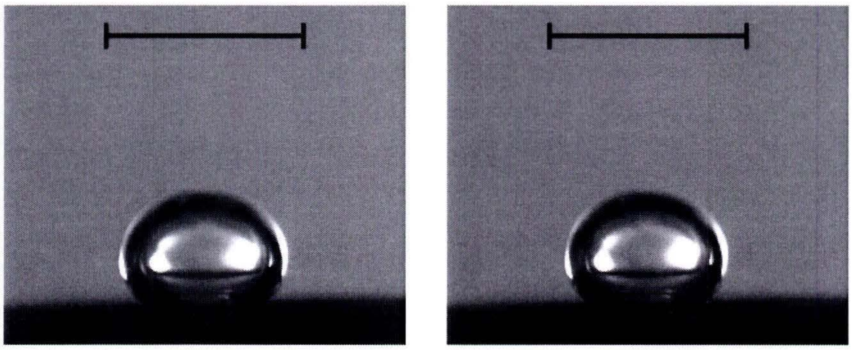

(e) t = 3.00 ms (f) t = 3.00 ms

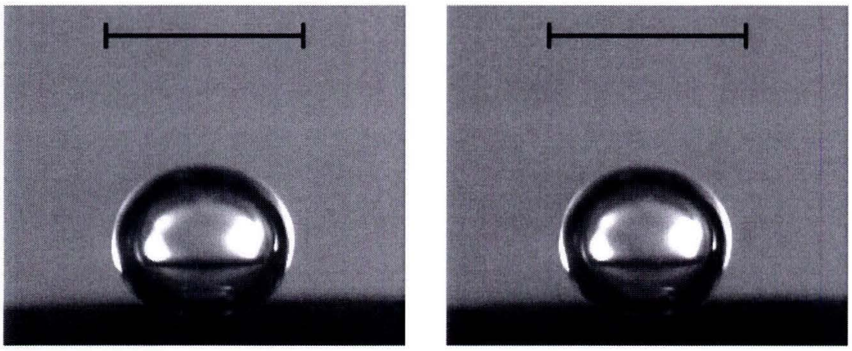

(g) t = 4.33 ms (h) t = 4.33 ms

Figure 5.8: Bubble growth of bubble without acoustic excitation (left) and with acoustic excitation 2730 Hz (right). The horizontal bar corresponds to 150 pixels (2.09 millimeter), equal to the detachment diameter of the bubble without acoustic excitation.

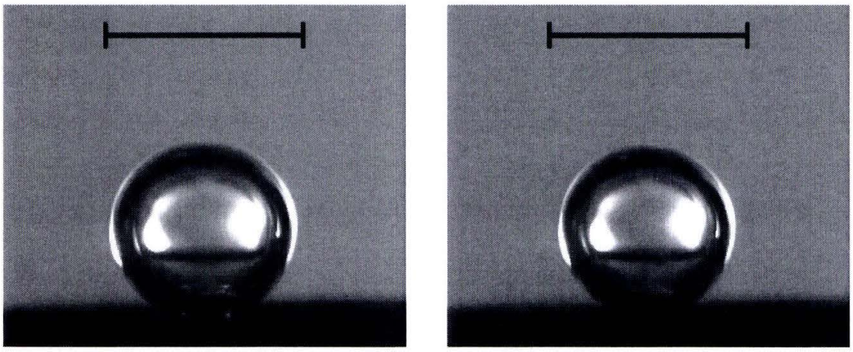

(a) t = 5.67 ms (b) t = 5.67 ms

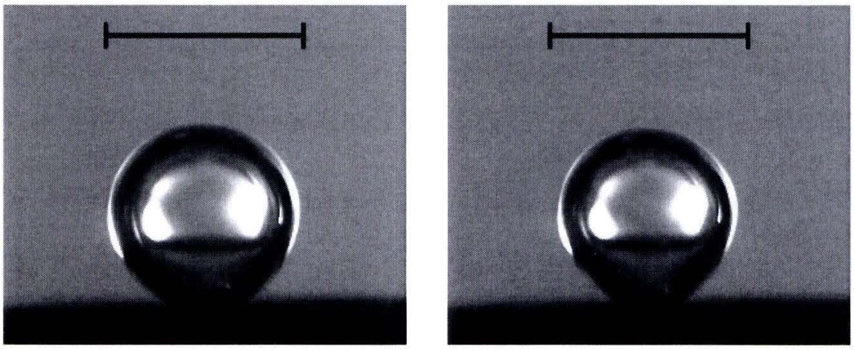

(c) t = 7.00 ms (d) t = 7.00 ms

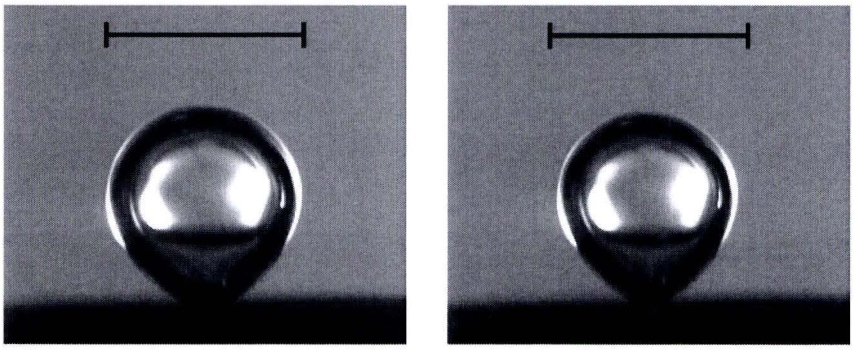

(e) t = 8.33 ms (f) t = 8.33 ms

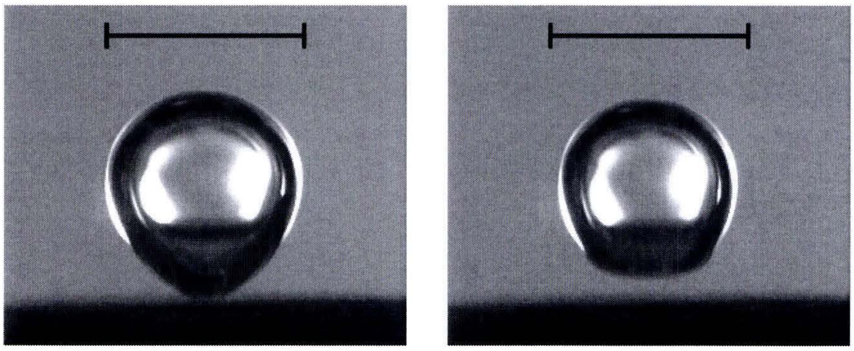

(g) t = 9.67 ms (h) t = 9.67 ms

Figure 5.9: Bubble growth (continued) of bubble without acoustic excitation (left) and with acoustic excitation of 2730 Hz (right). The horizontal bar corresponds to 150 pixels (2.09 millimeter), equal to the detachment diameter of the bubble without acoustic excitation.

5.3 Volumetric resonance mode using SSBG2

Experiments with acoustic excitation in the volumetric mode using the SSBG2 are presented in this section. The SSBG2 has a smaller cavity radius (20μm) and no internal thermocouple. The temperature of the thin steel sheet is measured by a PT-100 sensor located on top of the bubble generator. The reason to use two different types of stainless steel bubble generators was the fact that the glue of the SSBG1 showed some leakage after intensive use and multiple active nucleation sites were visible.

The advantage of using two different types of generators is the difference in vapor bubble conditions. The generated bubbles of the SSBG2 are much smaller and the bubble departure frequencies are higher than in the previous case. It is of interest to investigate if the same conclusions hold for the case of small bubbles. An important drawback of the recordings with small bubbles is the relative large error in the determination of the bubble size in pixels and in the determination of the growth times.

5.3.1 Measurement configuration

During all measurements with the SSBG2, the temperature difference ΔT was determined by the use of two PT-100 sensors. One located on top of the thin steel sheet, the other located in the bulk. The high speed recordings were recorded at a frame rate of 3000 frames per second and with a resolution of 512 x 256 pixels. The applied power during all measurements was equal to $Q_{\text{power}} = 7.8$ [W], whereas the temperature of the bulk was slightly varied per measurement. For each measurement the pixel to millimeter ratio is calibrated as

$$\frac{\text{pixels}}{\text{millimeter}} = \frac{228 \pm \Delta 2}{3.10 \pm \Delta 0.01}$$

resulting in the size of one pixel equal to 0.0136± 0.0001 millimeters.

5.3.2 Effect of sound on bubble volume

The bubble volumes in mm^3 as function of time before and after the trigger are shown in figure 5.10. Five different measurements are presented in the figure for clarity. Three other experiments with large $\Delta\nu$ were performed as well, however the applied acoustic waves showed no effect on bubble decrease and are therefore not presented here. The data of these three measurements can be found in appendix E.

As follows from figure 5.10, the bubbles generated by the SSBG2 are much smaller than the bubbles generated by the SSBG1 (bubble volumes almost 3 times as small). It was therefore even harder to generate equally sized bubbles per experiment. Moreover, much more bubbles are generated per unit of time with the SSBG2 than with the SSBG1 under almost the same conditions.

The generated bubbles have all radii of 0.65 ± 0.06 millimeter. The approximation of $R_{\max}$ using equation 2.13 of Chesters [23] is for a cavity size of 20 μm equal to 0.57 millimeter. The error in the approximation is only 11 % in this case.

The frequencies of the applied acoustic waves per experiment are given in the legend. Since the generated vapor bubbles are smaller, higher frequencies (in the order of 4000Hz) are applied. The horizontal dashed lines in figure 5.10 correspond to an error of 3% as a result of the estimation of the bubble width and height by hand. However, based on the figure it seems that we might have overestimated the error. We introduced error bars in the figure corresponding to 2 % which cover all fluctuations in bubble volume.

Figure 5.10(b) shows the normalized bubble volumes before and after the trigger. We normalized with respect to the volume of the first bubble. Once more it can be observed that for some measurements the bubble volume decreased, whereas in other measurements the volume did almost not change. We start the analysis by comparing the difference between applied frequency and the theoretical predicted frequency based on the radii of the bubbles before the trigger. The theoretical volumetric frequency is calculated with use of Equation 5.2. The results are given in table 5.2.

The bubble volumes of measurement numbers 4, 5 and 6 decrease after the trigger with sound. The change in volume of the bubbles in the other measurements is small and the percentage volume change is located between the error bars. The sudden change in bubble volume for these experiments is possibly an effect of small temperature changes, error in the determination of bubble size by hand or the restricted resolution.

Due to the small bubbles we have relative large errors in the determination of bubble size. This leads to uncertainties of 2 % in the bubble radius, resulting in errors of 2 % with respect to theoretical predicted frequencies as well. Therefore, the uncertainties in frequency in the fourth and fifth column are in the order of 100 Hz.

#	ν_{applied}[Hz]	$R_{bubble}[mm]$	$\nu_{RP_{wall}}$[Hz]	$\Delta\nu = \nu_{\text{applied}} - \nu_{RP_{wall}}$ [-]	Volume decrease [%]
1	3200	0.6390 ± 0.0136	4388 ± 95	-1188 ± 95	-3.10 ± 5
2	3800	0.6798 ± 0.0136	4124 ± 84	-324 ± 84	-0.89 ± 5
3	4000	0.6594 ± 0.0136	4252 ± 89	-252 ± 89	-2.86 ± 5
4	4050	0.7138 ± 0.0136	3927 ± 77	123 ± 77	3.60 ± 5
5	4150	0.6798 ± 0.0136	4124 ± 84	26 ± 84	9.36 ± 5
6	4200	0.6526 ± 0.0136	4296 ± 92	-96 ± 92	3.94 ± 5
7	4400	0.6594 ± 0.0136	4252 ± 89	148 ± 89	1.87 ± 5
8	5000	0.6186 ± 0.0136	4532 ± 102	468 ± 102	-0.98 ± 5

Table 5.2: Frequency dependence of bubbles in eight different measurements. The table shows the numbers corresponding to the different measurements in the first column, the applied frequency of sonic wave in the second column, bubble radius right before trigger in the third column, theoretical predicted value of volumetric resonance mode at wall in the fourth column and difference between applied frequency and theoretical resonance frequency in the fifth column. The last column shows the decrease in percentage bubble volume. The errors in the table are the maximum possible errors made in the determination of the bubble size (1 pixel error (2%) in determination of bubble radius and 5% in bubble volume).

Figure 5.11 shows the maximum decrease in bubble volume as function of the difference in frequency $\Delta\nu$. The black lines are the error bars. The figure shows the same 'v-shaped' behavior, corresponding to the forced weakly damped oscillator resonance peak (as discussed

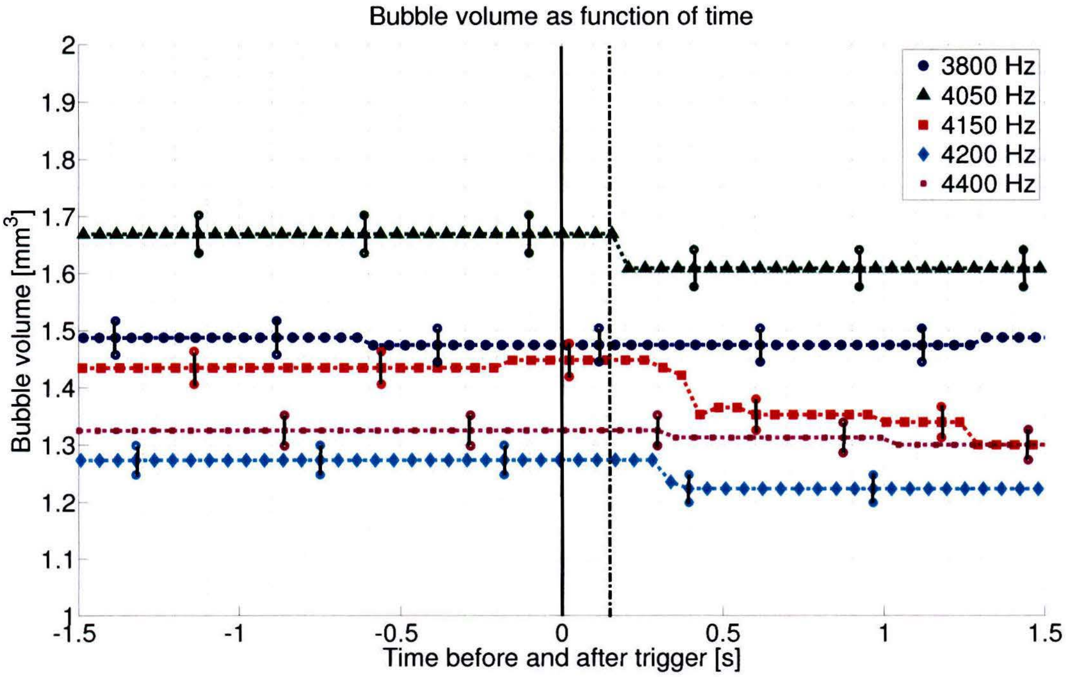

(a) Bubble volume as function of time before and after trigger. The symbols indicate the volumes of the vapor bubbles.

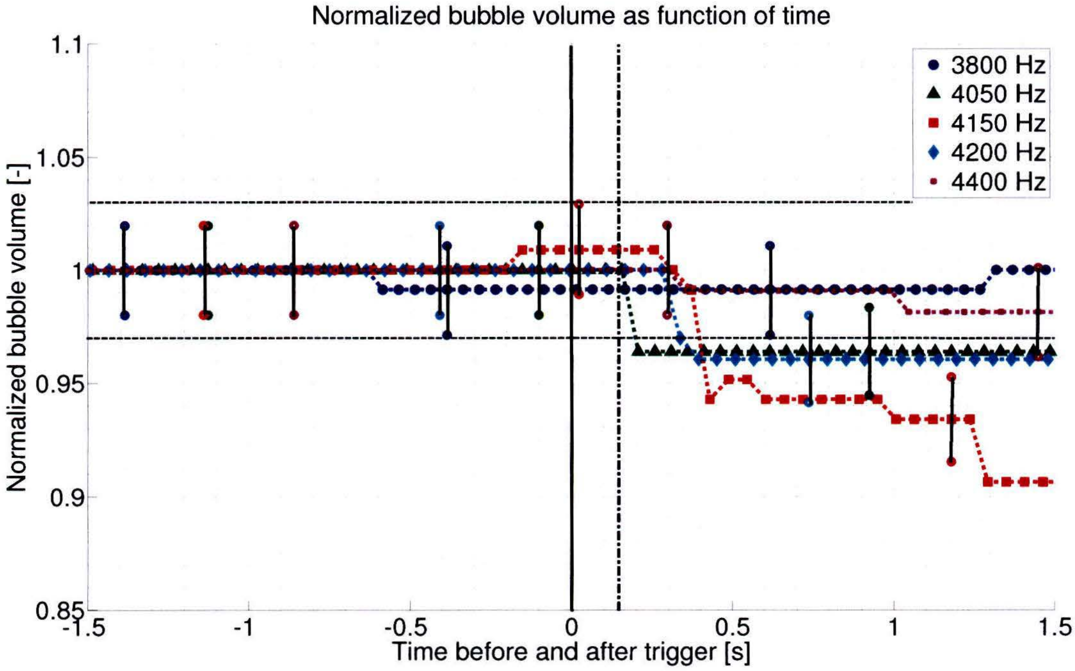

(b) Normalized bubble volume as function of time before and after trigger. The symbols indicate the volumes of the vapor bubbles.

Figure 5.10: Bubble volume as function of time before and after trigger. The black solid vertical line at $t = 0$ corresponds to the trigger of the camera and the wave-generator, whereas the black dotted vertical line at $t \approx 0.15$ corresponds to the time delay of the sound setup.

in section 2.2). Despite of the large errors in the analysis, we find the largest decrease in bubble volume with frequencies equal to - or close to - the resonance frequency of the growing vapor bubble.

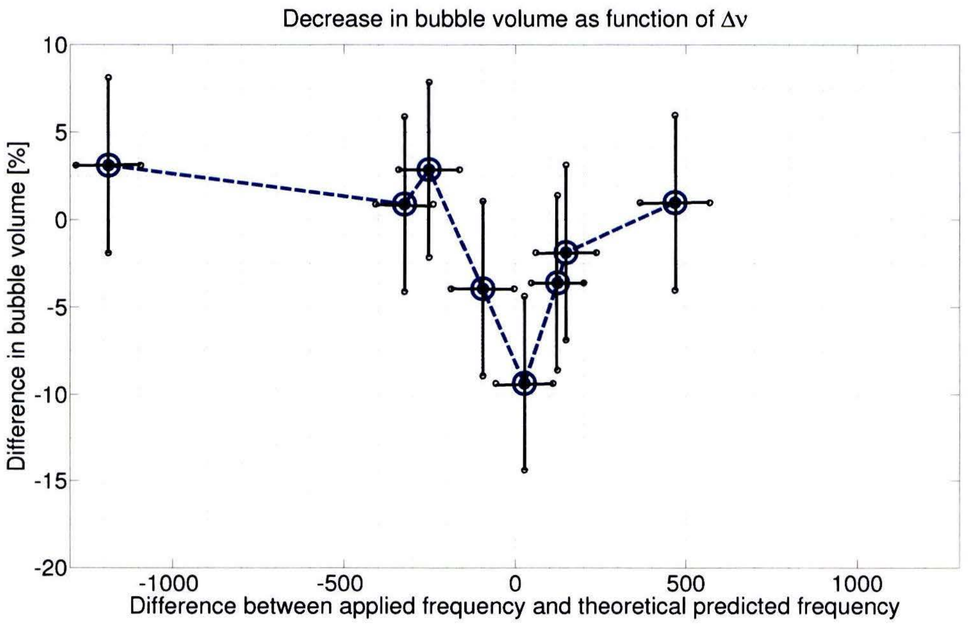

Figure 5.11: Decrease in bubble volume as function of the difference in frequency $\Delta\nu$. The black lines are the error bars, with a maximum error of ± 102 Hz in horizontal direction and ± 5% in vertical direction. The horizontal error is a result of the error of one pixel (2 %) in the determination of the radius.

5.3.3 Effect of sound on bubble growth times

The bubble growth times of the bubbles before and after the trigger with sound are presented in figure 5.12. To compare the growth times, we normalized the growth times with respect to the mean: the fluctuations in bubble growth time correspond in this way to the standard deviation σ_d. The horizontal dashed lines are the error bars, which cover the standard deviation of approximately ± 5.6 %. This error is based on the assumption of one frame error with respect to the minimum of 18 frames of growth time per bubble ($\frac{1}{18} = 0.056$).

The bubble growth of all bubbles fluctuated with ± 1 frame before and after the trigger. However, it can be observed that the bubble growth times of the bubbles in measurement number 5 decrease almost immediately after the delay of the sound setup with approximately 9 %. It seems that the sound has (almost) no influence on the other measurements. The frequency dependence of the waves can therefore be observed in the growth times of the bubbles as well.

5.3.4 Effect of sound on waiting time

The waiting times for the different measurements performed with the SSBG2 are presented in figure 5.13 as function of time. The waiting times in measurement numbers 2 and 4 are shorter than the waiting times in the other measurements. This is of course as expected since the bubble volumes in measurement number 2 and 4 are the largest. The vertical black line indicates the trigger of the camera and the wave generator. The vertical dashed line indicates the delay of the sound setup.

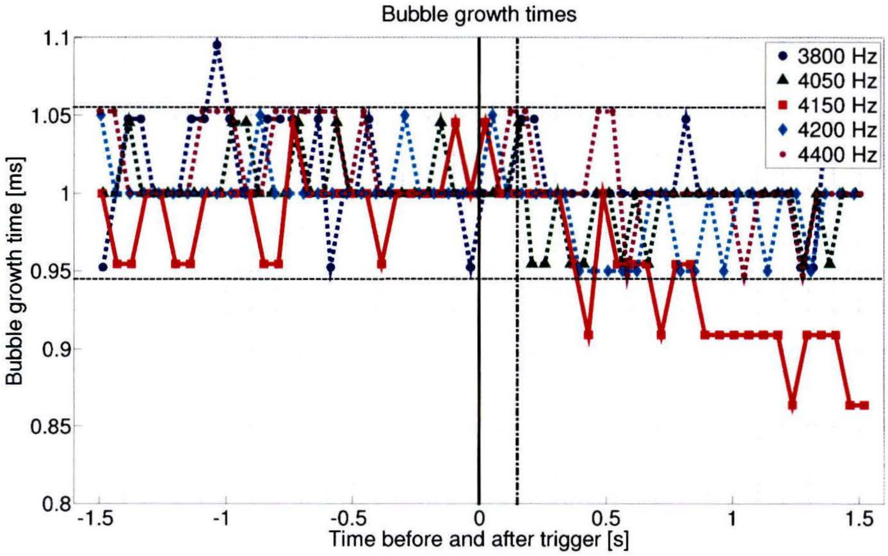

Figure 5.12: Bubble growth times as function of time before and after the trigger. The horizontal error bars correspond to the error of one frame equal to 5.6%.

There is almost no difference in the waiting time before -and after the triggering and no effect of acoustic excitation can be observed. Again we conclude that acoustic excitation has no effect on the waiting time between two adjacent bubbles.

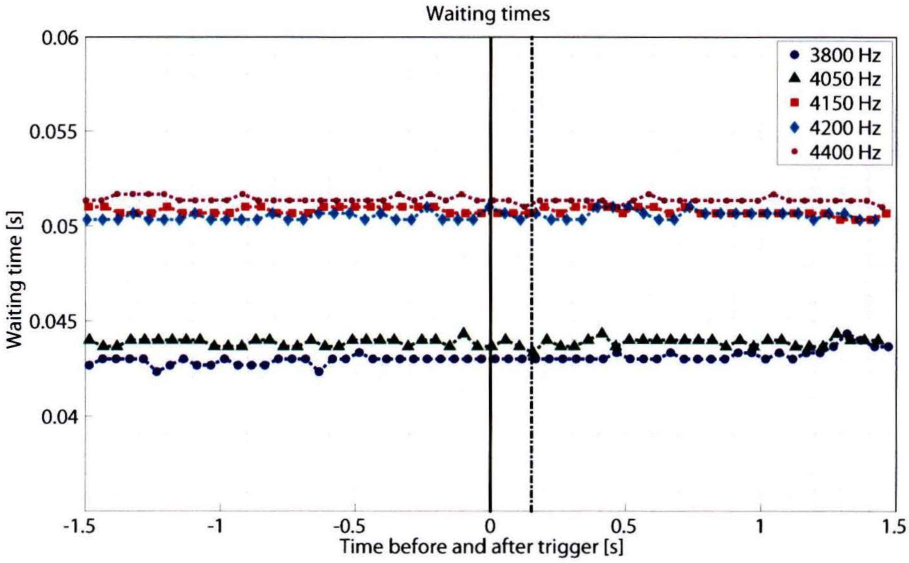

Figure 5.13: Waiting times between two adjacent bubbles as function of recording time. No change in waiting time occurs after the trigger.

Since the bubble growth times can be decreased without affecting the waiting times, we are able to increase the bubble departure frequency using acoustic excitation.

5.3.5 Temperature registration

During all measurements the bulk temperature is registrated. We tried to measure the wall temperature with a PT-100 sensor located on top of the thin sheet, however this did not give satisfying results. As a consequence, only the bulk temperature as function of time for each measurement is known. The change in bulk temperature as function of time should be enough to explain changes in bubble volume which are not induced by the acoustic waves.

In the previous experiments with the SSBG1 the heater wall did almost not changed in tem-

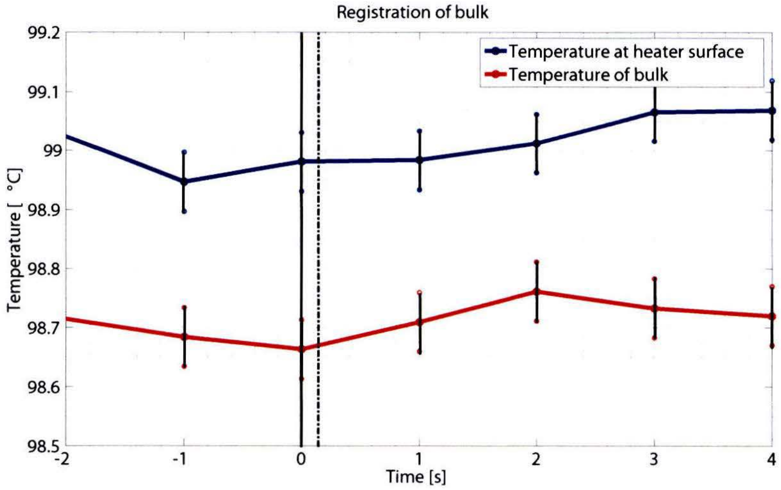

(a) Temperature registration of the bulk with and without sound (4150 Hz)

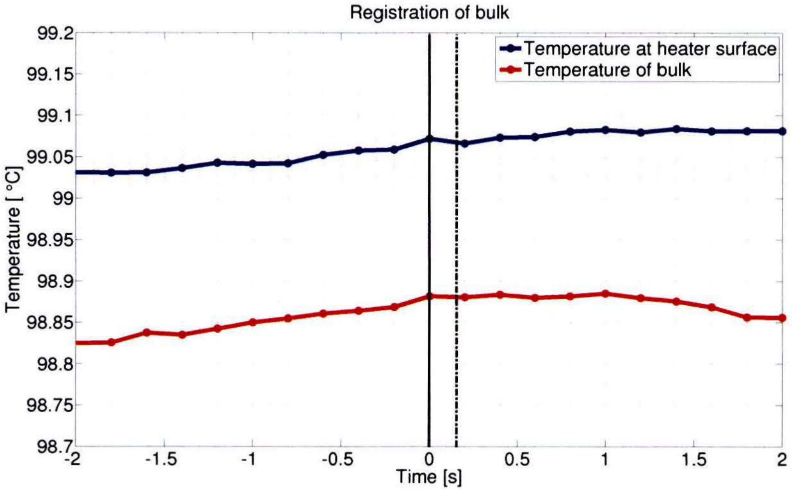

(b) Temperature registration of the bulk with and without sound (4050 Hz)

Figure 5.14: Temperature registration of bulk before and after the trigger of sound.

perature, since a constant power was applied to the heater. The experiments using the SSBG2 are performed under approximately the same boiling conditions. It is therefore assumed that the superheat ΔT will be in the order of 8 ° Celsius.

The temperature of the bulk during measurement number 5 (frequency 4150 Hz) is given in figure 5.14(a). Unfortunately the sampling rate in *Labview* was only 1 Hz instead of 5 Hz, resulting in a less accurate measurement. For this reason, error bars corresponding to $\pm$ 0.05° Celsius are introduced. It can be observed that after the trigger a small increase in bulk temperature occurs. This increase can of course not lead to smaller boiling bubbles and the decrease in bubble volume should be the effect of the applied acoustic waves. Figure 5.14(b) shows the temperature of the bulk during measurement number 4. Again, almost no change in the bulk temperature occurred after the trigger.

5.4 Anisotropic first order Lamb mode

Besides the experiments with acoustic excitation in the volumetric Rayleigh-Plesset mode, we performed experiments with acoustic excitation in the first order Lamb mode. These experiments are performed with the SSBG1.

5.4.1 Measurement configuration

The measurements are recorded with a frame rate of 3000 frames per second with a resolution of 512 x 256 pixels. The applied power was maintained at a value of $Q_{\text{power}} = 7.5$ [W], whereas the temperature of the bulk was slightly varied per measurement (around 98° Celsius). The wall temperature of the bubble generator is calculated using relation 4.3 obtained by the calibration measurements. The pixel to millimeter ratio is calibrated as:

$$\frac{\text{pixels}}{\text{millimeter}} = \frac{222 \pm \Delta 2}{3.10 \pm \Delta 0.01}$$

resulting in the size of one pixel equal to 0.0140± 0.0001 millimeters.

5.4.2 Effect of sound on bubble volume

The effects of excitation in the first order Lamb mode are investigated. The frequencies corresponding to this mode are located around 100 Hz for the generated bubbles. Figure 5.15 shows the bubble volumes in three measurements before and after the trigger with sound.

For the best comparison with the Rayleigh-Plesset mode, it was tried to generate bubbles which have the same bubble volume. Figure 5.15(a) shows that the bubble volumes during the experiments with applied frequency of 100 Hz and 130 Hz are in the order of 5 mm^3, which is in correspondence with the volumes of the bubbles generated with the SSBG1 during the volumetric excitation. The bubbles generated in the experiment with applied frequency of 70 Hz are larger. Therefore, these bubbles should have the lowest resonance frequencies.

Figure 5.15(b) shows the normalized bubble volumes. The figure is normalized with respect to the volume of the first bubble. To investigate the frequency dependence of the acoustic waves in the first order Lamb mode we recall equations 2.36 and 2.43:

$$\omega_{L_{\text{wall}}} = \frac{\omega_L}{1.9} \qquad \text{where} \qquad \omega_{\text{L}} = \sqrt{\frac{12\sigma}{\rho_l R^3_{t=0}}} \tag{5.3}$$

The values for saturated water can be found in table 2.1. The bubble radii of the bubbles before the trigger are given in table 5.3 together with the theoretical predicted values and the difference between applied frequency and predicted frequency.

The theoretical resonance frequencies of the bubbles in the three different measurements are located very close to each other. Even the large bubbles with volumes equal to 6.5 mm^3 have a resonance frequency that is located very close to the resonance frequencies of bubbles which are 23 % smaller in volume! Moreover, since the frequencies are so low, the error as a result of pixel determination is very small. It is therefore much easier to excite the bubbles in their first order resonance mode and observe some effects.

It can be observed that the volumes of all bubbles decrease immediately after the triggering of sound. After approximately 1 second the decrease in volume stops and the volumes stay at a constant value or increase. After 3 seconds it seems that the bubble volumes are stabilized again and have lower volumes than before the sound was applied.

This behavior can be an effect of the pressure in the boiling pot as will be discussed in the next chapter, however it might have another reason. Namely, it was observed that at the triggering of the sound the speaker showed a large startup response, which could cause the bubble to detach. More than once the membrane broke during the excitation and water could flow unhindered from the reservoir to the boiling pot as will be shown in the temperature plots.

Nonetheless, a decrease in bubble volume was observed during the recordings, where the decrease in temperature at the position of the bubble generator occurred 4 seconds after the trigger. It is very hard to draw useful conclusions, since it is clear that the oscillating speaker influences the setup. On the other hand we observe a significant decrease in bubble volume, before the temperature of the bulk was decreased. Since it is easier to excite the growing

#	ν_{applied}[Hz]	$R_{bubble}[mm]$	$\nu_{RP_{wall}}$[Hz]	$\Delta\nu = \nu_{\text{applied}} - \nu_{RP_{wall}}$ [-]	Volume decrease [%]
1	70	1.110 ± 0.014	61 ± 2	9 ± 2	12.9 ± 3
2	100	1.019 ± 0.014	70 ± 2	30 ± 2	18.8 ± 3
3	130	1.005 ± 0.014	71 ± 2	59 ± 2	15.0 ± 3

Table 5.3: Frequency dependence of bubbles in the four different measurements. The table shows the numbers corresponding to the different measurements in the first column, the applied frequency of sonic wave in the second column, bubble radius right before trigger in the third column, theoretical predicted value of volumetric resonance mode at wall in the fourth column and difference between applied frequency and theoretical resonance frequency in the fifth column. The last column shows the decrease in percentage bubble volume. The errors in the table are the maximum possible errors made in the determination of the bubble size (1 pixel error (1.4 %) in determination of bubble radius and 3% in bubble volume).

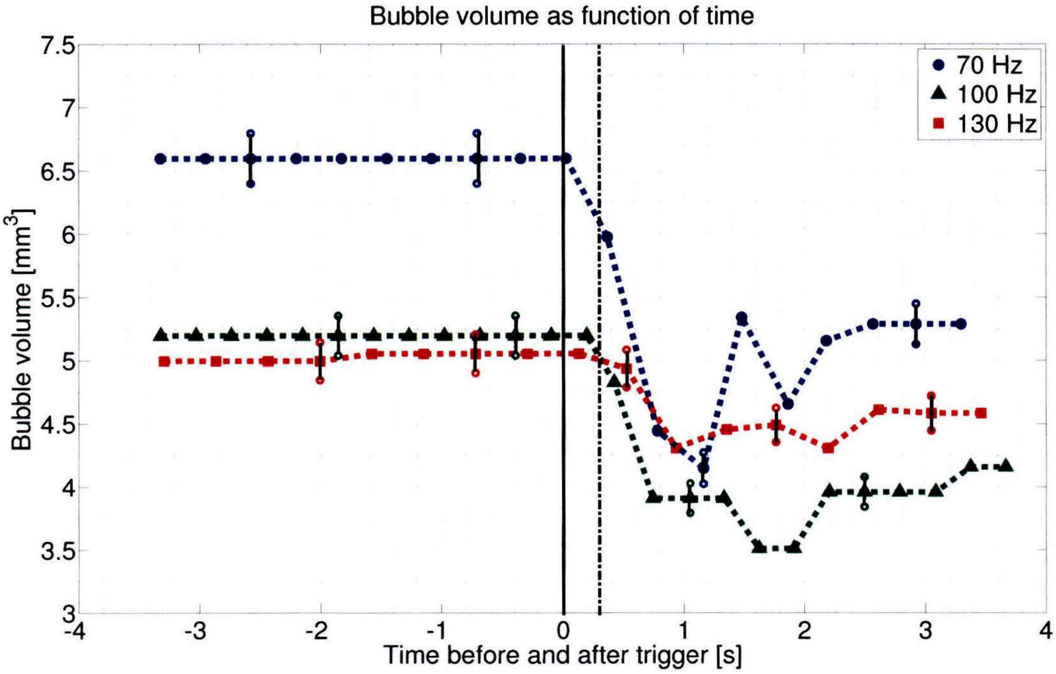

(a) Bubble volume as function of time before and after trigger. The symbols indicate the volumes of the vapor bubbles.

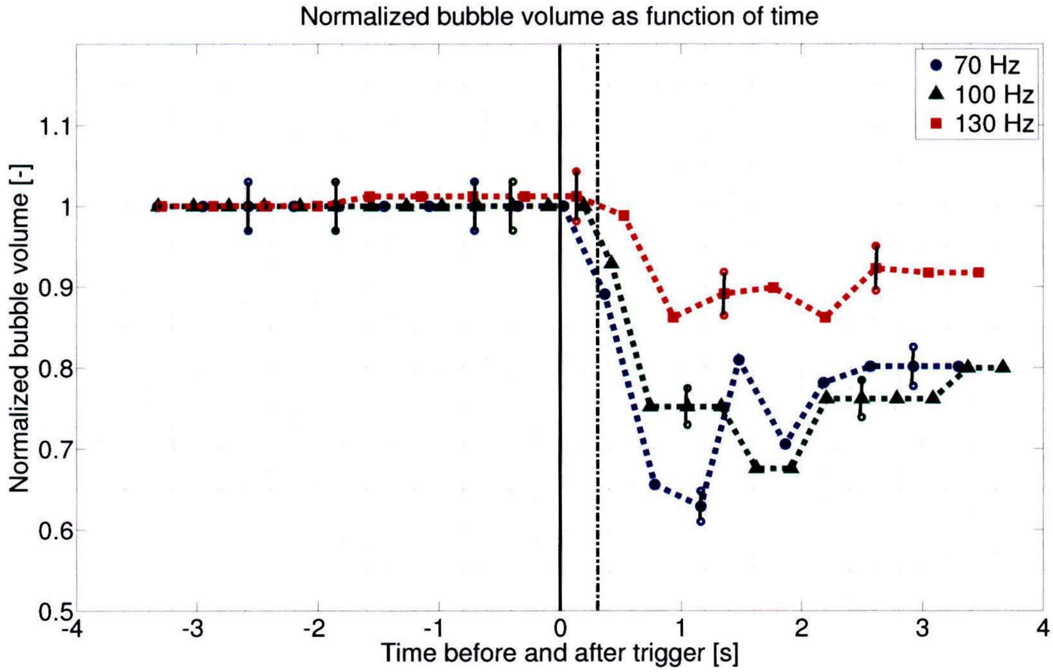

(b) Normalized bubble volume as function of time before and after trigger. The symbols indicate the volumes of the vapor bubbles.

Figure 5.15: Bubble volume as function of time before and after trigger. The black solid vertical line at $t = 0$ corresponds to the trigger of the camera and the wave-generator, whereas the black dotted vertical line at $t \approx 0.15$ corresponds to the time delay of the sound setup.

vapor bubbles in the first order Lamb mode than in the volumetric mode, it is of interest to do more investigation with (acoustic) excitation in this mode.

5.4.3 Effect of sound on bubble growth times

The effect of acoustic excitation on the bubble growth times is given in figure 5.16. The bubble growth times decrease after the trigger with sound and show the same behavior: the largest decrease in growth time occurs in the first second and it stabilize after three seconds. A decrease of maximum 10 % in bubble growth time can be observed.

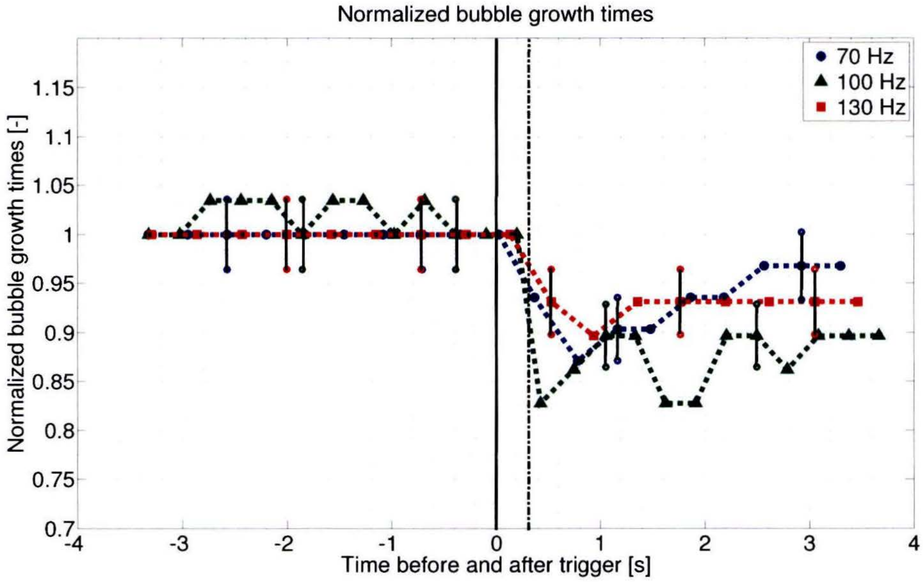

Figure 5.16: Bubble growth times before and after the trigger. The error bars correspond to an error of 3.6 %.

Without sound the bubbles have a growth time of approximately 28 frames. The error is equal to 1 frame, which results in an error of 3.6 %.

5.4.4 Effect of sound on waiting time

The waiting times are given in figure 5.17. It can be observed that the waiting time decreases immediately after the triggering of sound. This supports the conclusion that the start up response of the speaker detaches the bubble from the bubble generator. The subsequent waiting time is much longer, which indicates that it takes more time to generate a new bubble. After the startup effect of approximately one second, the waiting times return to their corresponding value as it was before the triggering. Once more it seems that the sound has no influence on the waiting time, except during the start up of the sound with low frequencies, but this seems rather a setup issue.

5.4.5 Temperature registration

The temperature of the bulk and heater wall during the measurement with applied acoustic waves of 70 Hz are presented in figure 5.18. The bulk is measured at two positions: one PT-100 sensor is located inside the pool boiling pot above the bubble generator, whereas the other PT-100 sensor is located near the membrane.

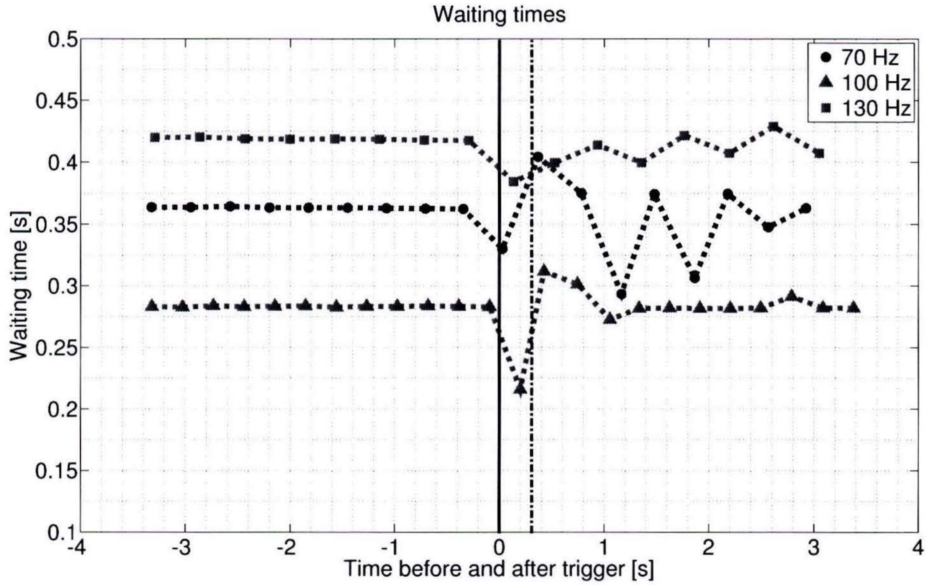

Figure 5.17: Waiting times between two adjacent bubbles as function of recording time. The waiting times are disturbed by the sound trigger. After approximately one second the waiting times return to their original values.

It can be observed from figure 5.18(a) that the temperature near the membrane decreases very rapidly in one second after the triggering. This is a fact of the broken membrane between the reservoir and the pool boiling pot. However, the decrease in temperature near the bubble generator is not as significant as it is near the membrane. During the performed measurement, the temperature near the bubble generator only decreased 0.05° Celsius, whereas the temperature of the heater wall was almost constant. The superheat, ΔT, which is the driving force of bubble growth, increased approximately one tenth of a degree as is indicated in figure 5.18(c). The temperature profile near the bubble generator should therefore not result in the growth of smaller bubbles.

It is very hard to draw a conclusion about the effect of *acoustic* excitation on the bubble detachment. It is proved that the volume and growth times of the bubbles decrease significantly as they are excited by acoustic waves with a frequency close to the first order anisotropic resonance mode. Moreover, the effects were observed while the temperatures near the bubble generator did not changed.

On the other hand, it is observed that both the oscillations and the startup effect of the speaker have influence on the present setup. It seems that a stable state is reached after approximately three seconds, where the bubble volumes and bubble growth times are smaller

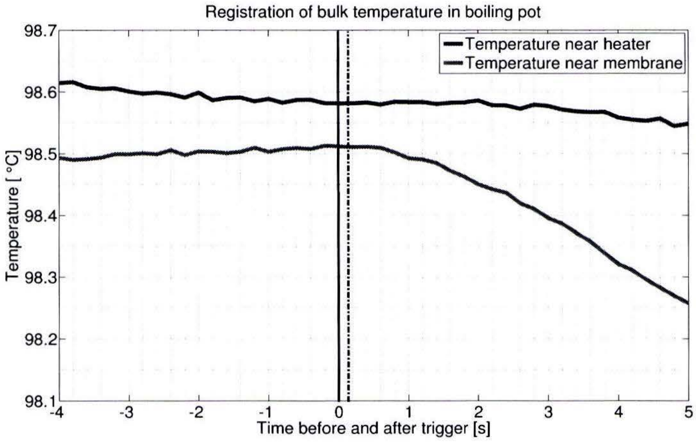

(a) Temperature registration of the bulk with and without sound corresponding to the case of excitation with 70 Hz.

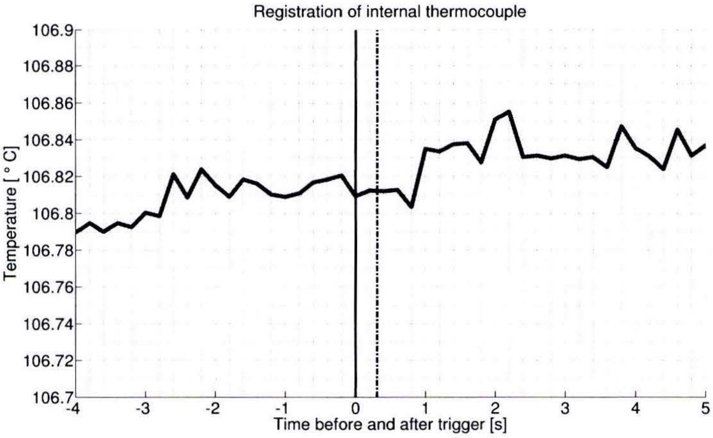

(b) Temperature registration of the internal thermocouple with and without sound corresponding to the case of excitation with 70 Hz

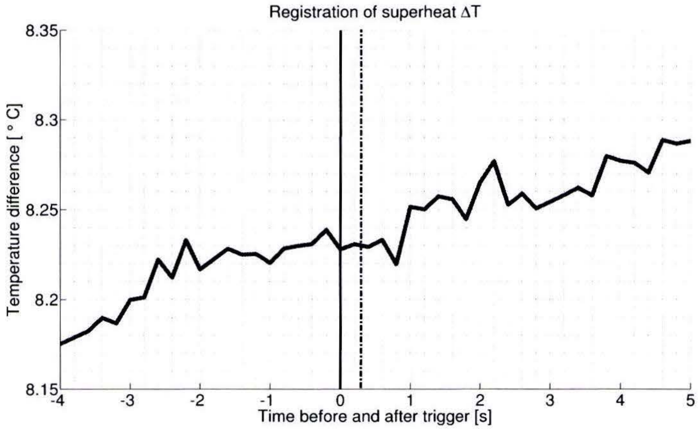

(c) Superheat temperature with and without sound corresponding to the case of excitation with 70 Hz

Figure 5.18: Temperature registration of bulk before and after the trigger of sound.

with acoustic excitation than without excitation. It was impossible to measure at frequencies below 70 Hz with the present setup. Therefore we were not able to investigate if the observed effect is a resonance response of the bubbles to the induced acoustic pressure waves or not.

Chapter 6

Discussion

In this chapter we take a closer look at the obtained results and investigate the influence of the volume decrease on the heat transfer. It will be concluded if we succeeded to enhance the heat transfer.

6.1 Pressure field in experimental setup

We start the discussion of the results by presenting simulations performed in COMSOL to map the pressure field of the present setup. Since we excite the bubbles with continuous waves with frequencies in the audible range, where the wavelengths are at least 30 centimeter, standing waves occur in the setup and the pressure field becomes very complex. It was very hard to measure the pressure field at the position of the bubble generator and to quantify the losses of the sound to the surroundings. The losses to the surroundings are significant, since we needed to wear ear plugs to prevent hearing damage.

The pressure at the position of the bubble generator (in the exact center of the pool boiling pot) as function of time is presented in figure 6.1. The simulations are performed in a two-dimensional space without taking the startup effects of the sound setup into account. It was tried to calculate the pressure field for a total of four seconds, however since we have no insight in the pressure losses to the surroundings (via the air, the setup, the table etc.) this was not possible. Nonetheless, the simulation of the pressure field as function of time for only 0.1 second give enough inside in the complex pressure field inside the pot.

It can be observed that large fluctuations in pressure amplitude occur at the position of the bubble generator. The bubbles are therefore excited with pressure waves where the amplitude varies in time. It depends on time whether a bubble is excited with a large peak in the pressure or whether the pressure is at a minimum. The decrease in bubble volume is related to the frequency of the applied waves, but the amplitude of pressure also plays an important role. The oscillations in the bubble volumes as function of time that occur during the excitation with acoustic waves is probably the effect of the standing wave pattern inside the pool boiling pot.

Furthermore the continuous pressure wave might lead to pressure increase as function of time inside the pot, which results in larger decrease in bubble volume as function of time as was observed in the presented results. The wavelengths in the case of acoustic excitation with frequencies equal to 70 Hz correspond to 20 meter, so a more complex standing wave pattern inside the pot is expected. The induced standing wave pressure pattern can lead to the observed decrease and increase in bubble volume as function of time.

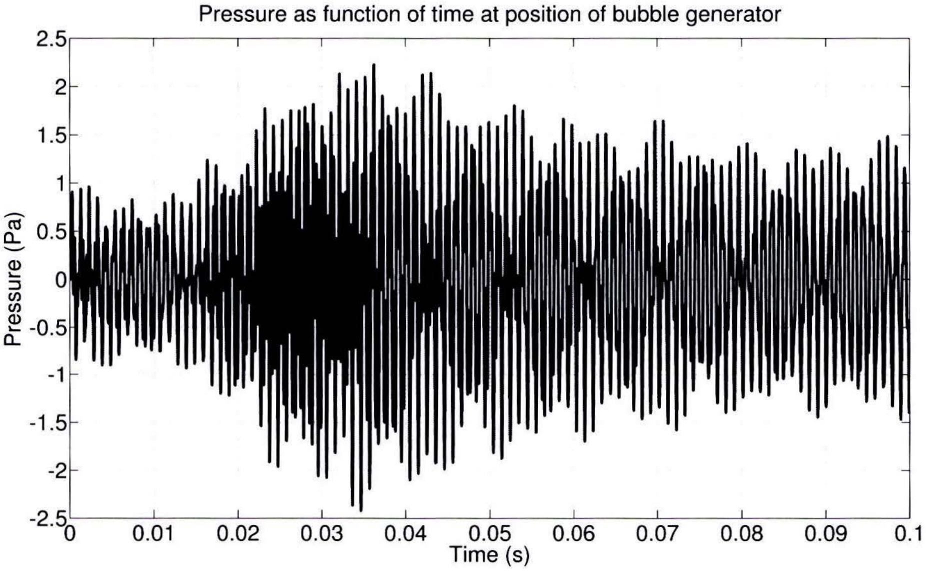

Figure 6.1: Simulation of pressure field with frequency 3000 Hz. Simulations are performed in COMSOL for the first 0.1 seconds, without taking startup effects into account.

It seems that the higher the pressure of the acoustic waves, the larger the decrease in bubble volume. It is of interest to investigate if higher pressures are able to influence the detachment of boiling bubbles even if the applied frequency is not very close to the resonance frequency of the bubbles.

The conclusion can be drawn that the induced pressure field and corresponding standing wave pattern inside the pot have influences on the bubble growth. It is of importance to measure the losses of the waves to the surroundings and to measure the pressure as function of time inside the boiling pot to get more insight in the importance of the pressure on bubble detachment. In the present work we used figure 6.1 to find possible explanations for the decrease and oscillations in bubble volume as function of time.

6.2 Frequency dependence in different measurements

In the measurements where we excited the bubble with acoustic waves with frequencies corresponding to the isotropic volumetric mode of the bubble, we found a frequency dependence. Both 'v-shaped' plots are presented in figure 6.2. It can be observed that $\Delta\nu$ was smaller in the measurements with the larger bubbles and more percentage volume decrease was obtained during these measurements. Moreover, it can be observed - as far as possible with this number of measurements - that the peak of the larger bubbles is smaller than it is for the small bubbles. This is in correspondence with the forced damped linear oscillator, since smaller bubbles are expected to have a higher damping, which results in a wider and lower resonance peak.

Figure 6.2(c) shows both 'v-shaped' plots combined into one. In this way the frequency dependence of all measurements together can be observed. The conclusion can be drawn that the decrease in bubble volume is closely related to the applied frequency of the waves. The closer the applied frequency to the resonance frequency of the bubbles, the larger the volume decrease.

6.3 Heat transfer

In this section we investigate the effect of the decrease in bubble volume with respect to heat transfer. This will be done with use of the results from the measurement performed with the SSBG1 where the largest decrease in bubble volume was obtained.

6.3.1 Energy equation

The energy equation valid at the position of the bubble generator was derived in section 4.6.5. The equation is the starting point of the heat transfer analysis. The energy equation is presented below and the different heat transfer mechanisms are indicated.

$$\boxed{\underbrace{Q_{\text{power}}}_{\text{applied power}} = \underbrace{\rho_v \cdot V_{\text{bubbles}} \cdot h_{ev} \cdot f \cdot N_a}_{\text{energy transported by bubbles}} + \underbrace{h \cdot A \cdot (T_{\text{wall}} - T_{\text{bulk}})}_{\text{convection}} \quad [\text{W}]} \tag{6.1}$$

During the measurements, the values of N_a [#], ρ_v [kg/m^3], h_{ev} [J/kg], A [m^2] and the applied power Q_{power} [W] did not change. These values are given in table 6.1.

The other four variables can change during the measurement, namely the heat transfer coefficient h [W/(m^{2}K)], the superheat ΔT [$^\circ C$], the bubble volume V_{bubbles} [mm^3] and the departure frequency f [Hz]. It can easily be observed that a decrease in bubble volume should result in an increase of the heat transfer coefficient as long as the superheat ΔT is not changed.

ρ_v [kg/m^3]	h_{ev} [J/kg]	A [m^2]	N_a [#]	Q_{power} [W]
0.598	$2.2570 \cdot 10^6$	$1 \cdot 10^6$	1	7.4

Table 6.1: Typical values corresponding to the measurement with applied frequency 2730 Hz.

6.3.2 Heat transfer enhancement of present work

To calculate the heat transfer enhancement in the present work, we take the measurement where the largest decrease in percentage bubble volume occurred. For the analysis we have to recall the superheat before and after the trigger (figure 5.5(c)) and the bubble volume before and after the trigger (figure 5.1(a)).

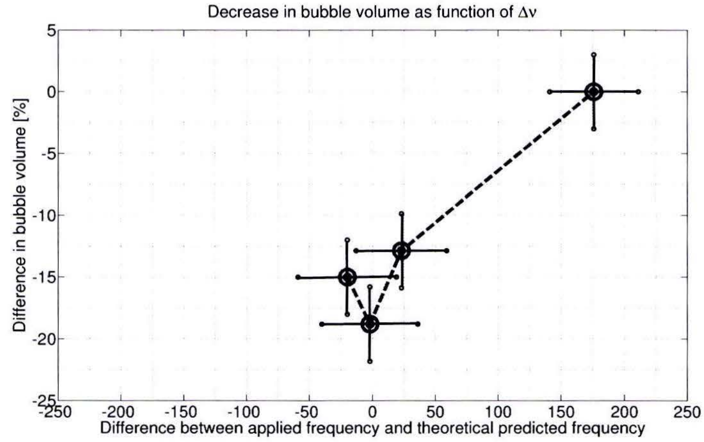

(a) Frequency dependence of measurements performed with the SSBG1 in the volumetric mode

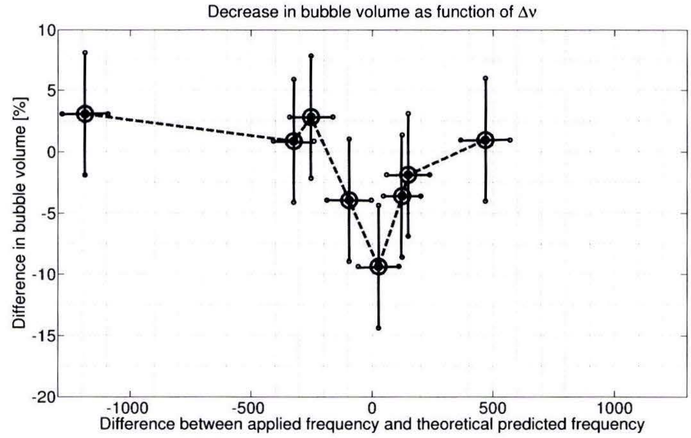

(b) Frequency dependence of measurements performed with the SSBG2 in the volumetric mode

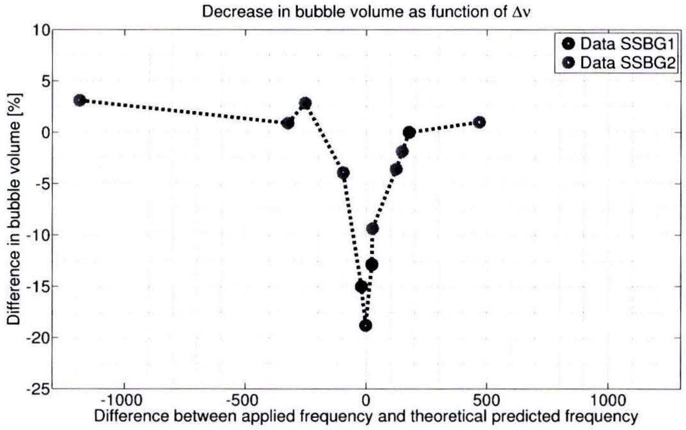

(c) Frequency dependence of both measurements in one plot. The frequency dependence on the decrease in bubble volume is nicely visualized.

Figure 6.2: Frequency dependence of measurements performed in volumetric Rayleigh-Plesset mode

It was observed that the superheat ΔT (see figure 6.3) did almost not changed during the performed experiment. Before the trigger with sound the superheat was approximately 7.65° Celsius, whereas after the trigger the superheat decreased to approximately 7.6° Celsius.

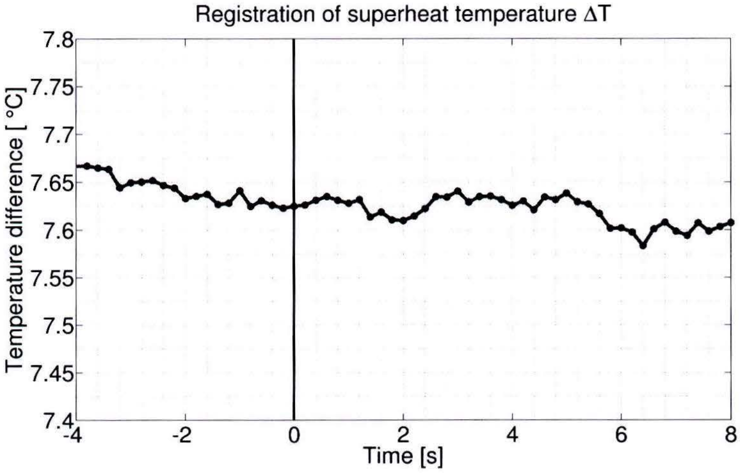

Figure 6.3: Registration of superheat temperature Δ T

The bubble volume before and after the trigger is given in figure 6.4. We consider the case of 2730 Hz which corresponds to the green line (triangle) in the figure. The bubble volume before the trigger is equal to 5.2 ± 0.16 mm^3, whereas the smallest volume after the trigger is equal to 4.2 ± 0.12 mm^3

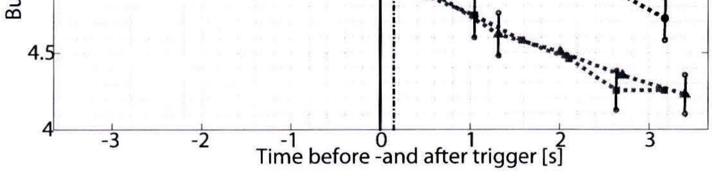

Figure 6.4: Bubble volume as function of time before and after trigger. The vertical lines are the error bars, where the maximum error is 3%. The symbols indicate the volumes of the vapor bubbles at detachment.

The bubbles departed 0.7 milliseconds faster with acoustic excitation, while the waiting times were constant at a value of 0.69 ± 0.05 seconds. The growth time plus waiting time determines the departure frequency. For the present case the growth time plus waiting time equals 0.70 ± 0.05 seconds without sound and 0.69 ± 0.05 seconds with sound. The bubble departure frequency is thus increased with approximately 1.4 %. From the recordings we know that 6 bubbles departed in 3.65 seconds, resulting in a departure frequency of $f = 1.6$ [Hz]. The increased bubble departure frequency with the application of sound is therefore $f = 1.7$ [Hz]

Now we are able to make the calculation for the situation without sound:

$$\underbrace{7.4}_{\text{applied power}} = \underbrace{0.598 \cdot 5.2 \cdot 10^{-9} \cdot 2.2570 \cdot 10^{6} \cdot 1.6 \cdot 1}_{\text{energy transported by bubbles}} + \underbrace{h_{\text{before}} \cdot 1 \cdot 10^{-6} \cdot 7.65}_{\text{convection}} \quad [\text{W}] \tag{6.2}$$

whereas the calculation with sound is given by:

$$\underbrace{7.4}_{\text{applied power}} = \underbrace{0.598 \cdot 4.2 \cdot 10^{-9} \cdot 2.2570 \cdot 10^{6} \cdot 1.7 \cdot 1}_{\text{energy transported by bubbles}} + \underbrace{h_{\text{after}} \cdot 1 \cdot 10^{-6} \cdot 7.6}_{\text{convection}} \quad [\text{W}] \tag{6.3}$$

6.3.3 Efficiency

It is clear that the heat transfer coefficient has to increase. The heat transfer coefficient before the applied acoustic waves is equal to $h_{\text{before}} = 9.658 \cdot 10^5$ [W/(m^{2}K)], whereas the heat transfer coefficient after application of sound is equal to $h_{\text{after}} = 9.724 \cdot 10^5$ [W/(m^{2}K)]. This results in an increase of

$$1 - \frac{9.658}{9.724} = 0.68\% \tag{6.4}$$

The decrease in power transported by the vapor bubbles is equal to

$$1 - \frac{4.2 \cdot 10^{-9} \cdot 1.7}{5.2 \cdot 10^{-9} \cdot 1.6} = 0.143 = 14.3\% \tag{6.5}$$

Since we have approximately two bubbles generated per second in the pool boiling pot, the heat transfer enhancement in the present setup is very low. However, we succeeded to reduce the power transported by the vapor bubbles with 14.3 %. It is of importance to investigate if we can tune some design parameters - think of the number of active nucleation sites per area N_a'', or the bubble departure frequency f - to increase the efficiency.

6.3.4 Order estimation of heat transfer mechanisms

To make an estimation of the possible increase, an order estimation is performed first. The energy equation with the different orders of magnitude is given in equation 6.6.

$$\underbrace{Q_{\text{power}}}_{\mathcal{O}(1)} = \underbrace{\underbrace{\rho_v}_{\mathcal{O}(1)} \cdot \underbrace{V_{\text{bubbles}}}_{\mathcal{O}(10^{-9})} \cdot \underbrace{h_{ev}}_{\mathcal{O}(10^{6})} \cdot \underbrace{f}_{\mathcal{O}(1)} \cdot \underbrace{N_a}_{\mathcal{O}(1)}}_{\mathcal{O}(10^{-3})} + \underbrace{\underbrace{h}_{\mathcal{O}(10^{5})} \cdot \underbrace{A}_{\mathcal{O}(10^{-6})} \cdot \underbrace{(T_{\text{wall}} - T_{\text{bulk}})}_{\mathcal{O}(10)}}_{\mathcal{O}(1)} \quad [\text{W}] \tag{6.6}$$

It follows from the order analysis that the power transported away from the heater surface is approximately 0.1 % of the total heat transfer.

6.3.5 Design parameters

The power of the transported energy is in the present setup equal to 0.0112 Watt without acoustic excitation and 0.0096 Watt with acoustic excitation. The difference in Watts is equal to $0.0112 - 0.0096 = 0.0016$. For a noticeable increase in the heat transfer, this difference in power needs to be at least 1 % of the power that is convected.

There are different design parameters that can possibly be tuned: the bubble departure frequency f, the surface A, the superheat ΔT, the applied power Q_{power} and the number of active nucleation sites N_a.

Bubble departure frequency

An increase in the bubble departure frequency results in a higher power that is transported by the bubbles to the fluid. However, to obtain a higher bubble departure frequency the applied power to the heater needs to be increased. Increasing the applied power results in a higher heater wall temperature and a higher superheat ΔT. This will of course lead to a higher convection rate and no increase in heat transfer coefficient is observed.

Superheat

The convective heat transfer can be decreased by a decrease in the superheat ΔT. However, the superheat determines the bubble growth and a lower superheat results in smaller bubbles and a lower departure frequency. By decreasing the superheat it is not possible to obtain a increase in the heat transfer of more than 1 %.

Applied power

To increase the ratio of energy that is transported away by the bubbles with respect to the energy that is convected, we can decrease the applied power. A decrease in applied power will result in a lower superheat, smaller bubbles and a lower bubble departure frequency. Again, no increase larger than 1 % in the heat transfer coefficient can be obtained.

Surface

An increase in surface increases the convective heat transfer. If the applied power is maintained at a constant level, the energy flux in Watts per unit area decreases, which results in smaller bubbles. Increasing the applied power, leads to a higher superheat ΔT and the convective heat transfer is increased even more.

Number of active nucleation sites

The only design parameter that can be tuned which leads to an increase in the transported power by the vapor bubbles and decreases the convective heat transfer is the number of active nucleation sites. If the active number of nucleation sites is tenfold, the increase in heat transfer coefficient is still in the order of 1%. If the number of active nucleation sites can be increased up to fifty sites, the increase in the heat transfer coefficient is more than 3 %.

6.3.6 Maximum possible heat flux transported by vapor bubbles

In this subsection we estimate the highest possible heat flux that can be transported by vapor bubbles in pool boiling. Herefore, we take the maximum departure frequency equal to the final rise velocity of the vapor bubbles, separated by the theoretical smallest possible distance. This smallest possible distance is the distance between the centers of two rising bubbles. The final rise velocity, u_{bubbles}, of spherical bubbles can be derived by equating the buoyancy force to the drag force [12]:

$$\begin{aligned} \frac{1}{2} \cdot c_D \cdot \rho_l u^2_{\text{bubbles}} \cdot \frac{\pi}{4} D^2_{\text{bubble}} &= \frac{pi}{6} D^3_{\text{bubble}} (\rho_l - \rho_v) \cdot g \\ \rightarrow u_{\text{bubbles}} &= \sqrt{\frac{4 D_{\text{bubble}} g}{3 c_d}} \end{aligned} \tag{6.7}$$

If we take the value $c_D \approx 0.4$ as the drag force coefficient and set the highest possible number of active nucleation sites equal to the reciprocal value of the projected bubble area of a single bubble [12], we can rewrite equation 4.6 into the following form:

$$\begin{aligned} q''_{\text{bubbles, max}} &= \rho_v \cdot V_{\text{bubbles}} \cdot h_{ev} \cdot \frac{u_{\text{bubbles}}}{D_{\text{bubble}}} \cdot \frac{1}{\frac{\pi}{4} D^2_{\text{bubble}}} \\ &= \sqrt{\frac{16 \rho_v^2 g D_{\text{bubble}} h^2_{ev}}{27 c_D}} \end{aligned} \tag{6.8}$$

If we take the values for water as presented in table 6.1, $c_D = 0.4$ and the bubble diameter equal to a typical value of 2 millimeter it follows for the maximum possible heat flux transported by the bubbles:

$$q''_{\text{bubbles, max}} = \sqrt{\frac{16 \cdot 0.598^2 \cdot 9.81 \cdot 0.002 \cdot (2.2570 \cdot 10^6)^2}{27 \cdot 0.4}} = 2.3 \cdot 10^5 \quad [\text{W/m}^2] \tag{6.9}$$

The maximum possible heat flux transported by the bubbles is in the order of $\mathcal{O}(10^5)$ [W/m^2]. This is an order of ten smaller than the maximum possible heat transfer rate in pool boiling ($\mathcal{O}(10^6)$ [W/m^2]).

With the use of acoustic excitation we were able to decrease the bubble volume with 20 ± 3 %, which resulted in a decrease of 14 % of transported power by the vapor bubbles. A decrease of 14 % in the heat transfer mechanism that is not the prevailing mechanism during pool boiling, results in an increase of the heat transfer coefficient of maximum 2 % if the design parameters are tuned.

In the present setup we increased the heat transfer rate with maximum 2 %. This corresponds with a surface of 1 mm^2 to an enhancement of 0.01 W/K. The applied power to the speaker however, is much larger. The ratio effiency/additional applied power is very bad. It depends on the amount of increased heat transfer and the addition applied power to the transducer if acoustic excitation is efficient enough to enhance the heat transfer.

Chapter 7

Conclusions and future work

7.1 Conclusions

7.1.1 Excitation in volumetric resonance mode

Experiments are performed where vapor bubbles are excited by acoustic waves which have frequencies close to the resonance frequencies of the vapor bubbles. Two different sets of experiments with excitation in the volumetric mode are performed: the first set of measurements consisted of large vapor bubbles, whereas the other set had smaller bubbles. In both sets of measurements the applied conditions were almost identical.

It was observed that a decrease in bubble volume can be obtained if the bubbles are excited by waves with applied frequencies very close to the theoretical predicted resonance frequencies of the bubbles. In experiments where the applied frequency was not close, no effect in bubble decrease was observed. From the performed measurements, a very clear resonance response of the bubbles was observed. The influence of temperature on the decrease in bubble growth is investigated and can be excluded. Therefore, the obtained decreases have to be an effect of the acoustic pressure waves. Acoustic excitation does not influence the waiting time between two adjacent boiling bubbles. The growth times of the bubbles are, in contrast, influenced by the applied acoustic waves. This results in an increase in the bubble departure frequency, which should promote micro-convection near the heater wall.

A decrease of approximately 20 ± 3 % in bubble volume was obtained, resulting in the detachment of boiling bubbles 0.7 milliseconds faster. It can therefore be concluded that we have succeeded to promote the detachment of growing vapor bubbles on the heater wall, resulting in higher departure frequencies.

7.1.2 Excitation in first order anisotropic mode

Measurements with excitation in the first order anisotropic 'Lamb' mode are performed as well. It was concluded that bubble volumes of the same order have almost exactly the same first order anisotropic resonance frequency and errors in the determination of bubble size do not have influence. It is therefore much easier to excite the bubble in their resonance frequency. During the performed measurements, large decrease in bubble volume and growth times were observed. However, the low frequencies affected the experimental setup in such a way that the results are not convincing. Since a significant decrease in bubble volume was observed , while temperature did not changed, these results seems to be promising.

7.1.3 Heat transfer

The increase in heat transfer is investigated. We succeeded to decrease the bubble volumes with approximately 20 %. On the other hand the bubble departure frequency is increased. This results in a maximum decrease of 14 % in the energy transported by the bubbles. If the applied power is kept constant and convection is the only other heat transfer mechanism in the setup, this should result in an increase in heat transfer.

However, an order analysis showed that the maximum transported energy by the vapor bubbles is an order ten times smaller than the convective heat transfer. A decrease of 14 % in the bubble transport has only a slight effect on the total heat transfer and an increase of 2 % in the heat transfer coefficient is the maximum expected efficiency.

7.2 Future work

7.2.1 Experimental setup

Temperature fluctuations were the largest problem during the measurements. Due to the large extended reservoir and the slow temperature feedback system, oscillations in temperature of three tenths of a degree occurred. This prevented a long run with applied acoustic waves to see the effects after for example ten minutes. In future work it should be tried to minimize the heat losses to the surroundings by a better isolation or other temperature feedback system. The use of another fluid - for example HFE 7000, which has a boiling point at 34 ° Celsius - can solve the problem as well.

Measurements are performed with the stainless steel bubble generators. However, both generators showed multiple active nucleation sites after intensive use and it is recommended to replace the glue and clean the generators for future work. Moreover, thin film bubble generators (which have a constant wall temperature instead of constant heat flux) were not used in our experiments since they showed strange behavior and leakage. New fabricated thin film bubble generators are now available in the lab and it is recommended to try these generators as well. Especially since the heater wall is maintained at a constant value and the power that is transported by the vapor bubbles can be read out instantaneously in *Labview*.

During the experiments with the frequencies in the order of the first order anisotropic mode, the membrane broke and the experimental setup started to oscillate. The results looked promising and it is of interest to investigate the effects of sound on bubble departure in these resonance modes. Therefore the experimental setup needs to be adapted to prevent temperature decreases and leakage between reservoir and boiling pot.

The recorded images were analyzed by hand. This was a lot of work and quite boring as well. It is therefore recommended to write a numerical code which can do the job. At the university of technology Eindhoven, there is a hand made code called IAT, which should do the job in future work. However, this code needs more development first.

At last the pressure inside the pool boiling pot and the losses to the surroundings have to be mapped. This will probably result in a better understanding of the observed effects and possibly better results can be obtained. However it is not easy to measure the pressure inside the pool boiling pot without affecting the standing wave pressure pattern.

7.2.2 Recommendations for application

In the chapter discussion it was already mentioned that the increase in heat transfer has to be larger than the additional applied power needed for the generation of waves. In the present setup this is not the case and it has to be verified if the increase of 2 % in the heat transfer coefficient outweighs the additional power needed in other applications. If not, it is of interest to investigate the possible effects of acoustic streaming on the heat transfer enhancement.

The application of acoustic excitation in future work depends on a variety of parameters. However, to obtain the largest possible increase in heat transfer coefficient, some parameters are of more importance than other. As was discussed in the previous chapter, the number of active nucleation sites increases the heat transport with respect to the convective heat. If the number of active nucleation sites can be increased to a number of fifty, an increase of 3% the heat transfer coefficient can be obtained. However, this number of active nucleation sites is theoretical not possible if we take the maximum number of active nucleation sites equal to the reciprocal value of the projected bubble area of a single bubble. However, the higher the better. Furthermore the superheat and applied power need to be as low as possible for the highest increase in heat transfer coefficient. This will of course not result in the increase of the critical heat flux, but it might be possible to enhance the boiling curve in regions with low ΔT.

More investigation is needed but it seems that a larger decrease in bubble volume can be obtained if the bubbles are excited in the first order anisotropic mode. It is easier to determine the frequency of the applied waves and with an error of 10 % between applied frequency and theoretical predicted resonance frequency, still effect of acoustic excitation was observed. If the bubbles are excited in the volumetric mode, this with preference with high pressures, resulting in larger volume decreases. It was observed that acoustic excitation has effect during the later stage of the bubble growth, when the bubble growth is diffusion controlled. Moreover the effect of surface tension on the attachment of the bubble supports the conclusion to excite the bubbles in the diffusion controlled growth.

References

Books

[1] Brennen, C. E., 1995. *Cavitation and Bubble Dynamics*, Oxford University Press, Oxford, p.101

[2] Çengel, Y. A. and Boles, M. A., 2002. *Thermodynamics, an engineering approach*, 4th edition, McGraw-Hill Higher Education, ISBN 0-07-121688-X

[3] Cobbold, R. S. C., 2007. *Foundations of Biomedical Ultrasound*, Oxford University Press, Inc., Oxford, New York

[4] Janna, W. S. 2000. *Engineering Heat Transfer*, 2nd edition, CRC Press LLC, USA, ISBN 0-8493-2126-3

[5] Kreith, F., 2000. *The CRC Handbook of Thermal Engineering*, Jointly published with CRC Press, USA, **XXI**, ISBN 978-3-540-66349-2

[6] Lamb, H., 1932. *Hydrodynamics*, 6th edition, Cambridge University Press, Cambridge

[7] Laplace, P. S., 1806. *Méchanique céleste*, Suppl. 10th Volume

[8] Leigthon, T.G., 1994. *The acoustic bubble*, Academic Press, London, ISBN 0-12-441920-8

[9] Neer, van, P. L. M. J., 2010. *Ultrasonic Superharmonic Imaging* Optima Grafische Communicatie, Rotterdam, ISBN 978-90-8559-998-2

[10] Norton, M. P. and Karczub, D. G., 2003. *Fundamentals of noise and vibration analysis for engineers*, Cambridge University Press, second edition, ISBN 978-0-521-49913-2

[11] Pierce, A. D., 1989. *Acoustics. An introduction to its physical principles and applications*, Acoustical Society of America, New York, ISBN 0-88318-612-8

[12] Rops, C. M., 2009. *Two phase flow and phase change heat transfer in small structures*, Ipskamp Drukkers B.V., Enschede, ISBN 978-90-9024517-1

[13] Squires, G.L., 2001. *Practical physics*, volume 4, Cambridge University Press, Cambridge

Publications

[14] Aktas, M., Farouk, B. and Lin, Y., 2005. Heat transfer enhancement by acoustic streaming in an enclosure, *Journal of Heat transfer* **127** 1313-1321

[15] Apfel, R.E., 1984. Acoustic Cavitation Inception, *Ultrasonics* **22** 167-173

[16] Bar-Cohen, A., Wang, P. and Rahim, E., 2007. Thermal Management of High Heat Flux Nanoelectronic Chips, *Bremen Micrograviity sci. technol.* **XIX-3/4** 48-52, Z-Tec Publishing

[17] Bartoli, C. and Baffigi, F., 2011. Effects of ultrasonc waves on the heat transfer enhancement in subcooled boiling, *Experimental Thermal and Fluid Science* **35** 423-432. Elsevier Inc.

[18] Basu, N., Warrier, G. R. and Dhir, V. K., 2002. Onset of Nucleate Boiling and Active Nucleation Site Density During Subcooled Flow Boiling, *Journal of heat transfer* **124** 717-728

[19] Bergles, A.E, 1997. Enhancement of pool boiling, *Int. J. Refrig.* **20**(8) 545-551. Elsevier Science Ltd. and IIR

[20] Bonekamp, S. and Bier, K., 1997. Influence of ultrasound on pool boiling heat transfer to mixtures of the refrigerants R23 and R134A, *Int. J. Refrig.* **20**(8) 606-615 Elsevier Science Ltd.

[21] Boulangé-Petermann, L., Joud, J-C. and Baroux, B., 2008. Wettability parameters controlling the surface cleanability of stainless steel, *Contact angle, Wettability and Adhesion* **5** 139-151

[22] Chen, Y., 2002. Study of forces acting on a growing bubble from a smooth surface, *International Journal of heat & technology* **20** 31-40

[23] Chesters, A. K., 1978. Modes of bubble growth in the slow-formation regime of nucleate pool boiling, *Int. J. Multiphase Flow* **4** 279-302

[24] Davis, E. J. and Anderson, G. H., 1966. The incipience of nucleate boiling in forced convection flow, *AIChE J.* **12**(4) 774-780

[25] Devaud, M., Hocquet, T., Bacri, J-C. and Leroy, V., 2008. The Minnaert bubble: an acoustic approach, *Eur. J. Phys.* **29** 1263-1285

[26] Dhir, V.K., 1998. Boiling Heat Transfer, *Annu. Rev. Fluid Mech.* **30** 365-401

[27] Douglas, Z.W., Smith, M.K, and Glezer, A., 2007. Acoustically Enhanced Boiling Heat Transfer, *Therminic* 145-149, EDA Publishing

[28] Fand, R.M. and Kave, J., 1960. Acoustic Streaming near a Heated Cylinder, *The Journal of the Acoustical Society of America* **32**(5) 579-584, Massachutes Institute of Technology, Cambridge, Massachutes

[29] FAND, R.M., 1965. The influence of acoustical vibrations on heat transfer by natural convection from a horizontal cylinder to water, *Journal of Heat Transfer* **87** 309-310

[30] GELD, VAN DER, C. W. M, 2009. The dynamics of a boiling bubble before and after detachment, *Heat Mass Transfer* **45** 831-846

[31] GELD, VAN DER, C. W. M., BERG, VAN DE, R. AND PEUKERT, P., 2009. Large amplitude oscillation of a boiling bubble growing at a wall in stagnation flow, *ECI International Conference on boiling heat transfer*

[32] GELD, VAN DER, C. W. M AND KUERTEN, J. G. M., 2009. Axisymmetric dynamics of a bubble near a plane wall, *J. Fluid Mech.* **640** 265-303

[33] GELD, VAN DER, C. W. M., 2010. Shape oscillations of a boiling bubble, *Multiphase Science and Technology* **22**(2) 157-175

[34] HELDEN, W. G. H., GELD, VAN DER, C. W. M. AND BOOT, P. G. M., 1995. Forces on bubbles growing and detaching in flow along a vertical wall, *International Journal of heat and mass transfer* **38**(11) 2075-2088

[35] HSU, Y. Y., 1962. On the size range of active nucleation sites on heating surface, *Journal of heat transfer* **84** 207-216

[36] HUYGENS, C., 1678. Traité de la lumière, *published in Leyden (1690)*

[37] HYUN, S., LEE, D.-R. AND LOH, B.-G., 2005. Investigation of convective heat transfer augmentation using acoustic streaming generated by ultrasonic vibrations, *International Journal of Heat and Mass Transfer* **48** 703-718

[38] IIDA, Y. AND TSUTSUI, K., 1992. Effects of Ultrasonic Waves on Natural Convection, Nucleate Boiling, and Film Boiling Heat Transfer from a Wire to a Saturated Liquid, *Experimental Thermal and Fluid Science* **5** 108-115, Elsevier Publishing

[39] JEONG, J.H. AND KWON, Y.C., 2006. Effects of Ultrasonic Vibration on Subcooled Pool Boiling Critical Heat Flux, *Heat Mass Transfer* **42** 1155-1161, Springer-Verlag

[40] KIM, H.Y., KIM, Y.G. AND KANG, B.H., 2004. Enhancement of natural convection and pool boiling heat transfer via ultrasonic vibration, *Int. J. Heat and Mass Transfer* **47** 2831-2840

[41] KIM, Y.G., KANG, S.M., KANG, B.H. AND KIM, H.Y, 2002. Effect of ultrasonic vibration upon pool boiling heat tranfer, *Proceedings of the SAREK 2002 Summer Annual Conference, Yongpyong*

[42] LEGAY, M., GONDREXON, N., PERSON, LE, S., BOLDO, P. AND BONTEMPS, A, 2011. Enhancement of heat transfer by ultrasound: review and recent advances, *International Journal of Chemical Engineering Volume 2011*, **ID 670108**, 17 pages

[43] LI, K.W. AND PARKER, J.D., 1967. Acoustical effects on free convective heat transfer from a horizontal wire, *J. Heat Transfer* **89** 277-278

[44] LIGHTHILL, S.J., 1978. Acoustic Streaming, *Journal of Sound and Vibration* **61** 391-418

[45] LOH, B.-G., HYUN, S., RO, P.I., KLEINSTREUER, C., 2001. Acoustic streaming induced by ultrasonic flexural vibrations and associated enhancement of convective heat transfer, *J. Acoust. Soc. Am.* **111**(2) 875-883

[46] MIKIC, B. B., ROHSENOW, W. M. AND GRIFFITH, P., 1970. On bubble growth rates, *Int. J. Heat Mass Transfer* **13** 657-666

[47] MINNAERT, M., 1933. Air bubble and sound of running water, *Phil. Mag.* **6** 235-248

[48] NAKAGAWA, M., 2004. Analyses of Acoustic Streaming Generated by Four Ultrasonic Vibrators in a Vessel, *Japanese Journal of Applied Physics* **43**(5B) 2847-2851

[49] NEPPIRAS, E.A., 1984. Acoustic Cavitation: an Introduction, *Ultrasonics* **22** 25-28

[50] NOMURA, S., MURAKAMI, K. AND SASAKI, Y., 2000. Streaming induced by ultrasonic vibrations in a water vessel, *Japanese Journal of Applied Physicsz* **39** 3636-3640

[51] NOMURA, S., NAKAGAWA, M., MUKASA, S., TOYOTA, H. ,MURAKAMI, K AND KOBAYASHI, R., 2005. Ultrasonic heat transfer enhancement with obstacle in front of heating surface, *Japanese Journal of Applied Physics* **44**(6B) 4674-4677

[52] NORMURA, S., YAMAMOTO, A. AND MURAKAMI, K., 2002.Ultrasonic Heat Transfer Enhancement Using a Horn-type Transducer, *Jpn. J. Appl. Phys.* **41** 3217-3222

[53] NUKIYAMA, S., 1966. The maximum and Minimum Values of Heat Q Transmitted from Metal to Boiling Water under Atmospheric Pressure, *Int. J. Heat Mass Transfer* **9** 1419-1433

[54] NYBORG, W., 1953. Acoustic Streaming due to the attenuated plane wave, *J. Acoust. Soc. Am.* **25** 68-75

[55] PARK, K.-A. AND BERGLES, A.E., 1988. Ultrasonic Enhancement of Saturated and Subcooled Pool Boiling, *Int. J. Heat Mass Transfer* **31(3)** 664-667

[56] PLESSET, M. S., 1949. The dynamics of cavitation bubbles, *ASME J. Appl. Mech.* **16** 228-231 231.

[57] PLESSET, M. S. AND PROSPERETTI, A., 1977. Bubble dynamics and cavitation, *Ann. Rev. Fluid Mech.* **9** 145-185

[58] PLESSET, M. S. AND ZWICK, S. A., 1952. A nonsteady heat diffusion problem with spherical symmetry, *Journal of Applied Physics* **23** 95-98

[59] PLESSET, M. S. AND ZWICK, S. A., 1954. The growth of vapor bubbles in superheated liquids, *Journal of Applied Physics* **25** 493-500

[60] RAYLEIGH, LORD, 1884. On the circulation of air observed in Kundt's tubes, *Philos. Trans. R. Soc. London* **A175** 1-21

[61] RAYLEIGH, LORD, 1917. On the pressure developed in a liquid during the collapse of a spherical cavity, *Phi/us. Mag.* **34** 94-98

[62] ROHSENOW, W. M., 1971. Boiling, *Annu. Rev. Fluid Mech.* **3** 211-236

[63] Rops, C.M, Lindken, R.,Velthuis, J.F.M. and Westerweel, J., 2009. Enhanced heat transfer in confined pool boiling, *Int. J. Heat and Fluid Flow* **30** 751-760

[64] Sato, T. and Matsumara, H., 1964. On the conditions of incipient subcooled boiling with forced convection, *Bull. JSME* **7**(26) 392-398

[65] Schneider, B., Koşar, A., Kuo, C.-J., Mishra, C., Cole, G.S., Scaringe, R.P. and Peles, Y., 2006. Cavitation enhanced heat transfer in microchannels, *Journal of heat transfer* **128** 1293- 1301

[66] Shannon, C. E., 1949. Communication in the Presence of Noise. *Proceedings of the IRE* **37**(1) 10-21

[67] Vainshtein, P., Fichman, M. and Gutfinger, C., 1995. Acoustic enhancement of heat transfer between two parallel plates, *Int. J. Heat Mass Transfer* **38**(10) 1893-1899

[68] Vargaftik, N. B., Volkov, B. N. and Voljak, L. D., 1983. International Tables of the Surface Tension of Water, *Journal of Physical and Chemical Reference Data* **12**(3) 817-820

[69] Webb, R.L and Bergles, A.E, 1983. Heat transfer enhancement: second generation technology, *Mechanical Engineering* **11**(6) 60-67

[70] Westervelt, P.J., 1953. The theory of steady rotational flow generated by sound field, *J. Acoust. Soc. Am.* **25** 60-67

[71] Wong, S.W. and Chon, W.Y., 1969. Effects of Ultrasonic Vibrations on Heat Transfer to Liquids by Natural Convection and by Boiling, *AIChE J.* **15**(2) 281-288

[72] Zhou, D.W, 2005. A Novel Concept for boiling heat transfer enhancement, *Journal of Mechanical Engineering* **51**(7-8) 366-373

[73] Zhou, D.W., Liu, D.Y., Hu, X.G. and Ma, C.F, 2002. Effect of acoustic cavitation on boiling heat transfer, *Experimental Thermal and Fluid Science* **26** 931-938

[74] Zuber, N., 1961. The dynamics of vapor bubbles in nonuniform temperature fields, *International Journal of heat and mass transfer* **2**(1-2) 83-98

Reports

[75] Broek, van den, R.J. and Geld, van der, C.W.M., 2009. Bubble Generator Design Up to May 2009, *Internal report, section Process Technology*, Eindhoven University of Technology

[76] Dijk, van, R., 2009. Ontwerpen van een nieuwe testopstelling, *Bachelor Final Project, section Process Technology*, Eindhoven University of Technology

[77] Geld, van der, C. W. M., 2011. Elementary two-phase flow with heat transfer, *Lecture Notes, Master Mechanical Engineering*, Eindhoven University of Technology

[78] Gisbergen, van , B.C.J., 2011. The effect of heat flux on forces during bubble growth, *MSc. Thesis, section Process Technology*, Eindhoven University of Technology

[79] Kovačević, M., 2006. Study of a boiling bubble in uniform approaching flow at high bubble Reynolds numbers, *Ph.D. Thesis, section Process Technology*, Eindhoven University of Technology

Webpages

[80] Corradini, M. L., 1997. Pool boiling, *http://wins.engr.wisc.edu/teaching/mpfBook/node26.html*, consulted on: April 22, 2012

[81] Photron, 2012. Photron Fastcam SA3, *http://www.photron.com/index.php?cmd=product_general&product_id=6*, consulted on May 28, 2012

[82] Wikipedia, 2012. Huygens-Fresnel principle, *http://en.wikipedia.org/wiki/Huygens-Fresnel_principle*, consulted on May 21, 2012

[83] Wikipedia, 2012. Wave, *http://en.wikipedia.org/wiki/Wave*, consulted on: May 18, 2012

[84] Winterton, R., 2011. Bubble growth, Thermopedia *http://www.thermopedia.com/content/602/*, DOI:10.1615/AtoZ.b.bubble_growth, consulted on June 4, 2012

Appendix A

Literature study: Heat transfer enhancement by (ultra)sonic excitation

A.1 Ultrasonic excitation

Fand (1965) [29] and Li and Parker (1967) [43] were one of the first researchers who found enhancement of the heat transfer by sonic vibration. Experiments with ultrasonic vibration were carried out by Wong and Chon [71] in 1969, who investigated the effects on the heat transfer of subcooled water and methanol in both the natural convection -and pool boiling regime. They found heat transfer enhancement due to turbulent oscillating cavitation bubbles on the heating surface. In 1992 Iida and Tsutsui[38] repeated the experiments of Wong and Chon with saturated ethyl alcohol and extended their study with the effects of ultrasonic vibrations on the heat transfer in the film boiling regime.

Both studies obtained a noticeable augmentation in the natural convection -and film boiling regime, whereas almost no enhancement of the heat transfer in nucleate boiling regime was observed. It is reported that the main mechanisms leading to heat transfer enhancement in natural convection and in subcooled boiling are acoustic streaming and cavitation, though the later may only become dominant when the applied power is high enough to cause it [38].

Kim *et.al.* [40] (2004) used a heated platinum wire in the liquid FC-72 for their measurements. Like Wong and Chon [71], they address the strong enhancement obtained by ultrasound in the natural convection regime to the presence of cavitation bubbles, which promote micro-convection and turbulent oscillations in the fluid. Kim *et.al.* [40] argue that the enhancing effect of cavitation bubbles is not as significant in the nucleate boiling regime as in the convection regime.

Park and Bergles (1988) [55] obtained an enhancing effect by ultrasonic excitation in their experiments using the dielectric liquid R-113 in pool boiling. The refrigerant R-113 is used as a cooling fluid for micro-electronic devices. They reported that the critical heat fluxes for subcooled conditions were slightly increased by the application of ultrasound. This was confirmed by the experiments of Bartoli and Baffigi (2011) [17] who found that the most important variable for heat transfer enhancement is undoubtedly the subcooling. Zhou (2005) [72] argued that the increase in subcooling leads to a decrease in the thickness of the thermal boundary layer, resulting in augmentation of the heat transfer.

Bonekamp and Bier (1997) [20] compared the augmentation of heat transfer of mixtures of the refrigerants R23 and R134a with pure substances in pool boiling. For their study a horizontal brass tube exposed to ultrasonic waves of different frequencies was used and the heat transfer is measured in a wide range of normalized saturation pressures and heat fluxes. Bonekamp and Bier found that the heat transfer is more pronounced for mixtures than for pure substances. This is mainly caused by a decrease of the local saturation temperature near the heating wall, due to a better mixing in the liquid boundary [20].

More recent studies

Douglas *et.al.* (2007) [27] carried out an experimental research on the augmentation of the boiling heat transfer of a single vapor bubble in the vicinity of a rigid-heated wall. They produced a novel heater to generate a single bubble of prescribed size and prescribed location on a flat heated surface. It was found that ultrasound can lead to unstable waves on the interface of the bubble with the heater, which are violent enough to detach the bubble from its surface. By influencing the detachment of bubbles, Douglas *et.al.* succeeded to increase the critical heat flux.

Jeong and Kwon (2006) [39] investigated the effects on the critical heat flux of subcooled water exposed to ultrasonic waves under different inclination angles. They used a flat heater mounted onto a specimen, which was able to rotate 180 degrees. It was found that the augmentation of the CHF is closely related to the process of bubble generation and the departure of it, which is confirmed by Douglas *et.al.* [27]. Jeong and Kwon observed that the generation of large vapor bubbles is suppressed by applying ultrasound. It is speculated that fluid mixing due to acoustic streaming and cavitation causes this phenomenon [39]. The cavitation intensity increases for higher subcooling, leading to a further enhancement of the heat transfer. This observation was previously reported by Kim *et.al.* (2002) [41].

Many more publications regarding the heat transfer enhancement using ultrasound were found. The publication of Legay *et.al.* (2011) [42] reviews the most important ultrasonic enhancement techniques and discusses the most recent advances. It shows the applicability of ultrasound in a lot of different research areas.

A.2 Ultrasonic enhancing effects

The previously discussed publications point out that the application of ultrasound can enhance the heat transfer. The main phenomena causing this enhancement were referred to as acoustic streaming and/or cavitation. Unfortunately, in some of the studies it is not clear which effect is causing the enhancement of the heat transfer, since both phenomena are not taken into account separately. In this section we separate both enhancing phenomena and discuss them one by one briefly.

A.2.1 Acoustic streaming

The effect of acoustic streaming was already observed around 1930 in experiments with standing waves and tobacco smoke, where a vortex motion with four loops was observed around a cylinder [28]. During the last decades the effect is more theoretical analyzed and some nice experiments have been performed.

Theory

The first attempts to find theoretical solutions to the acoustic streaming phenomenon started with the work of Rayleigh [60] in 1884. The starting point of his analysis was the vortex flow, which occurs when a longitudinal standing wave is formed in a long pipe (Kundt's tube). His theoretical work was continued in 1953 by among others Westervelt [70] and Nyborg [54].

A well-known mathematical description of acoustic streaming, based on the previous works of Westervelt and Nyborg, was published by Lighthill [44] in 1978. He reported that exclusively dissipation of the acoustic energy flux permits gradients in the momentum flux to force acoustic streaming motions [44]. In other words: the dissipated momentum of a sound wave traveling through a viscous liquid induces motion in the direction of wave propagation.

Experiments

In 1959 Fand and Kave [28] were the first researchers who investigated acoustic streaming exposed to a temperature gradient. For their experiment an electrically heated cylinder was placed in air perpendicular to the vibrating surface. Fand and Kave [28] reported that thermoacoustic streaming is a much stronger flow phenomenon than isothermal streaming and it can have important applications in the field of heat transfer.

Vainshtein *et.al.* [67] considered in 1994 a problem in which a steady state sonic wave is propagating in longitudinal direction between two parallel plates. Both plates are kept at different temperatures and the gap between both plates is much smaller than the wavelength of the propagating wave. Vainshtein *et.al.* found a heat transfer enhancement due to Rayleigh's vortical acoustic streaming.

Loh *et.al* (2001) [45] and later Hyun *et.al.* (2005) [37] performed experimental studies showing very nicely acoustic streaming with corresponding heat transfer enhancement. They created an acoustic streaming in the air gap above a resonating aluminum beam and visualized it by spraying acetone onto the vibrating beam [45]. The streaming velocity is calculated from the rotational speed of small objects which are levitated above the velocity antinodes and stay at the midpoint of the gap. To measure the enhancement of convective heat transfer due to the acoustic streaming, they placed a heat source above the vibrating aluminum beam and measured the temperature changes of the heater. For both studies it is reported that flow entrainment enhances the flow speed and changes the flow pattern, which will result in an enhancement of the heat transfer [45].

In the last decades, somewhat similar enhancing experiments with acoustic streaming have been done. For more studies on this topic, the interested reader is referred to Legay *et.al.* (2011) [42] or the literature [48], [14] and [52].

A.2.2 Acoustic cavitation

From the discussed literature, cavitation is assumed to be the major effect of heat transfer enhancement by ultrasound. However, there are not many investigations considering the effect of acoustic cavitation alone.

Theory

Cavitation is a physical phenomenon in liquids where vapor or air pockets are formed as a result of local pressure reduction below a critical value [65]. When cavitation is induced by an oscillating pressure field it is referred to as acoustic cavitation [15], [49]. During the rarefaction phase of the applied ultrasonic wave, the local pressure can be decreased sufficiently below the critical pressure and vapor bubbles are formed. The induced vapor bubbles start oscillating and will finally collapse violently due to the compression phase of the sound wave [50], [71]. The collapsing of cavitation bubbles near the solid-liquid interface disrupts thermal and velocity boundary layers, reducing the thermal resistance and creating a micro-turbulence in the boundary layer [42]. Among others Kim *et.al.* [40] concluded that this phenomenon significantly enhances heat transfer in the natural convection regime.

Experiments

Zhou *et.al.* (2002) [73] and later Zhou (2005) [72] investigated the effects of acoustic cavitation on the boiling heat transfer on a horizontal copper cylinder. It was reported that cavitation bubbles have an important influence on the nucleation, growth and collapse of vapor embryos within cavities on the heater. Furthermore they found that cavitation can activate residual gas located in cavities on the heater surface. Zhou *et.al.* (2002) proved that the boiling heat transfer is enhanced notably when the intensity of the acoustic source exceeds a certain value [73]. It is reported by Zhou (2005) that acoustic cavitation eliminates hysteresis as well.

Although a lot of researchers assign acoustic cavitation as the main mechanism of heat transfer enhancement, more publications considering acoustic cavitation alone were not found. It shows that the principle of acoustic cavitation is known, but it is hard to separate the enhancing effects of cavitation from the enhancing effects of acoustic streaming completely.

Appendix B

Ultrasound in Megahertz range

The pressure fields of the simulations with applied frequency 70 Hz and 2 Mhz are presented. The 70 Hz case shows great resemblance with the case of 4 kHz as was already presented in section 3.5. The pressure field corresponding to acoustic excitation with 2 Mhz is more complex. Furthermore, some practical ultrasonic issues are discussed in this appendix as well.

B.1 Simulations with applied frequency $\nu = 70$ Hz

The pressure field resulting from excitation with a frequency of 70 Hz is given in figure B.1. The pressure field is almost identical to the one presented in figure 3.7. The same holds for the lateral -and axial beam profiles. Therefore, these profiles are not presented here again. The conclusion can be drawn for the present work that due to the large wavelengths with respect to transducer pitch size, no diffraction occurs and the bubble generator is located in the far field of the sound source.

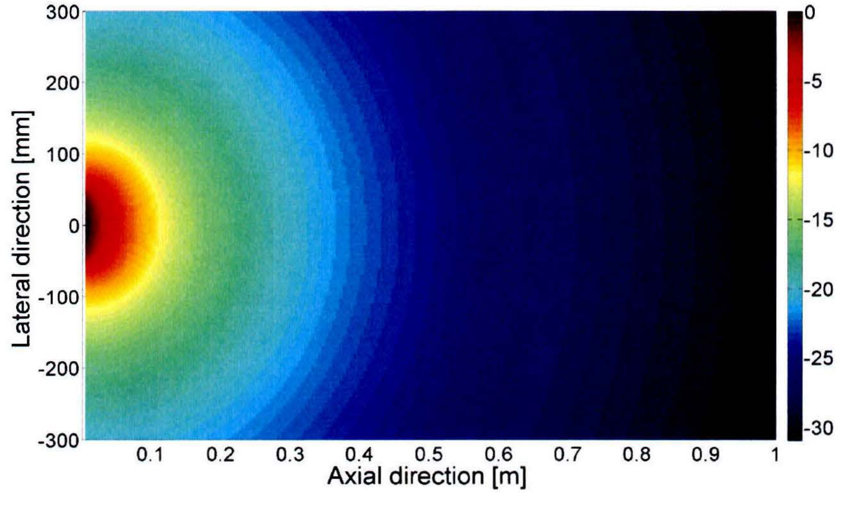

Figure B.1: Topview of the pressure field radiated from a 100 cm^2 rectangular aperture oscillating at a frequency of $\nu = 70$ Hz.

B.2 Simulations with applied frequency $\nu = 2$ MHz

In this section we present the acoustic pressure field induced by ultrasonic waves with frequency of 2 Mhz. We start by illustrating the effect of undersampling, which will lead to grating lobes. Subsequently, we adapt the transducer size to eliminate the unwanted grating lobes and investigate the generated pressure fields.

B.2.1 Grating lobes

Consider the previously used rectangular aperture of 100 cm^2 consisting of an array of 30 x 30 elements. In the case the aperture oscillates at a frequency of 2 MHz - which is physical not realistic, but can be done in the simulation - the individual pitch sizes are much larger than half a wavelength and the Nyquist sampling criterion can not be satisfied. Figure B.2 shows the theoretical generated pressure field using the rectangular aperture of 100 cm^2 where grating lobes occur.

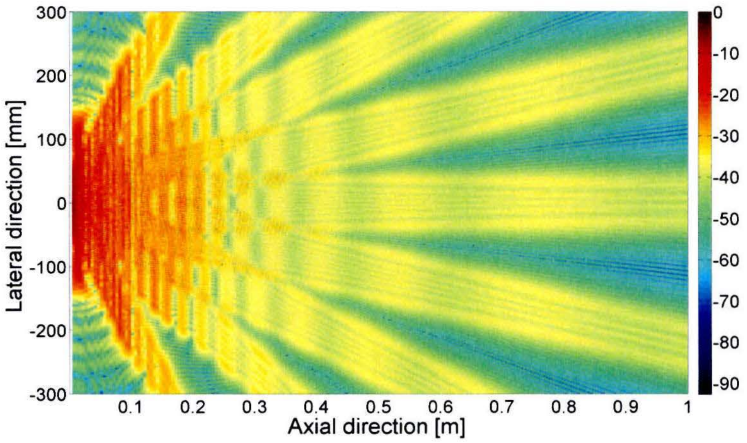

Figure B.2: Different grating lobes as a result of undersampling. To eliminate the unwanted grating lobes, the element size needs to be smaller than half a wavelength.

B.2.2 Simulations with aperture of 1 cm^2

To satisfy the sampling criterion of Nyquist, the transducer size needs to be reduced. Simulations with a rectangular aperture of 1 cm^2 oscillating at a frequency of 2 MHz are performed. The aperture has an array of 30 x 30 elements. The medium is water, which has a speed of sound of 1450 m/s. It follows for the wavelengths

$$\lambda = \frac{c}{\nu} = \frac{1450}{2 \cdot 10^6} = 0.73 \quad [\text{mm}]$$

whereas the distance between two adjacent elements is now equal to $0.01/30 = 0.33$ millimeter. In this case the pitch is smaller than half a wavelength of the applied wave and therefore fulfills the requirement of Nyquist. Grating lobes can not occur. Since the order of the wavelengths is equal to the order of the element size, diffraction and side lobes are expected to occur. This will be investigated by the lateral beam profiles.

B.2.3 Lateral beam profiles

Three different lateral beam profiles are given in figure B.5. The first beam profile corresponds to an axial position in the near field, the second lateral beam profile is calculated in the focus point and the third profile corresponds to an axial position in the far field.

The pressure distribution at axial position y = 0.001 [m] located very close to the radiating aperture shows one main lobe with magnitude of almost 0 dB and with a width of 10 millimeters. The width of the main lobe corresponds to the width of the radiating aperture and it can be concluded that at axial positions very close to the aperture, the pressure is localized around the vibrating surface. Almost no side lobes occur. The two small side lobes with pressures of -25 dB relative to the main lobe are an effect of the assumption of point-sources in the MATLAB code.

At the axial position near the focus point y = 0.04 [m] a very thin main lobe occurs and the lobe has a maximum at the centerline of the radiating aperture. At this axial position, side lobes occur and there is wave diffraction. The first real side lobe is located at approximately 7 millimeters out of the centerline and has a relative pressure of -15 dB with respect to the main lobe. The magnitude of the side lobes is decreasing relatively fast for increasing lateral position.

The pressure distribution in the far field is given in figure B.5(c). It can be observed that the side lobes are wider and the pressure is more smoothened throughout the far field of the sound source.

B.2.4 Axial beam profiles

The profile of the pressure distribution at a specific lateral position, for example at the center line, can be visualized with use of an axial beam profile. In these profiles it is very easy to observe the location of the near field, the focus point and the far field (see figure B.3).

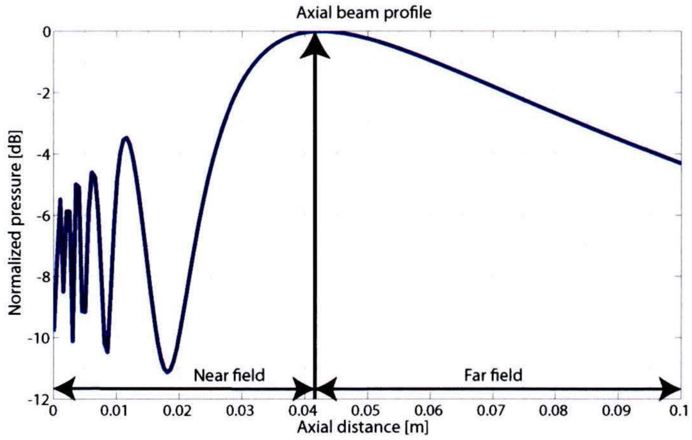

Figure B.3: Axial beam profile calculated at the centerline. The maximum in magnitude (black vertical arrow) corresponds to the axial location of the focus point. The near -and far field are indicated in the figure.

The magnitude of the pressure fluctuates in the near field, whereas the magnitude is at maximum in the focus point. At increasing axial distance from the focus point, we see a decrease in the magnitude (as was expected).

B.2.5 Acoustic sound field

Figure B.4 shows the acoustic pressure field resulting from a 1 cm^2 rectangular aperture oscillating at a frequency of ν = 2Mhz. In figure B.4(a) the pressures are normalized with respect to the maximum value of the pressure, whereas the pressures in figure B.4(b) are normalized in a decibel scale, where the reference value is the maximum magnitude of pressure.

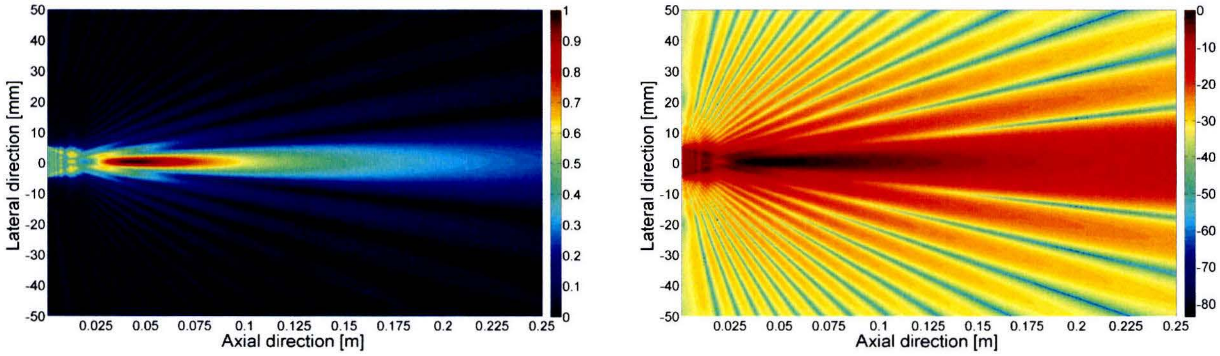

(a) Topview of normalized radiated pressure field

(b) Topview of radiated pressure field in dB

Figure B.4: Pressure field from a 1 cm^2 rectangular aperture oscillating at a frequency of ν = 2Mhz

The maximum magnitude of pressure occurs in the focus point, which is located at the center line and approximately 0.04 meters in axial direction (as follows from the figures B.5, B.3 and B.4). The wave diffraction throughout the complete domain can nicely be observed in this way.

B.3 Application of ultrasound

In the presented theory it was assumed that all individual sound sources are radiating in phase with the same amplitude from a flat surface. In practice however, this has not to be true and effects as steering or the converging of the focus point are sometimes very useful. To gain more insight in the practical issues, we start with the principles of a transducer.

B.3.1 Transducer

A transducer is a device which converts one form of energy to another, *i.e* electrical energy into motion and vice versa. Any device that is converting energy can be thought of as a transducer, however the term transducer is generally used for a sensor or detector. Transducers used to generate ultrasound are made of piezo-electric material. The piezo-electric material consists of crystals which accumulate a charge as a response to applied stress. The other way around holds as well: an applied charge results in deformation (expansion or contraction) of

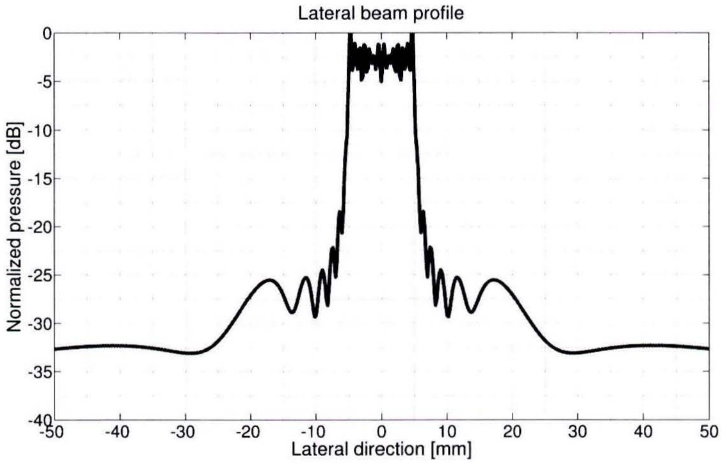

(a) Lateral beam profile in near-field at axial direction $y = 0.001$ m

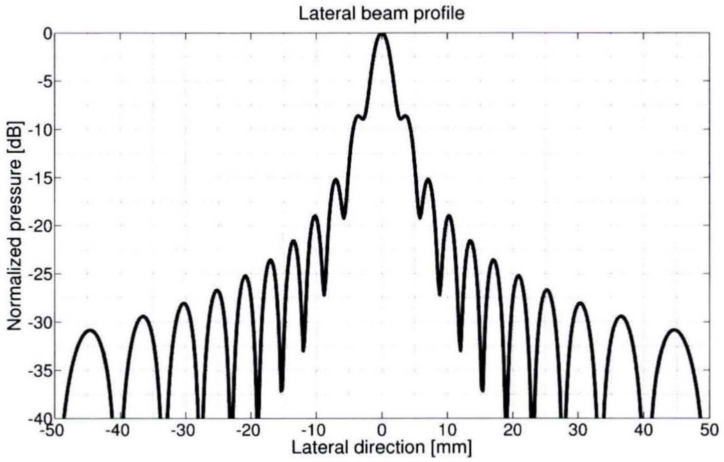

(b) Lateral beam profile in focus point at axial direction $y = 0.04$ m

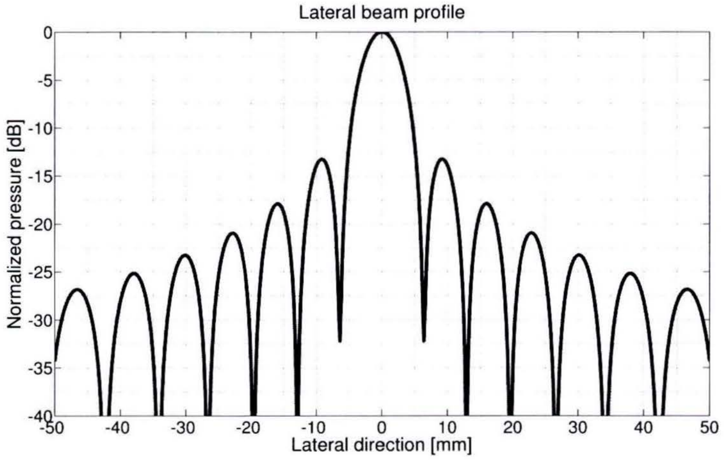

(c) Lateral beam profile in far-field at axial direction $y = 0.09$ m

Figure B.5: Lateral beam profiles at different axial positions. The pressure is normalized in dB with the maximum magnitude at the corresponding axial position.

the material. It is therefore that transducers are widely used as generators and detectors of ultrasonic signals.

The transducer has one specific frequency -or a bandwidth of frequencies- to which the transducer is sensitive. These bandwidths correspond to the resonance frequencies of the piezo-electric material. Small elements of the piezo-electric material are glued in arrays on top of an absorbing backing and mounted in a holder. The elements can be controlled individually.

B.3.2 Steering

Consider a situation in which it is desired to control the angle of the beam. Due to the individual elements of piezo-electric material on the transducer this can easily be done by controlling the charge applied on each element, *i.e* a delay in the applied electrical current for two adjacent elements results in a phase difference. The pressure field where the main beam is steered under an angle of 15 degrees is simulated and given in figure B.6(a). The concept of controlling the charge on each element is sketched in figure B.6(c). Note that if one wants to steer to the left, the time delay of the electronic signal has to increase for each adjacent piezo-electric element to the left (so the most right element of the transducer receives the signal as first). The side lobes in lateral direction are given in figure B.6(e) for the case of steering and no steering. It is obvious that the pressure profile in lateral direction changes due to the induced phase difference of the steered elements.

B.3.3 Focussing

The pressure field resulting from multiple sound sources consists of a near-field and a far-field, which are separated by the focus point. The position of the focus point is determined by a lot of parameters, *i.e.* think of the medium, the frequency, the surface of the transducer or even the alignment of the individual vibrating piezo-electric elements.

The focus point can be displaced by converging or diverging the radiated waves, which can be done with lenses or with an adjustment in the timing of the electrical charge (see figure B.6(d)). The pressure field for a focussed beam is shown in figure B.6(b). It can be observed that the location of the focus point has moved in decreasing axial direction. Moreover, the magnitude of the pressure fluctuations in the far-field has decreased significant in comparison with the unfocussed situation and at the axial position 0.25 meter, almost no sound is observed. The decrease in the radiated pressure for a focussed beam in axial direction is visualized with the axial beam plot in figure B.6(f).

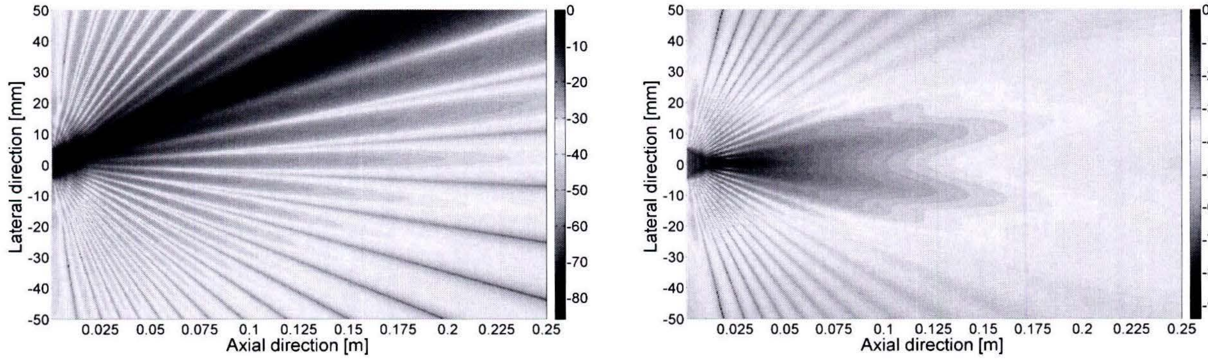

(a) Topview of steered beam under an angle of 15 degrees

(b) Topview of focussed beam

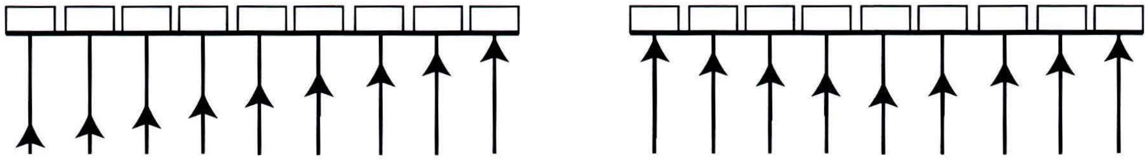

(c) Sketch of electric scheme for steering to the left

(d) Sketch of electric scheme for focussing

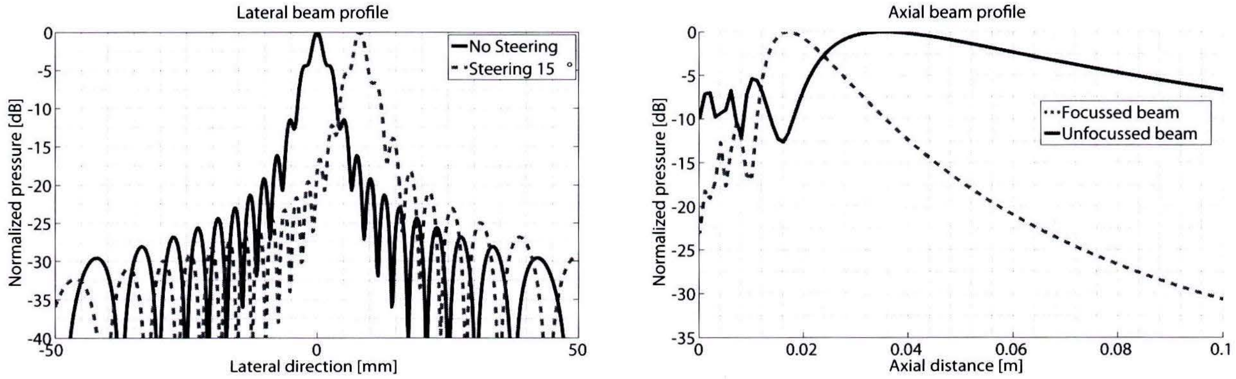

(e) Difference in lateral pressure profile for steering and no-steering

(f) Difference in axial pressure profile for focussed and unfocussed beam

Figure B.6: Figure illustrating the concepts of steering and focussing as often used in ultrasound.

Appendix C

Qsound measurement

We measured the temperature of the bulk as function of time. This was done to investigate the additional generated heat by the speaker. It was found that the temperature in the almost saturated bulk fluctuated more than three tenths of a degree during the measured twenty minutes and convincing conclusions could not be drawn.

The temperature of the bulk at approximately 99.2°Celsius as function of time is given in figure C.1. The observed fluctuations are a fact of the relative slow temperature feedback system: the silicon heating elements are turned off as long as the temperature is equal to - or above - the desired bulk temperature, whereas the heaters switch on as long as the bulk is below the desired value. Reaching the desired temperature switches the heating elements off again. Nevertheless, an overshoot of one tenth of a degree can occur easily.

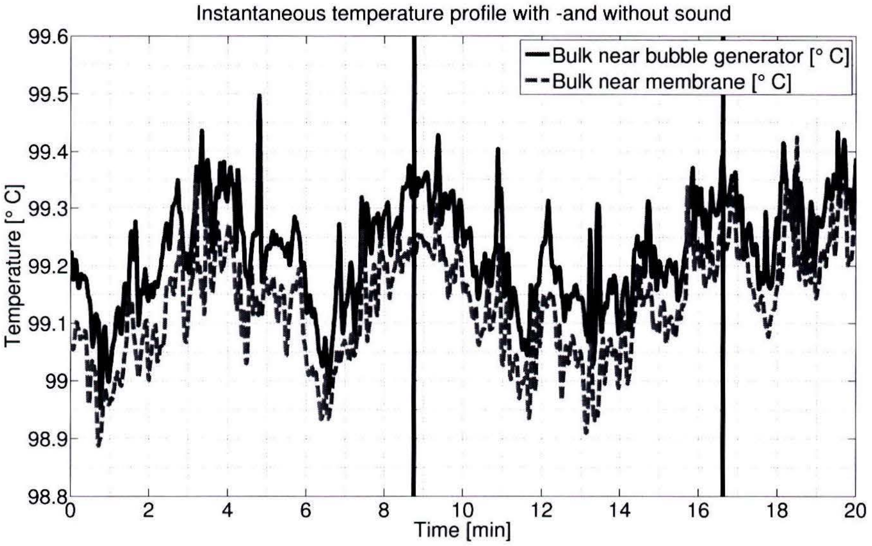

Figure C.1: Bulk temperature at $T_{\text{bulk}} \approx 92.2$°Celsius. Between the black vertical lines the sound was turned on. The fluctuating temperature is a result of the slow temperature feedback system.

It seems that the fluctuating temperature in the period with sound in figure C.1 is a result of the slow temperature feedback system rather than a consequence of the sound wave, since the same type of oscillation occurred earlier in time as well. Moreover, no additional heat of the transducer can be observed in this temperature profile. Together with the performed measurements in section 4.6.3 we conclude that the additional generated heat of the speaker can be neglected.

Appendix D

Temperature registration

D.1 Volumetric measurements using SSBG1

The small increase in bubble volume before the trigger in measurement number 4 with applied frequency of 2800 might be an error based on pixel determination, restricted resolution or a small change in temperature. Figure D.1 shows the registration of the superheat during the measurement and it can be observed that a small increase in superheat temperature occurs. This increase occurs at 1 second after the trigger, however the internal thermocouple has a delay of several seconds [78]. Therefore, the increase in superheat may be the reason for the increase in bubble volume before the trigger.

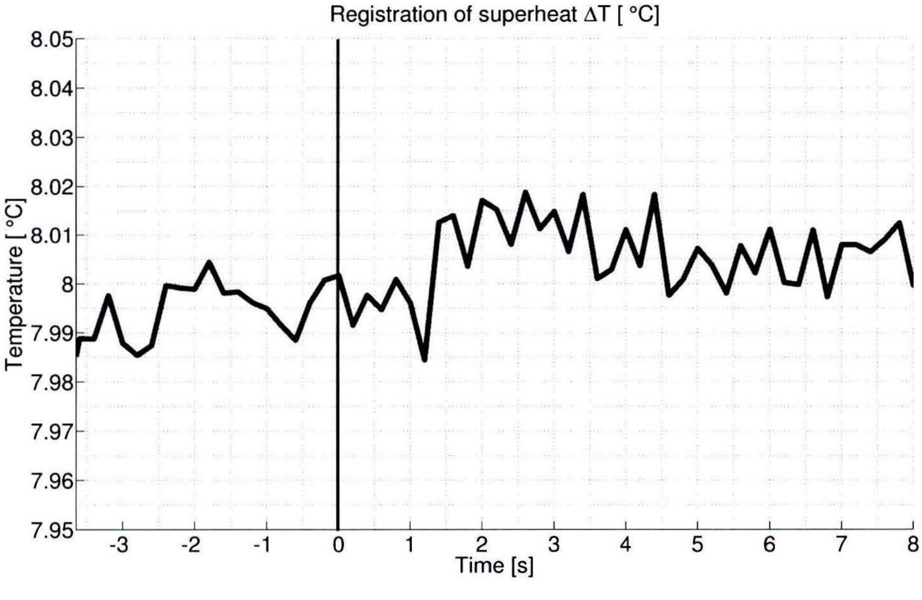

Figure D.1: Registration of superheat ΔT during the recordings with applied acoustic waves of frequency 2800 Hz.

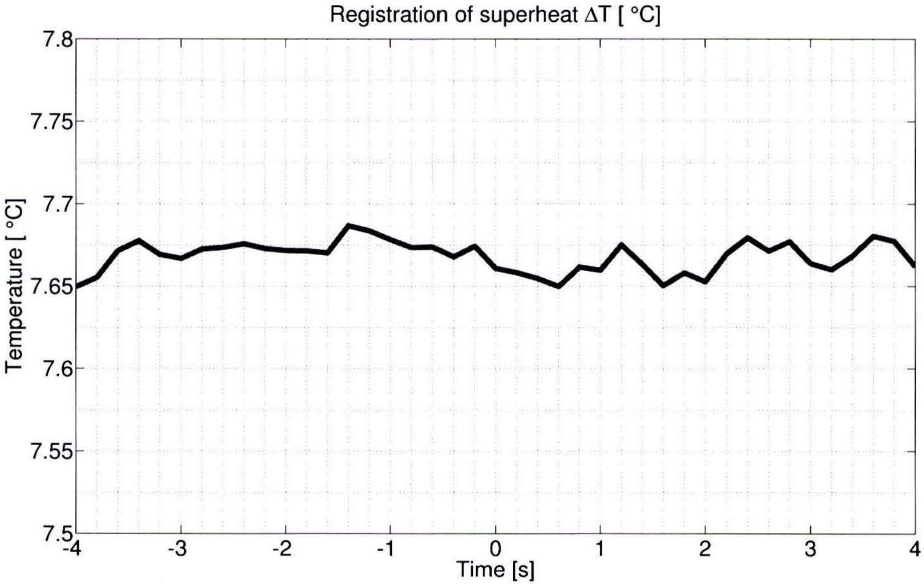

Figure D.2: Registration of superheat ΔT during the recordings with applied acoustic waves of frequency 2700 Hz. No change in the superheat occurs after the trigger. The decrease in bubble volume should therefore be a result of the applied acoustic waves.

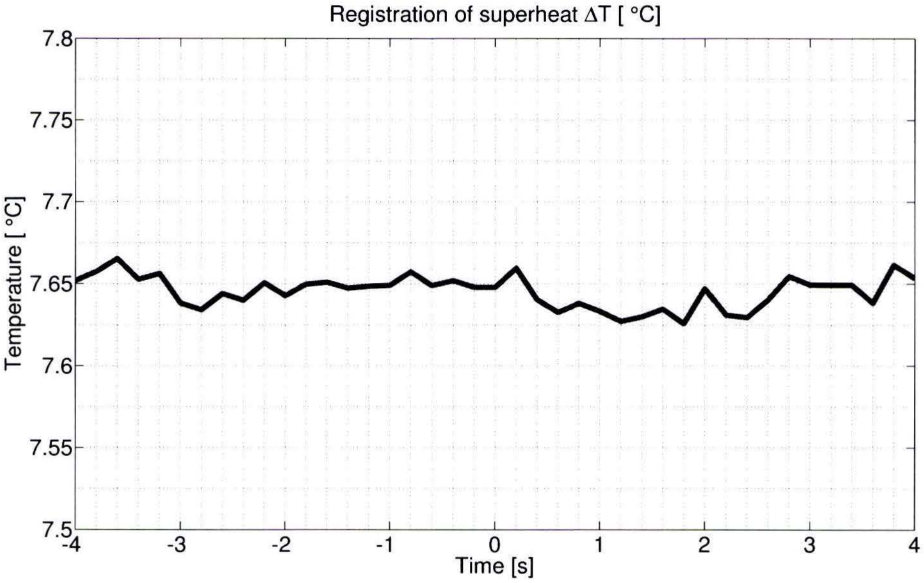

Figure D.3: Registration of superheat ΔT during the recordings with applied acoustic waves of frequency 2750 Hz. No change in the superheat occurs after the trigger. The decrease in bubble volume should therefore be a result of the applied acoustic waves.

D.2 Volumetric measurements using SSBG2

The temperature registrations of the measurements with applied frequency of 3200 Hz, 4200 Hz and 4000 Hz are presented here. The temperature profiles can be used to explain sudden changes in volume which are not an effect of acoustic waves.

Figure D.4 shows that the temperature near the heater wall increases, which is probably the explanation for the increase in bubble volume as is observed in the corresponding measurement with applied frequency 3200 Hz (presented in appendix E).

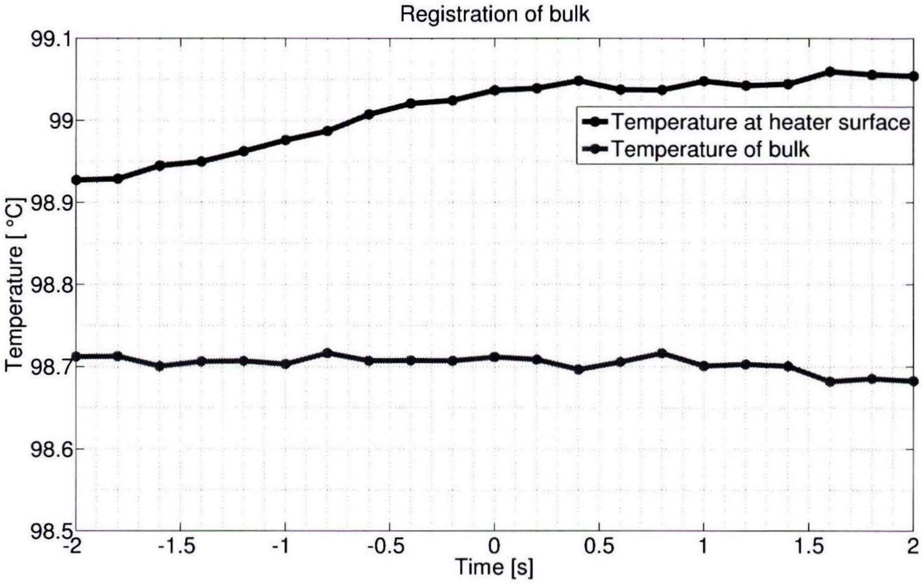

Figure D.4: Bulk temperature near heater and at center of boiling pot. Note the increase in temperature which causes the increase in bubble volume for the measurement with applied acoustic waves with frequency 3200 Hz

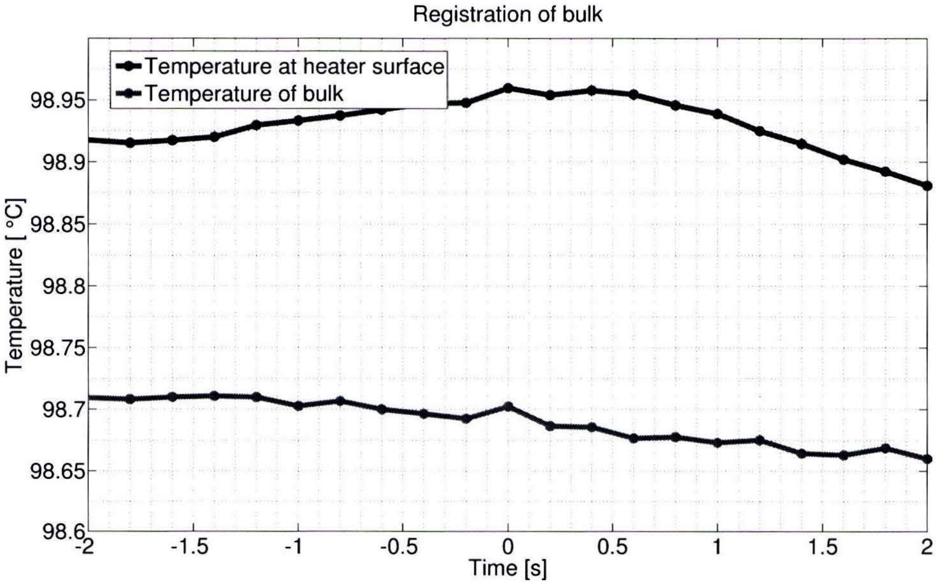

Figure D.5: Bulk temperature near heater and at center of boiling pot (4200 Hz).

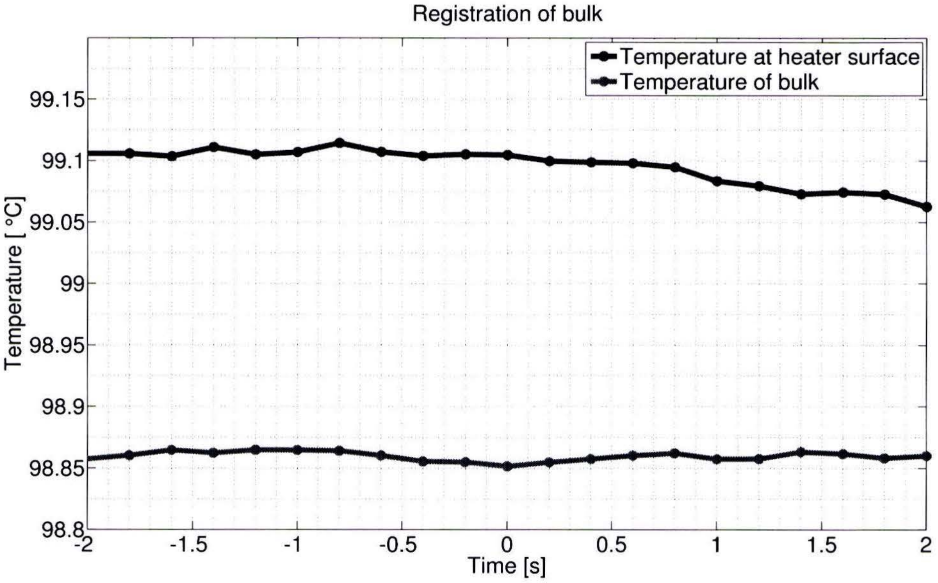

Figure D.6: Bulk temperature near heater and at center of boiling pot (4400 Hz).

Appendix E

Extra measurements performed with SSBG2

The three remaining measurements performed with the SSBG2 are presented in this appendix. The experiments are performed with a large difference between applied frequency and theoretical predicted frequency. No effect of the acoustic waves on bubble volume can be observed. The increases in bubble volume are all located between the error bars corresponding to 3 %. The increase in bubble volume of measurement number one (3200 Hz) can be explained by an increase in bulk temperature near the heater (see figure D.4). The data of the three measurements was already presented in section 5.3.2.

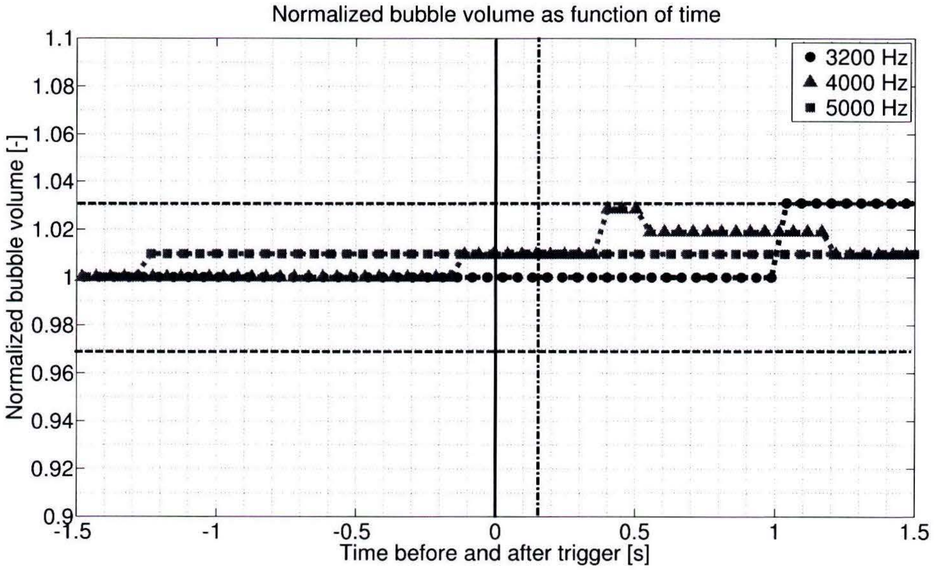

Figure E.1: Normalized bubble volume before and after the trigger. The three measurements all have large $\Delta\nu$ and no difference in volume as consequence of acoustic excitation can be observed.

Appendix F

Technical drawings of bubble generators

F.1 Thin Film Bubble Generator

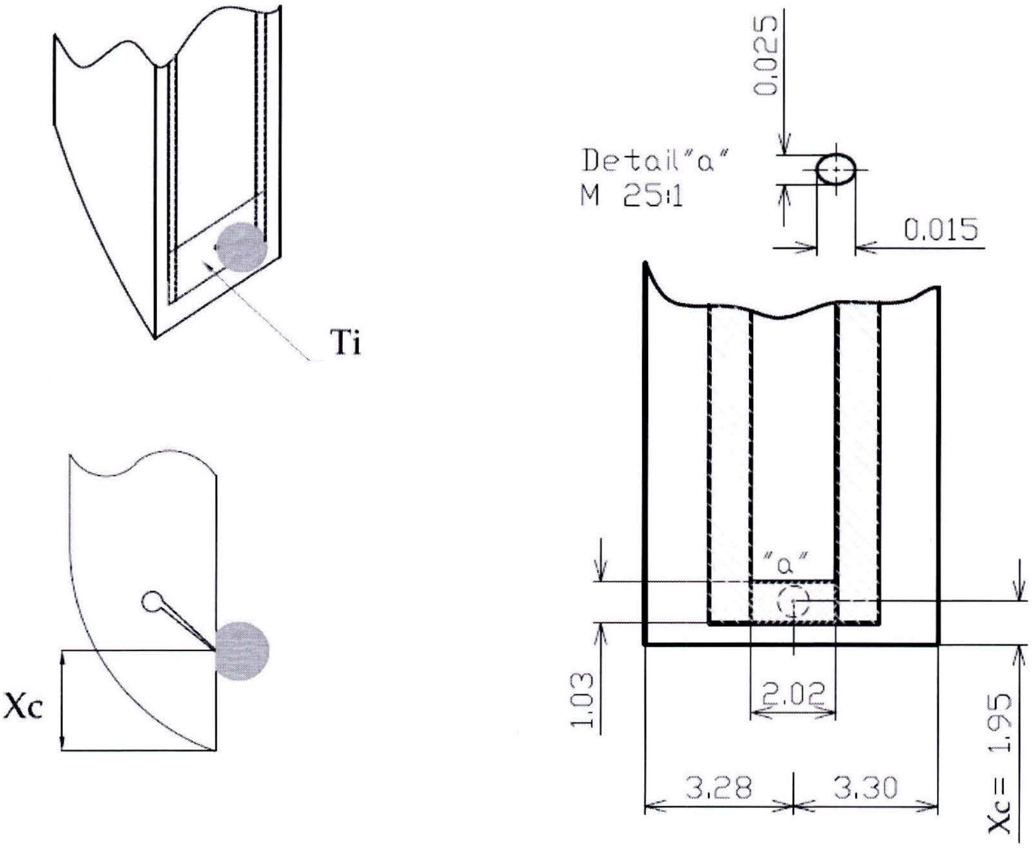

Figure F.1: Technical drawing of the thin titanium film bubble generator. In the top left corner a 3D drawing of the tip of the TFBG. In the bottom left corner a side view. The grey spot represents a vapor bubble. On the right of the figure a top view of the TFBG with corresponding dimensions in millimeters (*From "The effect of heat flux on forces during bubble growth"*, 2011. B.C.J. van Gisbergen [78])

F.2 Stainless Steel Bubble Generator

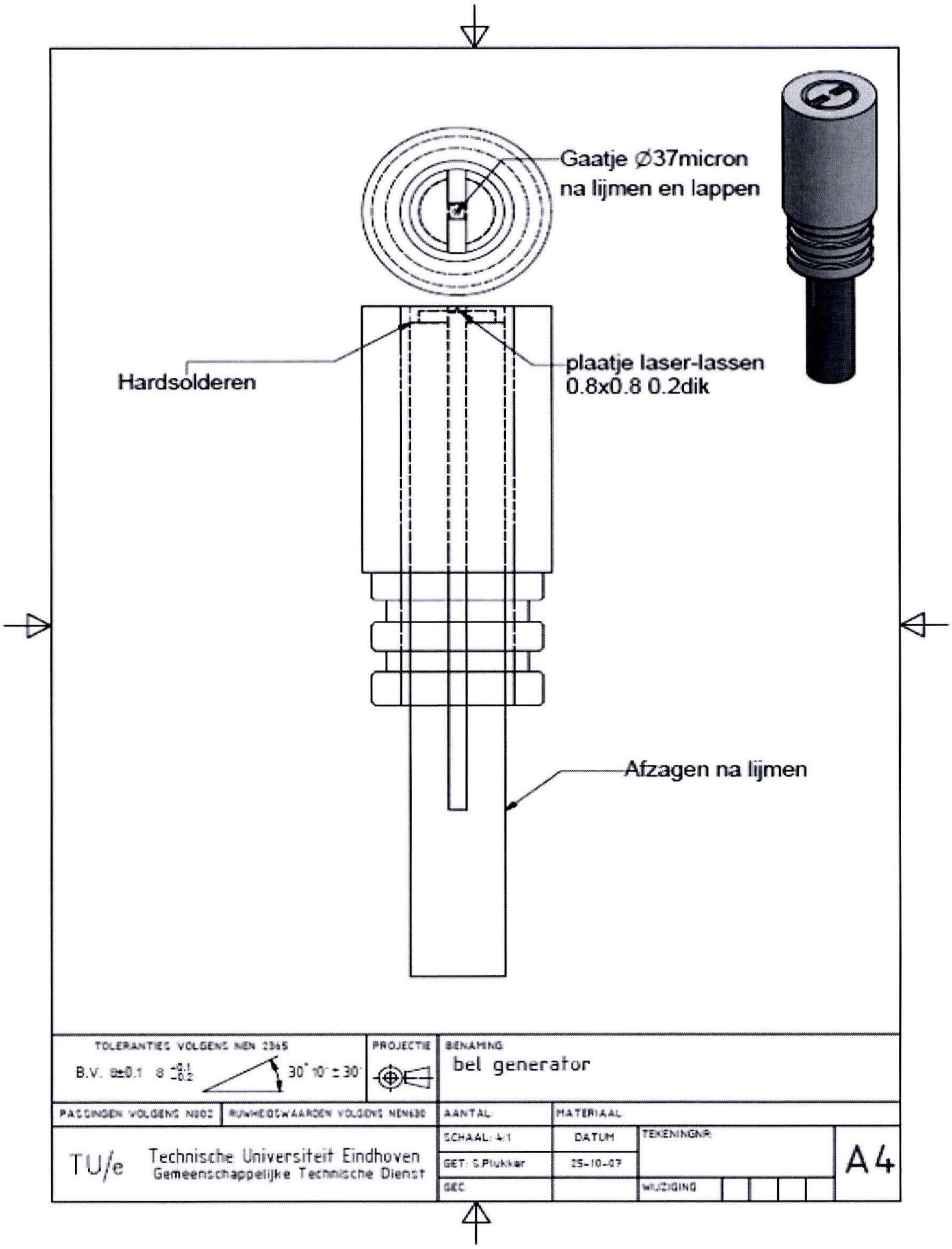

Figure F.2: Technical drawing of the stainless steel bubble generator (overview) (*From "Bubble generator design up to May 2009"*, 2009. R. J. van de Broek [75])

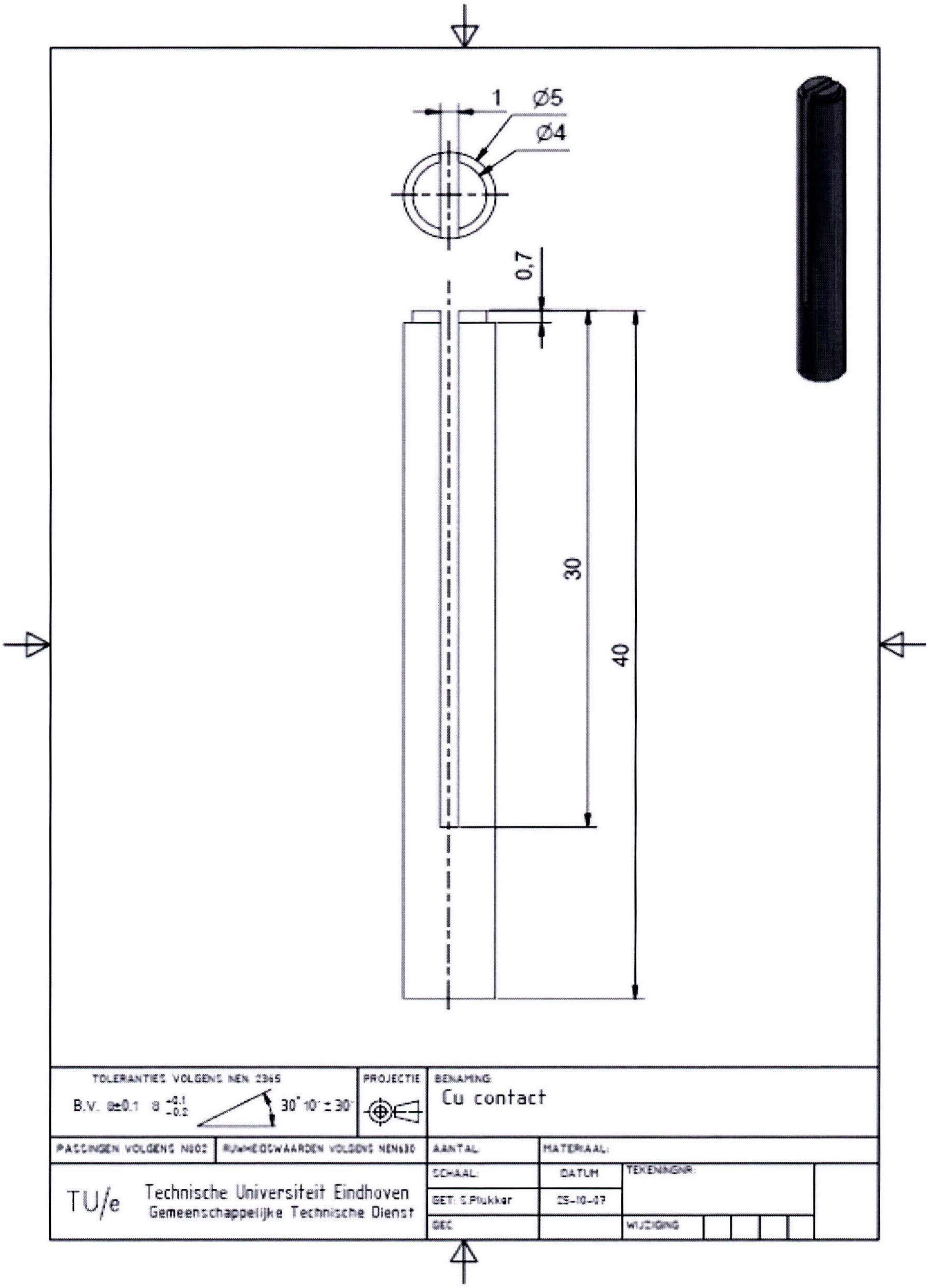

Figure F.3: Technical drawing of the stainless steel bubble generator (copper internal core) (*From "Bubble generator design up to May 2009"*, 2009. R. J. van de Broek [75])

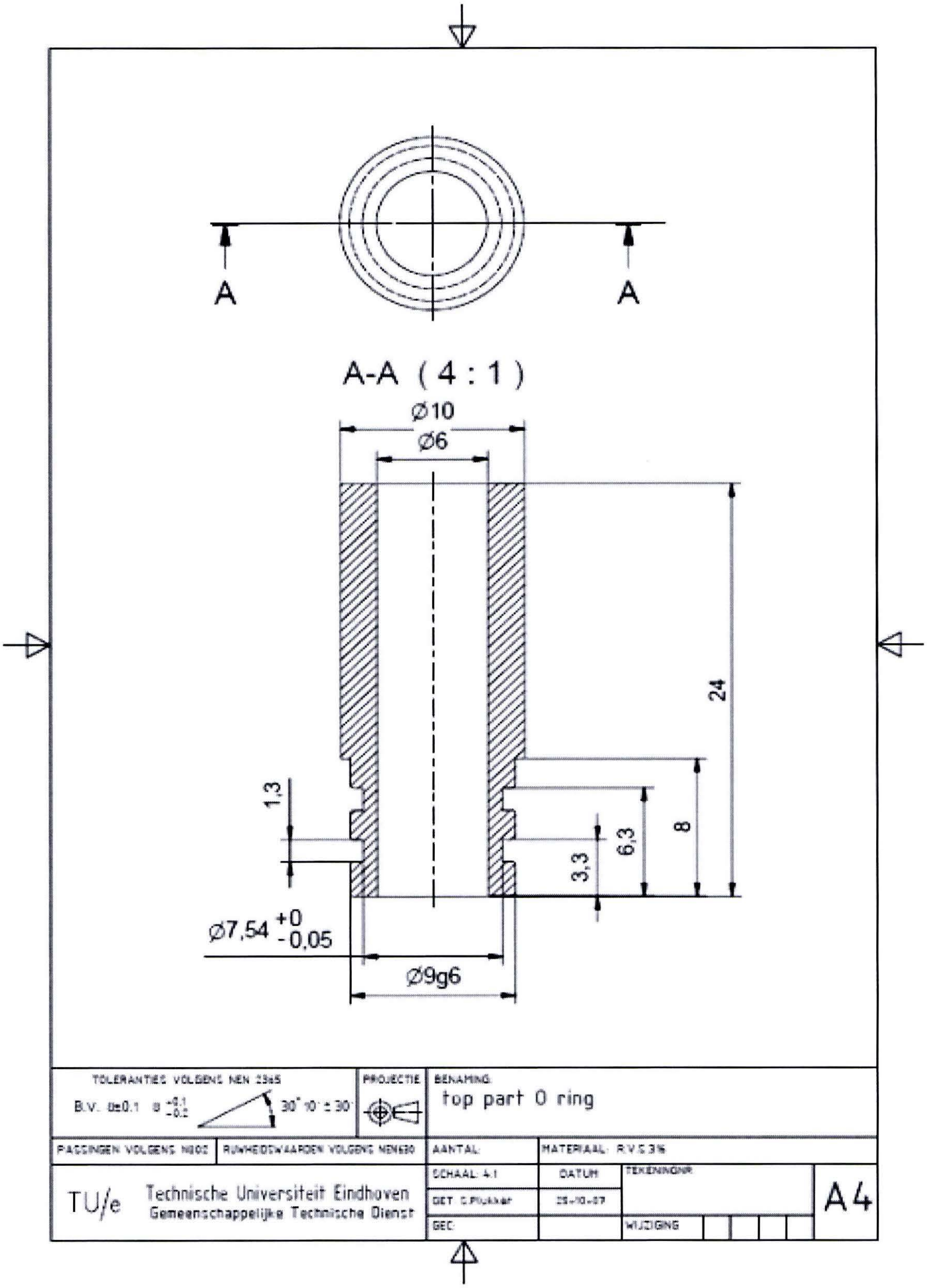

Figure F.4: Technical drawing of the stainless steel bubble generator (holder) (*From "Bubble generator design up to May 2009"*, 2009. R. J. van de Broek [75])

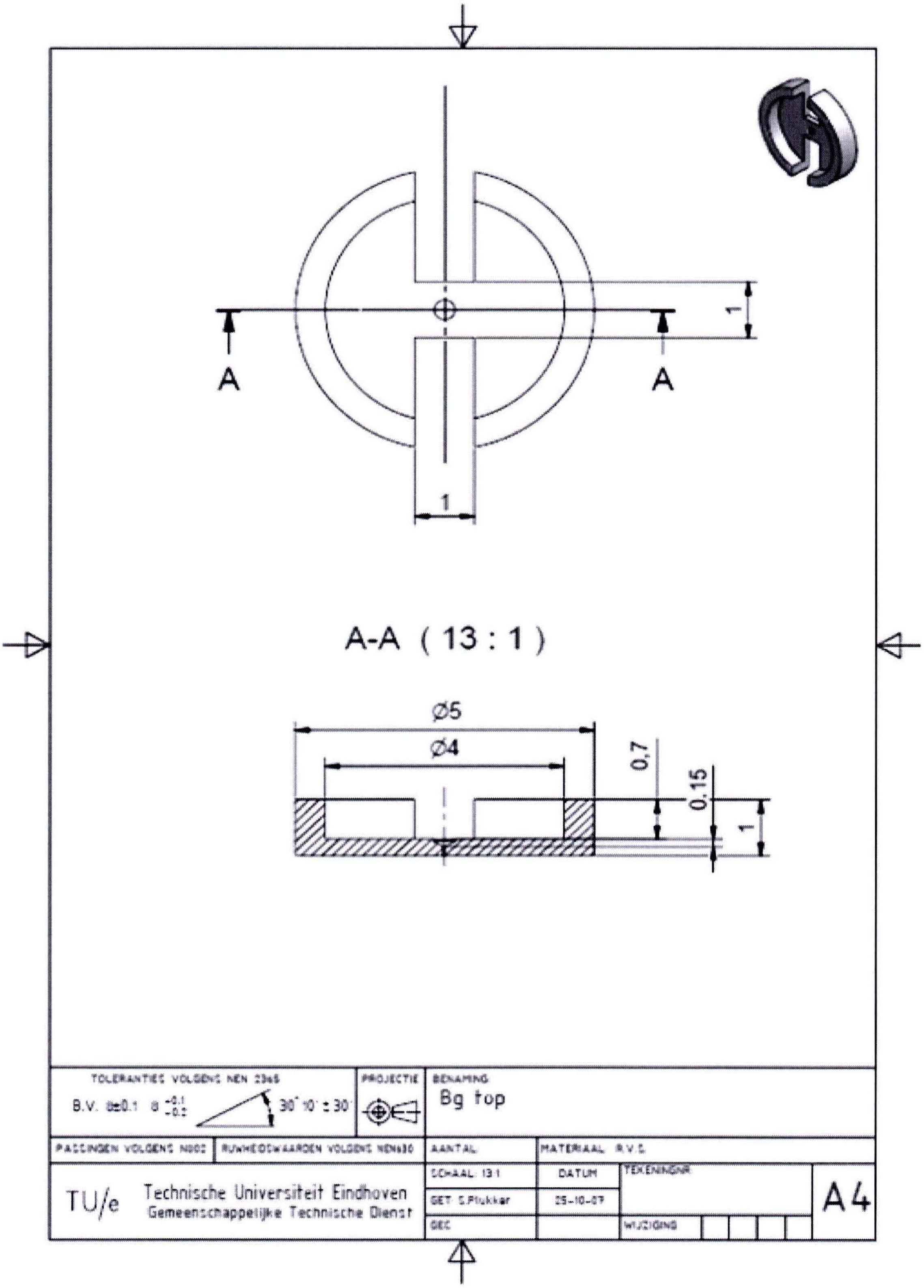

Figure F.5: Technical drawing of the stainless steel bubble generator (thin steel sheet) (*From "Bubble generator design up to May 2009"*, 2009. R. J. van de Broek [75])

Acknowledgement

Hereby I would like to take the opportunity to thank a few people who did tremendous jobs during the last year to help me complete this work. First of all I would like to thank my direct supervisors Paul van Neer and Cees van der Geld who were always there when needed. Without their help, useful discussions and support I was not able to finish this work. I would like to thank Paul Bloemen for his support with the camera setup and all the optical experiments. Besides I would like to thank Coen Baltis who assisted me during the year with a lot of practical issues. Thanks to Axel Lexmond who helped me during the start of the project. A special thanks goes to Henri Vliegen, who helped me with the construction of the experimental setup. At last I would like to thank all my friends, girlfriend and family for their support the last eight years.